Controlled Growth and Application for the Anodization of Tin and Iron

Dissertation

zur Erlangung des Grades
"Doktor der Naturwissenschaften"
im Promotionsfach Chemie

am Fachbereich Chemie,
Pharmazie und Geowissenschaften der
Johannes Gutenberg-Universität Mainz

Nils Mohri
geboren in Heppenheim

Mainz, 2015

Dekan: [redacted]

Erster Gutachter: [redacted]

Zweiter Gutachter: [redacted]

Tag der mündlichen Prüfung: [redacted]

The work for this thesis was carried out at Johannes Gutenberg University of Mainz and the Seoul National University of Korea in the period between July 2012 and June 2015 under the guidance of Prof. [redacted] and Prof [redacted]

Diese Arbeit wurde an der Johannes Gutenberg - Universität Mainz und an der Staatlichen Universität Seoul, Korea in der Zeit vom Juli 2012 und Juni 2015 angefertigt. Die Arbeit wurde von Prof. [redacted] und Prof. [redacted] betreut.

Acknowledgements

First, I would like to thank Prof. Dr. [redacted] for providing me with such an interesting task for my PhD studies and for always providing new ideas and advice during this work. Furthermore, I would like to thank the *International Research and Training Group 1404 - Self-Organized Materials for Optoelectronics* and Prof. Dr. [redacted] for providing the financial support to make the exchange to Seoul possible.

I would also like to express my gratitude to Prof. [redacted] and his group in Seoul National University for hosting me during my stays in Korea and for welcoming me so nicely in your world and always offering a helping hand.

Next I want to thank the members of [redacted], which didn't really have much to do with DSSC's in the end. [redacted] were always helpful and took their time to be open for discussion.

I also want to thank Dr. [redacted] for the many helpful discussions giving me insights into the X-ray microdiffraction. Especially the single-crystal analysis improved my thesis substantially. In the same spot I want to thank [redacted] for the measurement of almost all of my samples on the basis of my, not always easy to understand, sketches.

Especially I want to thank [redacted] of the former "Institut für Angewandte Struktur- und Mikroanalytik" for some of the best experiences of my PhD. I cannot really put into words how much the time in your lab supported me in every aspect. The kind provision of your scanning electron

microscope, which had to endure so many samples and (in the end) files, added with the ("I ordered new nitrogen") energy dispersive X-ray analysis, were essentially the center of my whole work. Without it, this thesis would not have been possible. The use of the X-ray photoelectron spectroscope capped it all off by introducing me into a new world of elemental analysis. But all of those things mentioned above would not have been that special had it not been with [redacted] The coffee-talks often opened a totally new perspective not only on the work ("At first we measure standards and optimize the Nitrogen signal") but also in private life.

A very important thank you goes to the institute workshop for providing me with the best custom-made equipment imaginable. Without their effort, most of the experiments would not have been possible.

Big thanks to [redacted] not only for always providing help and ideas concerning electronic setups ("You could also buy this power source, it goes up to 300 volts and only costs 1800 €!") but also for saving my life when an external ZIP-drive was trying to sabotage my thesis.

A thank you also goes to Korea to [redacted] for an awesome time in Korea. Especially [redacted] I want to mention, not only for being such a good friend but also for the translation of my abstract, even though she had a lot of stress at that time.

Next, I want to thank my "girls" aka coffee group [redacted] and [redacted] for making the time in the office such a good experience, I will always look back to in joy. Also I want to thank my italien coffee-maker [redacted]

not only for making the best coffee in our Institute, tested scientifically by the two of us, but also for being the nicest office neighbor one could wish for.

Furthermore, I want to thank the whole AK Tremel for providing such a diverse working environment while, even though in a large group there are always the sub-groups messing with each other, being supportive and nice which made the years in this group and unforgettable experience.

I also want to thank [redacted], my Chemistry teacher in school, for explaining to me how colors work ("This is not green - it absorbs the complementary color, so it only looks like green.") which got me interested in chemistry in the first place and in the end lead to this thesis.

Last but not least I want to thank my family always standing by me in good and bad times and my wonderful girlfriend for not only making my life better every day but also sometimes giving me the little push needed to do the things I want while also giving me every freedom I need.

Contents

Abstracts

Abstract in English

In modern research, nanochemistry is one of the most studied topics because of the benefit of increased efficiency in almost every application. In this field, the electrochemical anodization has attracted a growing interest in recent years not only due to the broad range of possible applications but also because of the easy control and upscalability of the process. While to this point, many metals have been successfully anodized, the theory behind the pore formation is not yet fully understood. Only with this knowledge, advancements in film quality are possible, widening the range of applications for these tailor made materials. The preparation of self-ordered nanoporous metal oxide films from tin and iron by electrochemical anodization is in the focus of this work.

In **chapter 2**, the synthesis of sponge-like SnO_x by anodization has been investigated. By a combination of tempering and a single or three-step electropolishing method, commercially available tin foil was successfully smoothed. Subsequently, different parameters were varied systematically and the observed structures were characterized using laser microscopy, scanning electron microscopy and X-ray microdiffraction. The application of a buffered solution resulted in the successful synthesis of a homogeneous and defect-free sponge-like SnO_x film.

With the use of the buffered solution, anodization at low-applied voltages became possible, to this point inhibited due to a passivation of the surface by the precipitation of tin oxalate. This resulted in the discovery of a lamellar Sn/SnO_2 core-shell

structure. In **chapter 3**, the growth mechanism of the lamellae is described. The structure was investigated by the use of scanning electron microscopy, X-ray photoelectron spectroscopy, X-ray microdiffraction and Mössbauer spectroscopy.

A comparison of application properties of the SnO_x sponge and the lamellar Sn/SnO_2 structure is presented in **chapter 4**. Efficiencies in photocatalysis, amphiphilic behavior and antimicrobial properties were explored by the degradation of Rhodamine B, contact-angle goniometry and the photooxidation of *E. coli* bacteria respectively.

In **chapter 5**, the SnO_x sponge was applied as a battery material via a carbon coating approach. After electrodeposition on a copper foil and anodization, the film was studied before and after coating via scanning electron microscopy, X-ray microdiffraction, energy dispersive X-ray spectroscopy, X-ray photoelectron spectroscopy and Raman spectroscopy. Furthermore, the film was characterized electrochemically by applying it as an anode in a lithium-ion battery half-cell setup.

The synthesis of nanoporous iron oxide has been investigated in **chapter 6**. By the use of a custom stirring setup, commercially available iron foils were successfully smoothed. Subsequently, the anodization reaction was examined by the systematic variation of different parameters and a new theory for the growth of the nanoporous iron oxide structure is presented.

Abstract in Korean

나노 화학영역은 높은 효율 덕분에 다양한 분야에서 활발히 연구 중이다. 전기화학적 양극산화는 손쉬운 제어와 스케일 업뿐만 아니라 넓은 응용분야를 갖고 있기 때문에, 나노 화학 영역에서 가장 촉망 받는 분야로 그 관심이 커지고 있다. 하지만, 현재까지의 연구로는 박막의 품질 향상과 응용분야에 따른 물질의 기공크기의 변화와 같은 단순한 제어만 가능한 상태이며, 다양한 금속 물질을 이용한 기공형성에 대한 연구는 아직 미흡하다. 따라서, 본 연구에서는 전기화학적 양극산화를 이용한 주석과 철의 자기 정렬 나노 기공 금속박막의 제조를 중점적으로 다루었다.

2 장에서는, 양극산화를 이용한 스폰지 타입의 주석산화물 형성에 대한 연구를 진행하였다. 전기 연마 방법과 온도를 조합하여 상용화된 주석 호일을 성공적으로 연마할 수 있었다. 연이여, 다양한 요소들을 조직적으로 변화시켰으며, 레이저현미경, 주사전자현미경, X-선 미세회절 등의 장비를 이용하여 그 구조를 분석하였다. 완충 용액의 도입을 통하여 균일하고 무결점의 스폰지형의 주석산화막을 성공적으로 합성할 수 있었다.

완충용액의 도입을 통하여 주석 산화물의 침전으로 인한 표면부동화를 방지함으로써 저압에서의 양극산화가 가능했다. 그 결과, 라멜라 Sn/SnO_2 코어셸 구조를 발견할 수 있었다. 3 장에서는 라멜라 구조의 성장 메커니즘을 연구하였다. 각각의 구조는 주사전자현미경과 X 선 광전자 분광법, 뫼스바우어 분광법을 이용하여 분석하였다.

스폰지 구조와 라멜라 구조의 주석 산화물의 특성을 비교한 연구를 4 장에 정리하였다 .광촉매, 양쪽성, 항균성 등의 특성을 비교하기 위해, UV 측정을 통한 Rhodamine B 의 흡광도의 저하를 확인하고 컨택앵글 측정 및 *E. coli* 균의 광산화를 살펴 보았다.

5 장에서는, 스폰지 구조의 주석 산화막에 탄소를 코팅하여 배터리의 양극으로 응용하는 실험을 진행했다. 주석을 구리 호일 위에 전착하고 양극산화를 한 후, 탄소코팅 전후의 조성과 구조를 주사전자현미경, X-선 미세회절, EDX, X 선 광전자 분광법, 라만 분광법을 이용하여 비교 분석 하였다. 추가적으로 박막의 전기화학적 성질을 리튬이온전지의 반쪽셀에 적용하여 분석하였다.

나노 기공 산화철의 합성은 6 장에서 토론하였다. 자가 제작한 교반 시스템을 이용하여 상용화된 철을 연마하였다. 연속적으로 양극산화를 하여 다양한 요소들을 확인하고 새로운 성장이론에 대한 연구를 진행하였다.

Abstract in German

Die Nanochemie ist eines der am intensivsten studierten Gebiete in der Chemie. In diesem Bereich hat die Anodisierung durch ihre einfach zu kontrollierenden Reaktionsbedingungen, die eine genaue Anpassung an die Art des Einsatzes ermöglicht, wobei sie gleichzeitig hochskalierbar bleibt, ein zunehmendes Interesse in der Forschung erfahren. Obwohl bis zum heutigen Tag eine große Anzahl an Metallen erfolgreich anodisiert werden konnte ist die Theorie des Porenwachstums noch nicht vollständig verstanden. Nur mit diesem Wissen ist eine Verbesserung der Filmqualität und somit eine Erweiterung der Einsatzmöglichkeiten erreichbar. In dieser Arbeit wird die Synthese nanoporöser Materialien mittels anodischer Oxidation am Beispiel von Zinn und Eisen untersucht.

In **Kapitel 2** wird die Synthese von schwammänlichem SnO_x untersucht. Durch die Kombination aus Tempern und einer verbesserten einfachen beziehungsweise dreifachen Politur konnten die Folie von oberflächlichen Unreinheiten und Unebenheiten befreit werden. Bei der Anodisierung wurden verschiedene Parameter variiert und mittels Elektronenmikroskopie und Röntgendiffraktion charakterisiert. Durch den Einsatz einer neuartigen Pufferlösung konnten homogene SnO_x Schwämme synthetisiert werden.

Durch den Einsatz der Pufferlösung war es möglich, Anodisierungen mit geringen Spannungen durchzuführen, die bis dahin durch die Abscheidung und folgende Passivierung der Oberfläche durch Zinnoxalat nicht zugänglich waren. Dies führte zur Entdeckung einer neuartigen Sn/SnO_2 Schichtstruktur. In **Kapitel 3** wird der Bildungsmechanismus der Struktur beschrieben. Die Zusammensetzung der

Schichten wurde mittels Elektronenmikroskopie, Röntgendiffraktion, Röntgenphotoelektronenspektroskopie und Mössbauer Spektroskopie untersucht.

Ein Vergleich der Eigenschaften möglicher Anwendungen der SnO_x Schwämme und der Sn/SnO_2 Lamellen ist in **Kapitel 4** beschrieben. Die Effizienz in der Photocatalyse, Amphibischem Verhalten und Antimikrobischem Verhalten wurde mittels Zersetzung von Rhodamin B, Kontaktwinkelmessungen und der Photooxidation von *E. coli* Bakterien untersucht.

In **Kapitel 5** wird die Verwendung des schwammänlichen SnO_x Films als Anodenmaterial mittels Kohlenstoff-Beschichtung untersucht. Nach Elektrodeposition von Zinn auf Kupferfolie und Anodisierung wurde der Film vor und nach der Beschichtung mittels Elektronenmikroskop, Röntgendiffraktometrie, Energiedispersive Röntgenspektroskopie, Röntgenphotoelektronenspektroskopie und Raman Spektroskopie untersucht. Weiterhin wurde der Film elektrochemisch als Anodenmaterial in einer Lithium-Ionen Halbzelle charakterisiert.

Die Untersuchung der Synthese von nanoporösem Eisenoxid wird in **Kapitel 6** beschrieben. Durch die Verwendung einer Rührelektrode konnte die Folie von oberflächlichen Unreinheiten und Unebenheiten befreit werden. Die folgende Anodisierung wurde mittels systematischer Variation verschiedener Parameter untersucht und eine neue Theorie für das Porenwachstum erarbeitet.

1 Introduction

1.1 General Interest

In the face of a growing demand for devices constantly getting smaller in size while increasing in performance, micro- and nanostructured materials are in the focus of research. Nanoparticles for example were shown to boost the performance of batteries and dye-sensitized solar cells by offering a higher surface area. An increase in effective surface area also leads to a significant enhancement of reaction kinetics in catalytic reactions such as the photocatalysis of water. Additionally, nanostructured materials often exhibit altered electronic properties compared to the bulk material due to quantum size effects or surface curvature. This can be exploited particularly in transition metal oxides, which offer a wide range of applications; not only in solar cells and batteries but as well in electrochromic devices and gas sensors. The classical approaches for the synthesis of nanostructured materials are sol-gel method or hydrothermal treatment. Morphologies produced by those techniques are mostly nanopowders, nanowires or nanotubes. Even though nanowires or tubes may offer possible electron pathways for electrically connected devices, their random orientation inhibits a net benefit of the anisotropy.

Self-organization or self-assembly processes are possible methods for the creation of large-scale homogeneous ordered structures allowing for the use of this anisotropy. The most famous example are self-assembled monolayers, which are monomolecular layer forming spontaneously when immersing a substrate into a solution containing amphifunctional molecules.

For transition metals, another technique widely used for over a century for wear and corrosion resistance purposes is the electrochemical anodization.[1] A metal is

connected to an anodic bias while being in contact with a specific electrolyte. By careful choice of the applied bias and nature and concentration of the electrolyte, it is possible not only to oxidize the metal surface but also to etch a regular alignment of pores into the oxide material to form structures of vertically aligned nanopores.[2] Until today, a wide range of metals have been found to be able of forming porous oxide structures via electrochemical anodization, *e.g.* Al,[1][3] Ti,[4] Nb,[5] Ta,[6][7] W,[8] Zr,[9] Ni,[10] Sn[11] and Fe.[12] Despite the wealth of possible applications as gas-sensor,[13] electrode material,[14] solar cells[15][16] and water splitting,[17] very few reports on the anodization of iron and tin exist.

1.2 Theory of electrochemical anodization

Aluminum is the most prominent example of the electrochemical anodization since it was the first one to be anodized successfully to produce a hexagonal array of homogeneous pores.[3] This is the reason why it is the most studied metal and almost all reports concerning the theory of pore formation are based on the experiences with aluminum.[18][19] Despite anodization being used to produce porous structures for a long time, there is still no universal theory on the pore formation and the topic is still discussed controversially in literature.[20] The main reason for this is the used procedure. Since the anodization reaction takes place with the sample immersed in an electrolyte and at applied biases of up to hundred volts,[21][22] in-situ measurements are impossible to achieve, so all the theory is based on snapshots taken after different anodization times. In the following chapter, an overview of the possible reactions will be given, followed by the most prominent theories of pore growth.

1.2.1 Electrochemical oxidation reaction

If a sufficient anodic bias is applied to a metal, which is in contact to an aqueous electrolyte, the metal oxidizes (1). At the cathode, hydrogen evolution occurs (5). Depending on the type of electrolyte and applied bias, three cases are possible:

(I) If the electrolyte is aggressive enough to solvatize all forming metal ions, the surface is continuously dissolved. This reaction is used to electropolish sample surfaces prior to anodization to get rid of defects and impurities on the surface of the sample originated from the manufacturing process.

(II) If a weak electrolyte is used or it is in low concentration, most of the metal ions react with the oxygen provided by the water to form a compact oxide passivation layer (2-3).

(III) Under specific conditions in between the previously mentioned, a competition between oxide formation and dissolution is possible. In this case, a porous oxidic structure is formed.

In the case of the tin anodization, at an applied bias of more than 5 V, oxygen evolution occurs as a side reaction (4) (see Chapter 2.3).

Anode

$$M \rightarrow M^{z+} + ze^- \quad (1)$$

$$M + \frac{z}{2}H_2O \rightarrow MO_{z/2} + zH^+ + ze^- \quad (2)$$

$$M^{z+} + zH_2O \rightarrow M(OH)_z + zH^+ \quad (3.1)$$

$$M(OH)_z \rightarrow MO_{z/2} + \frac{z}{2}H_2O \quad (3.2)$$

$$2H_2O \rightarrow 4H^+ + O_2 + 4e^- \quad (4)$$

Cathode

$$zH_2O + ze^- \rightarrow \frac{z}{2}H_2 + zOH^- \quad (5)$$

1.2.2 Valve metal theory

In the valve metal theory, metals belonging to the group of the so called "valve metals" are claimed to be the prerequisite to form a porous oxide structure.[23] The term "valve metal" originates from their use in the production of vacuum valves.[24] These metals showed an increase in electron emission if covered by a thin layer of oxide. This so-called "valve effect" was later claimed to be the reason for a one-way electrical conductivity during the electrochemical anodization reaction allowing for the anodic current to pass through the oxide while the cathodic current was blocked.[25] Many metals were classified by Güntherschulze *et al.* to exhibit either a complete valve effect as Al, Bi, Sb and Ta or an incomplete valve effect as Ag, Cd, Fe, Mg, Si, Sn, W, Zb and Zr. Other authors divided the valve metals into groups of "most typical members" and "other elements"[26] with aluminum being in the first while titanium and tin being in the second group. Here, iron was not considered to be a valve metal. Si, while incorporated in the category of valve metals, forms porous Si structures instead of SiO_2 when anodized in an aqueous HF solution.[27][28] Nickel on the other hand is not considered a valve metal but forms porous NiO structures if anodized in HF/H_2PO_4 electrolyte.[10] This already shows the valve metal theory to be at best an incomplete description of the anodization. As a conclusion, it can be said that the valve metal theory is mostly a phenomenological attempt to categorize metals by the ability to form porous oxides and lacks any scientific foundation or even an unified categorization.

1.2.3 Electrical field-assisted oxide dissolution

The most common theory used to describe pore formation is the mechanism published by Parkutik and Shershulskii.[18] In this contribution, the anodization reaction is divided into four stages. A schematic illustration of the pore growth and a typical current curve are shown in Figure 1.1.

(I) In the initial stage, the metal surface is passivated as a thick oxide layer is formed. This results in a drop in current as the oxide layer decreases the conductivity of the sample.

(II) Because of local inhomogeneities in the film thickness, local fields occur at the bottom of the pits of the passivation layer. Here dissolution of the oxide is promoted, creating fine-featured pathways into the oxide.

(III) The individual pathways further propagate through the oxide, while slowly transforming into cavities. Due to the localized etching, the net thickness of the passivation layer decreases, resulting in an increase in current. Over time, the pores reach their maximum diameter as they compete with adjacent pores resulting in a self-ordering.

(IV) As the reaction continues, etching of the oxide at the bottom of the pores and oxidation of the metal on the metal-oxide interface reaches equilibrium as the current increase stops and the curve flattens.[29] With further pore growth and thus slowly decrease in mass transport through the holes, the current starts to gradually decrease.

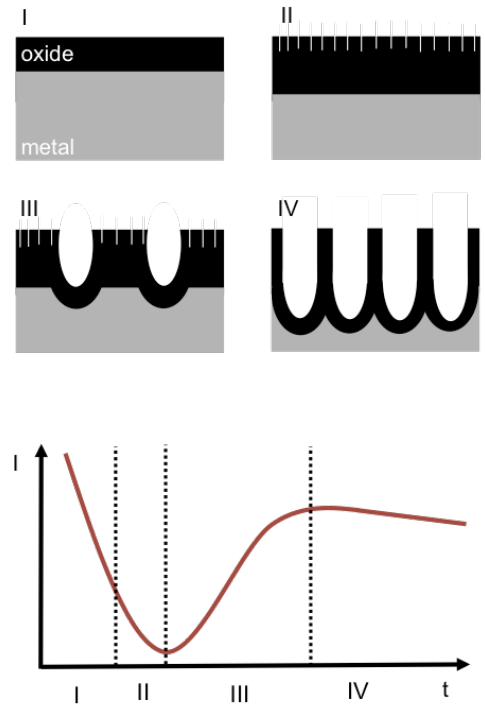

Figure 1.1 Schematic illustration of pore growth (top) and potentiostatic regimes (bottom)

Even though this theory is mostly a phenomenological explanation of the pore growth, it can be applied to the growth of various metal oxides like titanium.[23] The main problem is the fact that the electric field, which is claimed to be the reason for the preferred dissolution of the oxide at the bottom of the pores, is the same causing the formation of the oxide. Attempts in explanations were made by Mott *et al.*,[29] who suggested a high-field pulling of the anions through the oxide at interstitial positions. This was claimed to be possible for hydroxide ions forming in a reaction of oxygen ions with protons at the bottom of the pores, resulting in an effective decrease in size due to the single charge. This theory is supported by the studies from Schmuki *et al.*[30] who examined the formation of titanium oxide nanotubes in a fluoride containing electrolyte. XPS depth profile analysis showed a fluoride-rich layer to

develop at the metal-oxide interface caused by small fluorine ions migrating through the oxide.

1.2.4 Anodic protection

On the basis of the electrical field-assisted oxide dissolution, Wang *et al.* recently published an attempt for an unified theory.[20] The starting point of this theory is the thermodynamic analysis of the anodic formation of the metal oxide and its dissolution reaction. While the oxide formation is an electrochemical reaction, the Gibbs free energy follows the Nernst equation as a function of the electrode potential (6).

$$\Delta G_{ox} = -zFE \qquad (6)$$

Here, z is the electron transfer number, F the Faraday constant and E the electrode potential. The oxide dissolution is a chemical reaction, where the Gibbs free energy (ΔG_{diss}) is a constant, since it does not change with the applied voltage.

Based on this approach, three cases are possible:

(I) If $\Delta G_{ox} > \Delta G_{diss}$, only the oxidation reaction occurs, resulting in a passivated layer on the surface.

(II) If $\Delta G_{ox} < \Delta G_{diss}$, the formed oxide is dissolved completely, no oxide layer is formed.

(III) If the applied voltage is so, that $\Delta G_{ox} \geq \Delta G_{diss}$, hence the dissolution and oxidation are almost in equilibrium, the formation of a porous oxide becomes possible.

In the beginning of the anodization reaction, a passivation layer is formed on the surface of the metal as shown in Figure 1.2. The effective potential is high resulting in

an increase of the Gibbs free energy for the oxidation ($\Delta G_{ox} > \Delta G_{diss}$). Only the oxidation reaction occurs. This is the so-called "anodic protection" of the oxide since the dissolution reaction does not take place. As the passivation layer grows, resistivity increases. This leads to a drop in the effective voltage on the surface of the sample. At one point equilibrium is reached and the effective voltage is so low, that $\Delta G_{ox} = \Delta G_{diss}$. At this point the oxide is protected the least by the anodic bias and is dissolved by the electrolyte. Cavities are formed in the oxide at random spots, resulting in a decrease in resistivity. At these spots, the oxidation reaction increases again and the oxide grows further into the metal, resulting in a bulged metal-oxide interface.

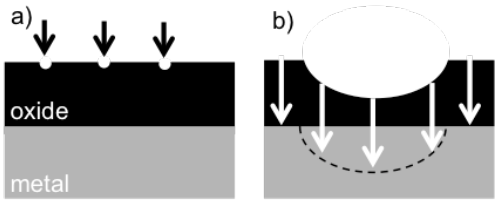

Figure 1.2 Schematic illustration of incident formation of pores

As the reaction continues, pores are formed. A schematic of the conditions for pore growth are shown in Figure 1.3. The anodic bias in the pore walls drops slowly from a1 to a2. This means that over a wide portion of the wall, the effective anodic bias is high enough to protect the oxide from dissolution hence the anodic protection is high. In the center of the pores, the anodic bias drops quickly from b1 to b2 so there is only a thin layer where the oxide is protected. Due to the thin oxide layer on the bottom of the pores, current density there is also higher when compared to the one along the pore walls. Both effects combined result in a preferential oxide formation and dissolution at the bottom of the pores.

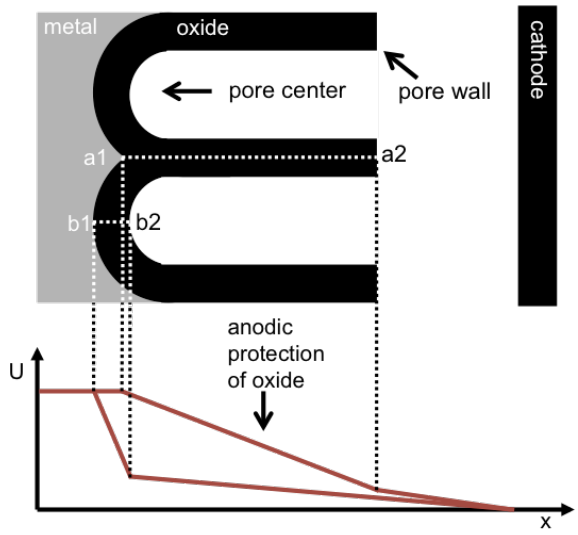

Figure 1.3 Schematic illustration of pore growth (top) and behavior of effective anodic bias in the center and the walls of pores (bottom)

This theory offers a slightly different take on the pore formation. Instead of only arguing the concentration of the electric field, the approach via the Gibbs free energy allows for an explanation of oxide dissolution and formation by the same applied field. The only problem with this approach is the transition from the bulged metal-oxide interface to the pore formation. At the point where the bulged metal is formed, oxide thickness should be homogeneous over the whole sample, which also means the anodic protection is the same. Here, the theory fails to give an explanation, while this stage is covered in the field-assisted oxide dissolution theory.

As a conclusion it can be said that so far, no unified theory has been established to give a complete description of the pore growth. This is the reason, why in this work further studies on the growth mechanism were made.

1.3 Tin dioxide

Tin dioxide is a n-type semiconductor with a band-gap of ~3.6 eV and crystallizes in the tetragonal space group $P4_2/mnm$ with the cell parameters being a = b = 473.8 nm and c = 318.7 nm. In the unit cell, Sn^{4+} is coordinated by six O^{2-}-anions, forming slightly distorted octahedra, whereas the oxygen atoms are coordinated by three tin ions, forming a triangle. Due to its optical transparency and intricate electronic properties, tin dioxide has found use in several applications as electrode material in dye-sensitized solar cells (DSSC),[15][31] light emitting diodes and flat panel displays,[32] as cathode in lithium-ion batteries,[33][34] as a solid state gas-sensor for NO_2[35] and H_2S,[13] in architectural windows[36] allowing for light to pass through while keeping the heat out, and as a self-cleaning antimicrobial glass coatings.[37]

Tin dioxide films are produced by hydrothermal processes,[38] via magnetron sputtering,[39] or atomic deposition.[40] While the anodization of aluminum and titanium had been performed and investigated for a long time, it was not until 2004 that Shin *et al.* first reported the synthesis of self-ordered porous tin oxide via anodization in an aqueous oxalic acid electrolyte.[11] The porous film was found to consist mainly of tin oxide but could easily be transformed to cassiterite by annealing. Compared to the regular pores produced by the anodization of aluminum, anodized tin shows a sponge-like architecture. The reason for this was found to be the production of oxygen gas, which always occurs as a side reaction on the anodization of tin.[41] Since the anodic potential of the oxygen evolution reaction is higher than the one for the formation of tin dioxide, both reactions occur. While formation of nanotubes and -pores is a self-ordering process, every disturbance induced into the system is directly translates into deformations of the structure.

1.4 Iron (III) oxide

Iron (III) oxide is also a n-type semiconductor with a smaller band-gap of 2.2 eV,[42] which crystallizes in the rhombohedral space group *R3c* with the cell parameters being a = b = 503.5 nm and c = 1374.9 nm.[43] The oxide anions are cubic closely packed whereas the Fe^{3+}-ions are found in the octahedral positions. In contrast to the more abundant magnetite (α-Fe_3O_4), hematite (α-Fe_2O_3) has been in the focus of research due to its favorable band-gap energy allowing for the use as an anode for photoelectrochemical water splitting. However, the very short excited state lifetime (~1 ps)[44] and the small hole diffusion length (~2 - 4 nm)[45] severely limit the efficiency in charge separation and collection.

Several methods have been investigated to overcome these limitations by nanostructuring to increase the efficiency of electron hole separation. Zhong *et al.* for example synthesized 3D flower-like nanostructures by a solvothermal ethylene glycol-mediated self-assembly process[46] while Vayssieres *et al.* were able to grow nanorods arrays with a diameter of 7-24 nm by a simple sol-gel method.[47] Via metal organic vapor deposition (MOCVD) Wu *et al.* reported on the synthesis of vertically aligned nanorods on a silicon substrate.[48] Anodization techniques first allowed for the synthesis of nanorods by electrochemical deposition of iron into aluminum oxide (AAO) template and the oxidation to iron oxide after removal of the AAO template.[49][50] Without template, only the formation of hematite nanoparticle thin films was possible.[51][52] It was not until 2006 that Grimes *et al.* first published the direct anodization of iron for the synthesis of nanoporous iron oxide films.[53] Until now, nanotubes of up to 3 µm in length could be synthesized by heating of the electrolyte.[54]

1.5 Aims of the Project

As explained up to this point, the anodization of metals is not yet fully understood. While aluminum and titanium were studied extensively, tin and iron, even though they offer a wide range of possible applications, just came into the focus of research in recent years.

This is the reason why in this work, the anodization of tin and iron shall be studied with the use of X-ray diffraction, scanning electron microscopy and X-ray photoelectron spectroscopy. The main aim is a further understanding and control of the growth mechanism of nanoporous tin and iron oxide, resulting in an increased film quality.

Additionally, applications of the improved anodized tin structure will be investigated.

1.6 References

[1] J. W. Diggle, T. C. Downie and C. W. Goulding, "Anodic oxide films on aluminum," *Chem. Rev.*, vol. 69, no. 3, pp. 365–405, 1969.

[2] F. Keller, M. S. Hunter and D. L. Robinson, "Structural Features of Oxide Coatings on Aluminum," *Journal of The Electrochemical Society*, vol. 100, no. 9, p. 411, 1953.

[3] H. Masuda and K. Fukuda, "Ordered metal nanohole arrays made by a two-step replication of honeycomb structures of anodic alumina.," *Science*, vol. 268, no. 5216, pp. 1466–1468, 1995.

[4] J. M. Macák, H. Tsuchiya and P. Schmuki, "High-aspect-ratio TiO2 nanotubes by anodization of titanium," *Angew. Chemie - Int. Ed.*, vol. 44, pp. 2100–2102, 2005.

[5] J. Choi, J. H. Lim, S. C. Lee, J. H. Chang, K. J. Kim and M. A. Cho, "Porous niobium oxide films prepared by anodization in HF/H3PO4," *Electrochim. Acta*, vol. 51, no. 25, pp. 5502–5507, 2006.

[6] I. Sieber, B. Kannan and P. Schmuki, "Self-Assembled Porous Tantalum Oxide Prepared in H2SO4/HF Electrolytes," *Electrochemical and Solid-State Letters*, vol. 8, no. 3, p. J10, 2005.

[7] J. E. Barton, C. L. Stender, P. Li and T. W. Odom, "Structural control of anodized tantalum oxide nanotubes," *J. Mater. Chem.*, vol. 19, p. 4896, 2009.

[8] N. Mukherjee, M. Paulose, O. K. Varghese, G. K. Mor and C. A. Grimes, "Fabrication of nanoporous tungsten oxide by galvanostatic anodization," *Journal of Materials Research*, vol. 18, no. 10, pp. 2296–2299, 2003.

[9] H. Tsuchiya, J. M. MacAk, L. Taveira and P. Schmuki, "Fabrication and characterization of smooth high aspect ratio zirconia nanotubes," *Chem. Phys. Lett.*, vol. 410, no. 4–6, pp. 188–191, 2005.

[10] N. K. Shrestha, M. Yang and P. Schmuki, "Self-Ordered Nanoporous Nickel Oxide/Fluoride Composite Film with Strong Electrochromic Contrast," *Electrochemical and Solid-State Letters*, vol. 13, no. 8, p. C21, 2010.

[11] H.-C. Shin, J. Dong and M. Liu, "Porous Tin Oxides Prepared Using an Anodic Oxidation Process," *Adv. Mater.*, vol. 16, no. 3, pp. 237–240, 2004.

[12] B. J. Park, H. E. Prakasam and C. A. Grimes, "Fabrication of Iron (III) Oxide Nanostructures By Potentiostatic Anodization," *EEREU Annu. Res. J. Electr. Eng. Res. Exp. Undergraduates*, vol. III, p. 117, 2005.

[13] C. Jin, T. Yamazaki, K. Ito, T. Kikuta and N. Nakatani, "H2S sensing property of porous SnO2 sputtered films coated with various doping films," *Vacuum*, vol. 80, no. 7 SPEC. ISS., pp. 723–725, 2006.

[14] Y. Idota, "Tin-Based Amorphous Oxide: A High-Capacity Lithium-Ion-Storage Material," *Science*, vol. 276, no. 5317, pp. 1395–1397, 1997.

[15] A. Birkel, Y.-G. Lee, D. Koll, X. Van Meerbeek, S. Frank, M. J. Choi, Y. S. Kang, K. Char and W. Tremel, "Highly efficient and stable dye-sensitized solar cells based on SnO2 nanocrystals prepared by microwave-assisted synthesis," *Energy & Environmental Science*, vol. 5, no. 1, p. 5392, 2012.

[16] K. Xie, Z. Lu, H. Huang, W. Lu, Y. Lai, J. Li, L. Zhou and Y. Liu, "Iron supported C@Fe3O4 nanotube array: a new type of 3D anode with low-cost for high performance lithium-ion batteries," *J. Mater. Chem.*, vol. 22, p. 5560, 2012.

[17] S. K. Mohapatra, S. E. John, S. Banerjee and M. Misra, "Water photooxidation by smooth and ultrathin R-Fe2O3 nanotube arrays," *Chem. Mater.*, vol. 21, no. 9, pp. 3048–3055, 2009.

[18] V. P. Parkhutik and V. I. Shershulsky, "Theoretical modelling of porous oxide growth on aluminium," *J. Phys. D. Appl. Phys.*, vol. 25, pp. 1258–1263, 1992.

[19] F. Li, L. Zhang and R. Metzger, "On the growth of highly ordered pores in anodized aluminum oxide," *Chem. Mater.*, vol. 10, no. 28, pp. 2470–2480, 1998.

[20] M. Wang, Y. Liu and H. Yang, "A unified thermodynamic theory for the formation of anodized metal oxide structures," *Electrochim. Acta*, vol. 62, pp. 424–432, 2012.

[21] W. Lee, R. Ji, U. Gösele and K. Nielsch, "Fast fabrication of long-range ordered porous alumina membranes by hard anodization.," *Nat. Mater.*, vol. 5, no. 9, pp. 741–747, 2006.

[22] K. Schwirn, W. Lee, R. Hillebrand, M. Steinhart, K. Nielsch and U. Gösele, "Self-ordered anodic aluminum oxide formed by H2SO4 hard anodization," *ACS Nano*, vol. 2, no. 2, pp. 302–310, 2008.

[23] J. M. Macak, H. Tsuchiya, A. Ghicov, K. Yasuda, R. Hahn, S. Bauer and P. Schmuki, "TiO2 nanotubes: Self-organized electrochemical formation, properties and applications," *Curr. Opin. Solid State Mater. Sci.*, vol. 11, no. 1–2, pp. 3–18, 2007.

[24] J.F. Rider, *Inside the Vacuum Tube*. New York: John F. Rider Publisher, INC, 1945.

[25] A. Güntherschulze and H. Betz, *Elektrolytkondensatoren*. Berlin: M. Krayn Verlag, 1937.

[26] L. Young, *Anodic Oxide Films*. London: Academic Press, 1961.

[27] V. Lehmann and U. Gösele, "Porous silicon formation: A quantum wire effect," *Appl. Phys. Lett.*, vol. 58, no. 8, pp. 856–858, 1991.

[28] R. L. Smith and S. D. Collins, "Porous silicon formation mechanisms," *J. Appl. Phys.*, vol. 71, no. 8, 1992.

[29] T. P. Hoar and N. F. Mott, "A mechanism for the formation of porous anodic oxide films on aluminium," *J. Phys. Chem. Solids*, vol. 9, no. 2, pp. 97–99, 1959.

[30] P. Roy, S. Berger and P. Schmuki, "TiO2 nanotubes: Synthesis and applications," *Angew. Chemie - Int. Ed.*, vol. 50, no. 13, pp. 2904–2939, 2011.

[31] F. Yang and S. R. Forrest, "Organic Solar Cells Using Transparent SnO2-F Anodes," *Adv. Mater.*, vol. 18, no. 15, pp. 2018–2022, 2006.

[32] J. F. Wager, "Applied physics. Transparent electronics.," *Science*, vol. 300, no. 5623, pp. 1245–1246, 2003.

[33] J. S. Chen and X. W. Lou, "SnO2-based nanomaterials: Synthesis and application in lithium-ion batteries," *Small*, vol. 9, no. 11, pp. 1877–1893, 2013.

[34] Y. Yu, C. H. Chen and Y. Shi, "A tin-based amorphous oxide composite with a porous, spherical, multideck-cage morphology as a highly reversible anode material for lithium-ion batteries," *Adv. Mater.*, vol. 19, pp. 993–997, 2007.

[35] J. Kaur, S. C. Roy and M. C. Bhatnagar, "Highly sensitive SnO2 thin film NO2 gas sensor operating at low temperature," *Sensors Actuators, B Chem.*, vol. 123, no. 2, pp. 1090–1095, 2007.

[36] C. G. Granqvist and A. Hultåker, "Transparent and conducting ITO films: New developments and applications," in *Thin Solid Films*, vol. 411, no. 1, pp. 1–5, 2002.

[37] R. André, F. Natalio, M. N. Tahir, R. Berger and W. Tremel, "Self-cleaning antimicrobial surfaces by bio-enabled growth of SnO2 coatings on glass.," *Nanoscale*, vol. 5, no. 8, pp. 3447–56, 2013.

[38] J. Liu, Y. Li, X. Huang, R. Ding, Y. Hu, J. Jiang and L. Liao, "Direct growth of SnO2 nanorod array electrodes for lithium-ion batteries," *J. Mater. Chem.*, vol. 19, p. 1859, 2009.

[39] R. Kohler, H. Besser, M. Hagen, J. Ye, C. Ziebert, S. Ulrich, J. Proell and W. Pfleging, "Laser micro-structuring of magnetron-sputtered SnOx thin films as anode material for lithium ion batteries," *Microsyst. Technol.*, vol. 17, no. 2, pp. 225–232, 2011.

[40] X. Meng, Y. Zhang, S. Sun, R. Li and X. Sun, "Three growth modes and mechanisms for highly structure-tunable SnO2 nanotube arrays of template-directed atomic layer deposition," *J. Mater. Chem.*, vol. 21, p. 12321, 2011.

[41] M. Wang, H. Yang and Y. Liu, "Current oscillations during potentiostatic anodization of tin in alkaline electrolytes," *Electrochim. Acta*, vol. 56, no. 20, pp. 7051–7057, 2011.

[42] Y. Matsumoto, "Energy Positions of Oxide Semiconductors and Photocatalysis with Iron Complex Oxides," *J. Solid State Chem.*, vol. 126, no. 2, pp. 227–234, 1996.

[43] J. D. Bernal, "The Oxides and Hydroxides of Iron and Their Structural Inter-Relationships," *Clay Minerals*, vol. 4, no. 21. pp. 15–30, 1959.

[44] A. G. Joly, J. R. Williams, S. A. Chambers, G. Xiong, W. P. Hess and D. M. Laman, "Carrier dynamics in α-Fe2O3 (0001) thin films and single crystals probed by femtosecond transient absorption and reflectivity," *J. Appl. Phys.*, vol. 99, no. 5, 2006.

[45] J. H. Kennedy, "Photooxidation of Water at α-Fe2O3 Electrodes," *Journal of The Electrochemical Society*, vol. 125, no. 5, p. 709, 1978.

[46] L. S. Zhong, J. S. Hu, H. P. Liang, A. M. Cao, W. G. Song and L. J. Wan, "Self-assembled 3D flowerlike iron oxide nanostructures and their application in water treatment," *Adv. Mater.*, vol. 18, no. 18, pp. 2426–2431, 2006.

[47] L. Vayssieres, N. Beermann, S. E. Lindquist and A. Hagfeldt, "Controlled aqueous chemical growth of oriented three-dimensional crystalline nanorod arrays: Application to iron(III) oxides," *Chem. Mater.*, vol. 13, no. 2, pp. 233–235, 2001.

[48] J.-J. Wu, Y.-L. Lee, H.-H. Chiang and D. K.-P. Wong, "Growth and magnetic properties of oriented alpha-Fe2O3 nanorods.," *J. Phys. Chem. B*, vol. 110, no. 37, pp. 18108–18111, 2006.

[49] A. Mao, N.-G. Park, G. Y. Han and J. H. Park, "Controlled growth of vertically oriented hematite/Pt composite nanorod arrays: use for photoelectrochemical water splitting.," *Nanotechnology*, vol. 22, no. 17, p. 175703, 2011.

[50] A. Kleiman-Shwarsctein, M. N. Huda, A. Walsh, Y. Yan, G. D. Stuckyst, Y. S. Hu, M. M. Al-Jassim and E. W. McMland, "Electrodeposited aluminum-doped α-Fe2O3 photoelectrodes: Experiment and theory," *Chem. Mater.*, vol. 22, no. 2, pp. 510–517, 2010.

[51] R. L. Spray and K. S. Choi, "Photoactivity of transparent nanocrystalline Fe2O3 electrodes prepared via anodic electrodeposition," *Chem. Mater.*, vol. 21, no. 15, pp. 3701–3709, 2009.

[52] Y. S. Hu, A. Kleiman-Shwarsctein, A. J. Forman, D. Hazen, J. N. Park and E. W. McFarland, "Pt-doped alpha-Fe2O3 thin films active for photoelectrochemical water splitting," *Chem. Mater.*, vol. 20, no. 12, pp. 3803–3805, 2008.

[53] H. E. Prakasam, O. K. Varghese, M. Paulose, G. K. Mor and C. A. Grimes, "Synthesis and photoelectrochemical properties of nanoporous iron (III) oxide by potentiostatic anodization," *Nanotechnology*, vol. 17, pp. 4285–4291, 2006.

[54] R. R. Rangaraju, a Panday, K. S. Raja and M. Misra, "Nanostructured anodic iron oxide film as photoanode for water oxidation," *J. Phys. D. Appl. Phys.*, vol. 42, p. 135303, 2009.

2 Controlled Anodization for the Synthesis of Smooth Nanoporous Tin Oxide Films

2.1 Introduction

As described in chapter 1, tin dioxide as a well-known n-type semiconductor offering a wide variety of possible applications such as a catalyst,[1][2] in gas sensing,[3]–[5] solar cells,[6][7] UV detectors[8][9] and as electrochemical energy storage[10][11]. Anodic tin oxide reported until today exhibits a variety of structural disadvantages in the art of cracks, rough surface and cavities along former grain boundaries of the bulk metal. In this chapter, improvements of the homogeneity and surface structure of the tin oxide sponge were investigated. By tempering of the foils, defects originating from grain boundaries could be eliminated. Application of a buffered electrolyte allowed the synthesis of homogeneous sponge-like tin oxide films. Investigation of the backside of the film showed closed pores while on the bulk material no imprints were found. Cross section measurements revealed a homogeneous film thickness over almost the whole diameter while high-resolution images showed the film to consist of oriented pores aligned in a lamellar manner.

2.2 Experimental

2.2.1 Materials

All starting materials were used without further purification. Commercially available tin foil with a thickness of 0.25 mm and a purity of 99.998 % was purchased from ABCR. The foil was cut into round plates with a diameter of 15 mm with a hole punch. Polishing solution consisted of n-butanol (99%, Acros Organics), methanol (p.A., Sigma-Aldrich), perchloric acid (Sigma-Aldrich) and MilliQ-water (18.3 ΩM/cm).[12] As part of the electrolyte, oxalic acid (p.A., Merck), di-potassium oxalate (≥ 99 %, Acros) and ethylene glycole (99 %, ChemPur) were used.

2.2.2 Tempering

Prior to electropolishing and anodization, the foil was tempered in a muffle furnace (Nabertherm S27) with a heating rate of 5 °C/min and a dwell time of either 80 h at 155 °C or 1h at 400 °C. After heating time was over, the oven was turned off and allowed to cool down to room temperature.

2.2.3 Experimental Setup

Anodic bias for all reactions was applied via a Voltcraft PSP 1803 voltage source. For the reactions, a custom made setup was used (Figure 2.1). It consists of a copper block, a PTFE-cylinder and a metal ring. The copper block with a diameter of 10 cm, equipped with six screws fixed in a circular way, was later connected to the external circuit linking the current to the sample. The PTFE-cylinder, used to hold the electrolyte, had a round cutout of 10 mm in diameter at the bottom, which was fitted with a rubber joint to guarantee a tight fit between cylinder and sample. The foil was placed in the center of the copper block and covered by the PTFE-cylinder. Then the two parts were fixed using six nuts to prevent leaking of the electrolyte. For stirring, a

commercially available drilling machine (CMI) was equipped with a custom made rotating steel electrode used as a cathode.

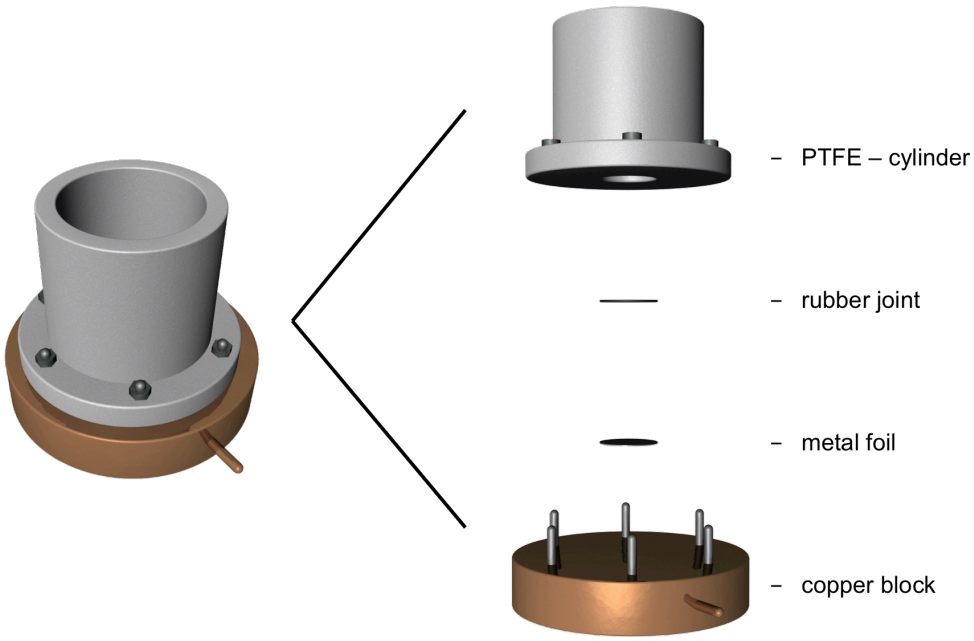

Figure 2.1 Illustration of PTFE-setup. Left: Assembled setup Right: Overview of the individual parts of the setup.

2.2.4 Sample Preparation

Electropolishing was performed with a standard polishing solution, used for titanium and aluminium,[13][14] modifying a method described by Alexander Birkel.[15] The solution consists of 900 ml methanol, 600 ml n-butanol, 85.7 ml 70% perchloric acid and 14.3 ml MilliQ-water. For electropolishing, 30 ml of cooled (T = -28 °C) solution were filled into the PTFE-cylinder and a constant anodic bias of 40 V was applied via an rotating steel electrode positioned at the bottom of the cylinder cutout, close to the sample surface. Non-tempered samples were polished for 20 seconds at maximum rotation velocity of the drilling machine. Tempered samples were polished for 20 seconds without stirring, 12 seconds at maximum velocity and again 7 seconds without rotation. Anodic oxidation was performed in the same setup using a graphite electrode (diameter: 0.5 cm) positioned in the center of the cylinder with a constant distance of about 1 cm to the sample surface. As electrolyte, different compositions of oxalic acid and di-potassium oxalate dissolved in different concentrations of water and ethylene glycol were investigated. Anodic bias for electropolishing and anodization was applied by a Voltcraft PSP 1803 voltage source. After anodization, the electrolyte was removed, the sample rinsed with deionized water and air-dried.

2.2.5 Characterization

Scanning electron microscopy (SEM)

Surface topography was analyzed using a high-vacuum mode scanning electron microscope (SEM; FEI Quanta 200 FEG Environmental-SEM, FEI Deutschland GmbH, Frankfurt / Main, Germany) at an acceleration voltage of 15 kV.

Cross section measurement

Samples were embedded in Poly(methyl methacrylate) (PMMA) using DuroFix-2 Kit by Struers GmbH. PMMA cylinder were then cut into disks of approx. 1 mm thickness with an EXAKT 300CP diamond band saw. Disks were glued on Plexiglas slides and polished by Struers RotoPol-31 for 30 seconds with polishing paper of a grain size of 1200 and 2 minutes with a grain size of 4000. Polished samples were then applied to an aluminum stub and measured in SEM using low vacuum mode.

Laser Microscopy

Laser microscopy images were recorded using a confocal Keyence VK-8710 laser microscope. As guiding value for surface roughness, the Rq-value was used. It is calculated as followed:

$$R_q = \sqrt{(\frac{1}{N} * \sum (z(x) - < z >)^2)}$$

The variable z is the difference between the heights of the sample to an imaginary plane through the mean height of the sample.

X-ray photoelectron spectroscopy (XPS)

XPS spectra were measured on a PHI 5600 Multi-Technique XPS (Physical Electronics, Lake Drive East, Chanhassen, MN) using monochromatized Al Kα at 1486.6 eV. Atomic concentrations were calculated using MULTIPAK 9.4.1.2 software. Peak fitting was performed with CASA XPS Version 2.3.14 software.

X-ray diffraction (XRD)

The crystal structure of tin was examined via room temperature X-ray diffraction on a Bruker D8 Discover instrument operated in reflection geometry with a CuK$\alpha_{1,2}$ X-ray source.

2.3 Results and Discussion

2.3.1 Tempering

Any irregularities on the foil are subsequently transferred as defects to the anodized film. Therefore, the first measure to optimize film quality should be the minimization of these irregularities. Until now, tempering was only used as a measure to increase crystallinity of the anodized sponge.[16]

Low-temperature Tempering

With a melting point of 231.93 °C, tempering of the pure metal was examined at a temperature of 155 °C for 80 h. Optical comparison of tempered samples to untreated foils showed a darker color of the surface and domains of varying color at different locations of the sample (Figure 2.2). Darkening of the surface is due to a passivation layer of tin(II) oxide, as proven by XRD analysis (Figure 2.3). Low-voltage anodization visualized the increased grain size, as large domains with high degree of orientation alignment could be synthesized as proven by SEM and XRD analysis (see Chapter 3.3.2).

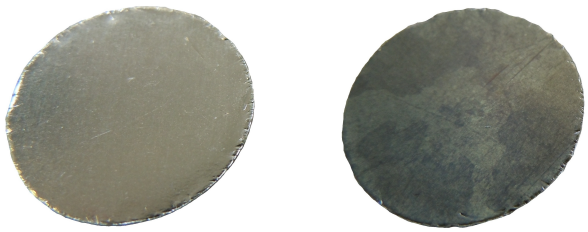

(I) (II)

Figure 2.2 Digital images of untreated and tempered foil. Left: Silver-colored, non-tempered tin foil. Right: Darkened tempered tin foil with domain-like color differences on the surface.

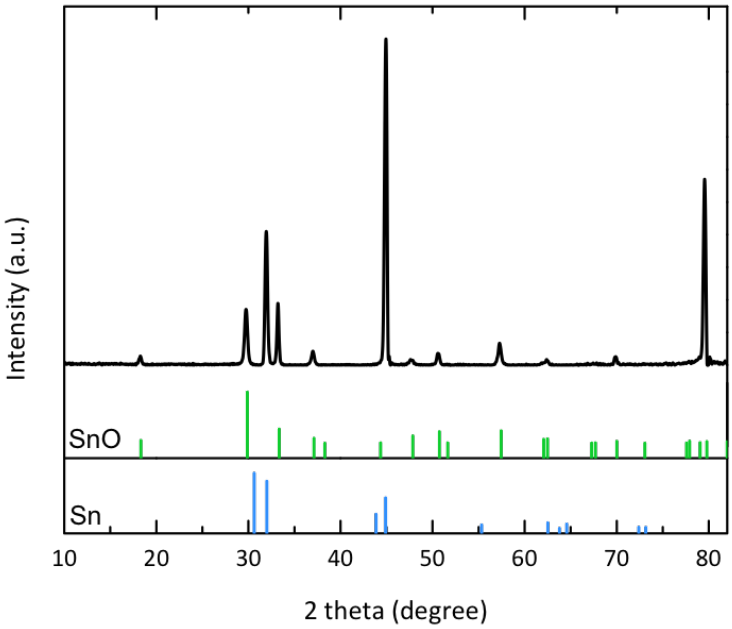

Figure 2.3 X-ray diffraction pattern of tempered foil. Reflexes of β- Sn and Romarchite are marked in the diffractogram

High-temperature Tempering

Following the promising results of the low-temperature tempering, an increase in temperature was examined. The foil was tempered with a heating rate of 5 °C/min and a dwell time of 1h at 400 °C. On the one hand, heat treatment resulted in a thick passivation layer of tin dioxide demanding an adjustment of the electropolishing procedure (see Chapter 2.3.2). On the other hand, heating the foil over the melting point and slowly cooling down the samples to room temperature lead to a recrystallization of the structure. The result was a high degree of orientation alignment over the whole sample, which was proven by XRD analysis of a high-temperature tempered and subsequently polished foil (see Chapter 3.3.2). Tempering decreased surface roughness of anodized samples significantly (see Chapter 2.4.2), producing more homogeneous samples.

2.3.2 Electropolishing

The as-purchased tin foil, even though they are of high purity, exhibit a noticeable and, depending on the supplier or batch, varying degree of roughness, caused by rolling of the foil. Laser microscopy images show deep trenches resulting in height differences of up to 4 micrometer and an Rq-value of 0.20 µm (see Figure 2.4). Furthermore, as tin oxidizes rather easy, a thin passivation layer of tin oxide is covering the surface.

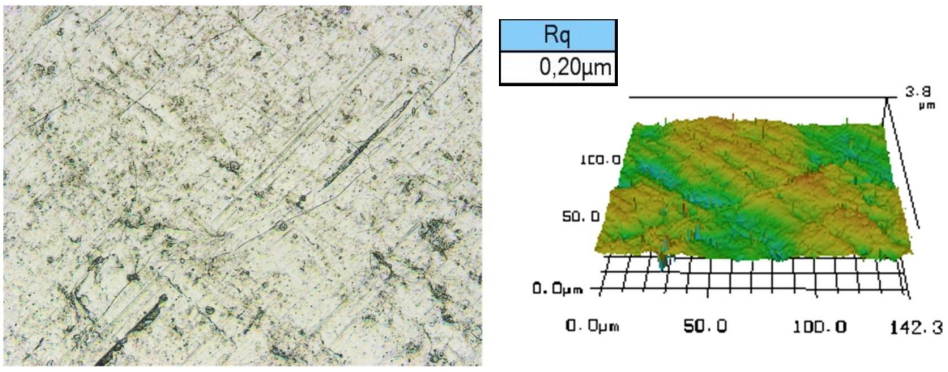

Figure 2.4 As purchased tin foil Left: Light microscopy image of unpolished surface with trenches and defects from rolling of the foil. Right: 3D topographic image extended 10-fold in z-axis and calculated Rq-value.

If an uneven surface is anodized, the resulting oxide film shows the same structure *i.e.* a rough surface (compare Chapter 5.3.1). To inhibit this prestructuring, the foil was electropolished prior to anodization, using the same PTFE-Setup. As polishing solution, a standard mixture consisting of perchloric acid, methanol, n-butanol and water was used which had produced good results in the electropolishing of titanium.[12] As for titanium, the solution was cooled to approximately -28 °C and an anodic bias of 40 V was applied. Cooling of the solution slows down the reaction rate at the beginning where the current flow is the highest.

Multi-step polishing

Starting point for the electropolishing procedure was a scheme tested and established by Alexander Birkel.[15] The scheme was based on repeatedly oxidizing and cleaning of the foils' surface. Polishing solution was filled into the beaker and an anodic bias was applied for several seconds. Then the polishing solution was removed. The sample, still within the setup, was cleaned with MilliQ water and dried with tissue paper. Afterwards, the solution was filled back into the beaker and the next step of electropolishing began. Those steps were repeated 5 to 7 times until an (subjective) evenly polished surface was reached. A digital image of the foil before and after electropolishing is shown in Figure 2.5. It is clearly visible that the polished foil exhibits a smoother surface, as the reflectivity is higher. Light microscopy confirms the decreased roughness as Rq-value decreases to 0.04 µm (Figure 2.6).

Figure 2.5 Left: Untreated tin foil. Right: Tin foil after multi-step electropolishing.

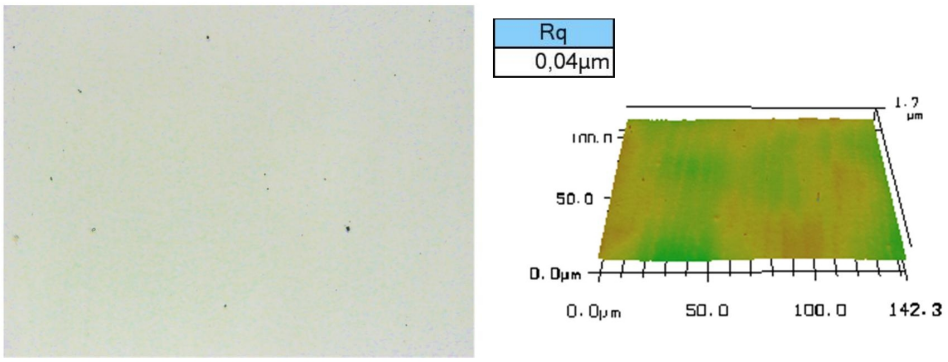

Figure 2.6 Multi-step polished tin foil after five repetitions. Left: Light microscopy image of polished surface with minimal defects (black spots). Right: 3D topographic image extended 10-fold in z-axis and calculated Rq-value

Admittedly, the procedure leads to polished sample surfaces, but repetition of the polishing steps for several times was time-consuming and not easy to reproduce since every electropolishing step had to be stopped, when the sample showed an even brown film of tin(II) oxide over the whole visible surface. Since the samples do not react homogeneously over the whole surface, the occurrence of the brown film starts at the highest and/or roughest point of the sample as it has the highest surface area. From there, the size of the brown spot increases until the whole sample is covered. Reaching this point took from 20 to 25 seconds in the first, down to 7-8 seconds in the last repetition. If the optimal time for one of the electropolishing steps was missed, the roughness of the sample increased and the sample had to be discarded (representative image in Figure 2.7).

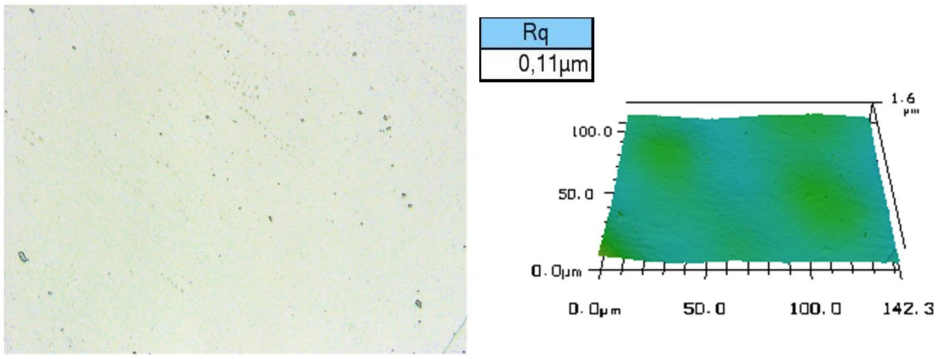

Figure 2.7 Multi-step polished tin foil after eight repetitions. Left: Light microscopy image of polished foil with increased defect concentration (black spots). Right: 3D topographic image extended 10-fold in z-axis and calculated Rq-value

Stirred polishing

Because of the disadvantages concerning reproducibility and length of the multi-step procedure mentioned above, a new polishing procedure had to be found. The reason for the multi-step procedure was the generation of a passivation layer of tin oxide on the surface, loosely attached to the bulk material. It became visible after stopping the reaction as the in-situ formed tin(II) oxide was oxidized to the stable tin(IV) oxide indicated by a change in color of the film formed on the surface from dark brown to white. Removing the polishing solution and cleaning the sample with water removed the oxide. To get rid of the necessity of removing the polishing solution, a custom made rotating steel electrode was manufactured (Figure 2.8).

Figure 2.8 Digital image of custom-made electrode. Left: side view showing diagonal cut at the bottom. Right: front view with cutouts to improve stirring.

The bottom of the electrode was cut diagonally which allowed stirring of the solution in close proximity to the sample surface. The stirring-effect was supported by two

cutouts in the electrode, increasing the turbulences produced by rotation of the cathode. Both effects combined successfully removed tin(II) oxide away from the surface directly after formation, so the cleaning step in between two polishing repetitions could be omitted. Optimization yielded into a single-step polishing for 20 seconds at maximum rotation velocity for non-tempered samples. Digital images already show the surface to be smoother than after a multi-step polishing procedure (Figure 2.9). Laser microscopy confirms the improvements in polishing as the Rq-value decreases further down to 0.02 µm (Figure 2.10).

Figure 2.9 Left: Tin foil after multi-step polishing. Right: Tin foil after stirred polishing

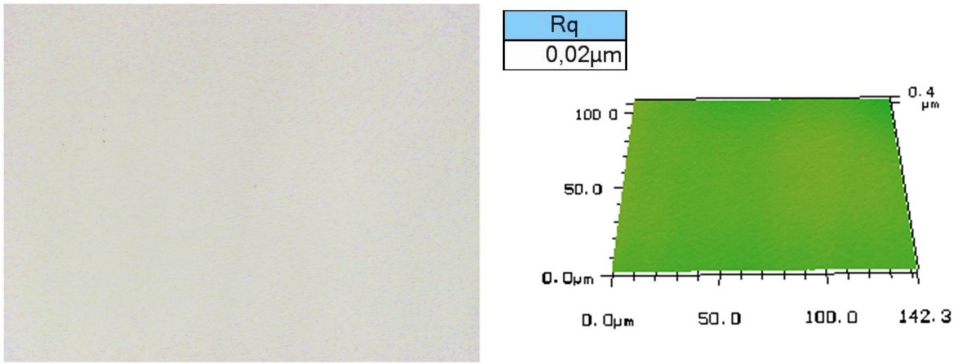

Figure 2.10 Stirred polished non-tempered tin foil. Left: Light microscopy image of polished foil. Right: 3D topographic image extended 10-fold in z-axis and calculated Rq-value

Due to a thicker passivation layer on the surface of a tempered sample, a three-step procedure (without removal of the polishing solution) was necessary. In the first step, the sample is electropolished without stirring, for a homogeneous removal of the thick passivation layer. Then the sample is polished for 15 seconds with maximum rotation velocity and finally for 7 seconds without rotation. The procedure created smooth sample surfaces as indicated by a reflectivity equal to a non-tempered foil (Figure 2.11). Laser microscopy confirms a low surface roughness as the Rq-value is in the same order of magnitude as a polished non-tempered foil (Figure 2.12).

Figure 2.11 Left: Polished non-tempered foil. Right: Polished tempered foil

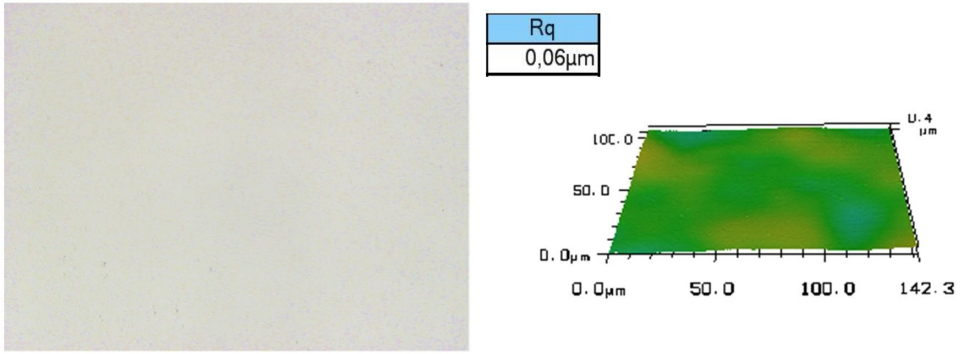

Figure 2.12 Stirred polished tempered tin foil. Left: Light microcopy image of polished foil. Right: 3D topographic image extended 10-fold in z-axis and calculated Rq-value

Analysis of the polished foil in SEM shows no contrast, *i.e.* the sample exhibits no visible height difference (Figure 2.13). Cross section analysis of the polished foil embedded in PMMA also showed no height differences on the sample confirming a successful polish (Figure 2.14). X-ray microdiffraction was used to investigate the chemical composition of a polished sample (Figure 2.15). Reflections exclusively attributed to beta tin are visible, indicating a successful removal of surface oxide.

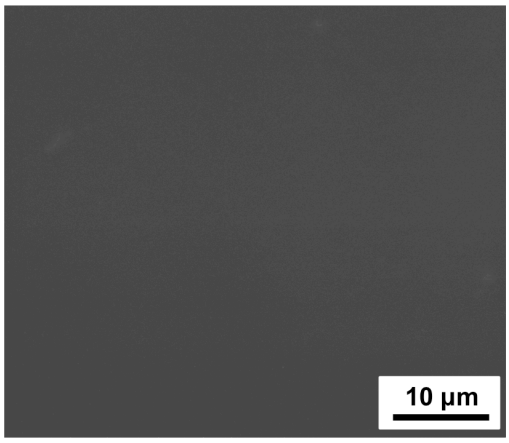

Figure 2.13 SEM image of tin foil after stirred electropolishing.

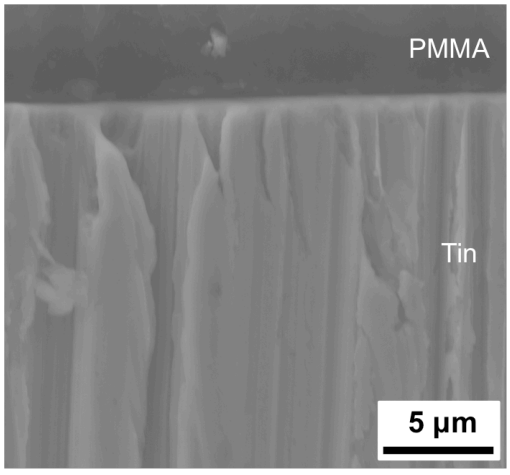

Figure 2.14 Cross section SEM image of a polished tin foil embedded in PMMA.

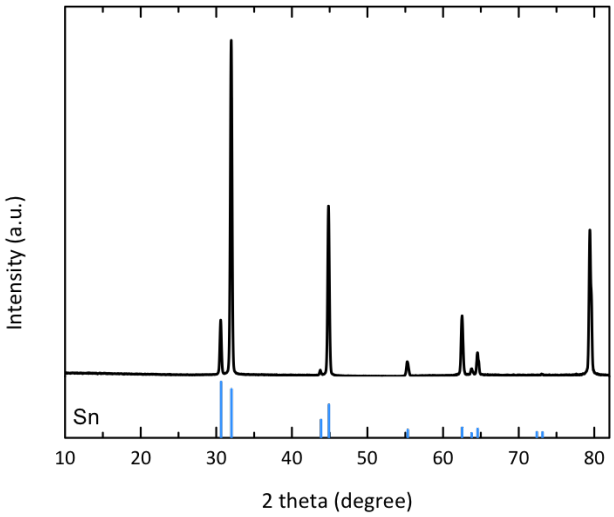

Figure 2.15 X-ray diffraction pattern of tempered tin foil after electropolishing. Reference reflections for tin (blue)

2.4 Anodization

2.4.1 Aqueous Oxalic Acid Electrolyte

Since the first publication by Shin *et al.*,[17] oxalic acid has proven to be the quasi standard for the anodization of tin. For a better understanding of the reaction, different anodization times and applied voltages were investigated (Table 2.1)

Table 2.1 Anodizations performed with oxalic acid electrolyte

c(Oxalic acid) / mol/l	Voltage / V	Time / min
0.5	10	10
0.5	10	60
0.5	30	10
0.5	2	10

Using an aqueous solution of 0.5 M oxalic acid at an applied anodic bias of 10 V leads to the formation of a rough, sponge-like film of tin dioxide (Figure 2.16).

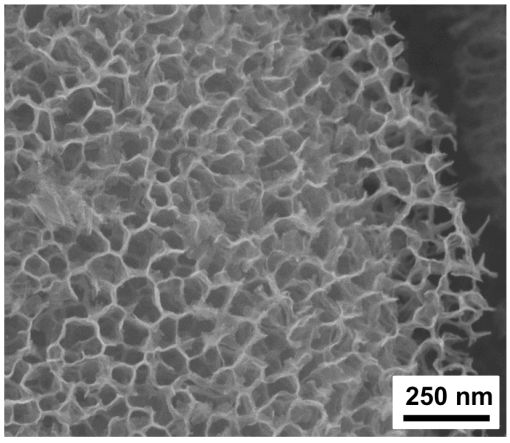

Figure 2.16 SEM image of anodized tin foil in oxalic acid at 10 V for 10 min.

Walls of the structure are frayed and thin. Former grain boundaries become visible as deep trenches in the nanoporous film (Figure 2.16 right). At longer anodization time, spallation of the oxide film due to stress generated by oxygen evolution and precipitation of colorless crystals on the surface of the sample occur (Figure 2.17 arrow). X-ray powder diffraction showed the crystals to consist of tin oxalate (Figure 2.18). Reflections from SnO can be attributed to the anodized SnO_x sponge.

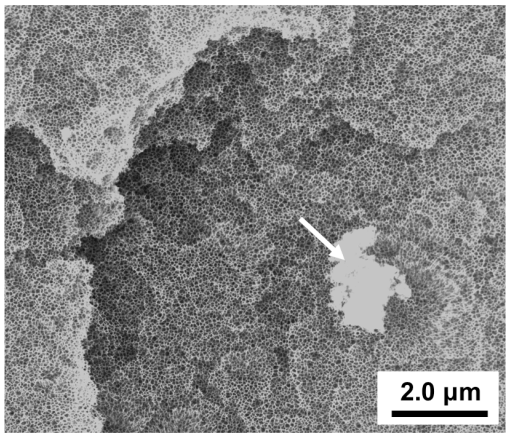

Figure 2.17 SEM image tin foil after anodization in oxalic acid at 10 V for 60 min. with tin oxalate precipitate on the surface (arrow)

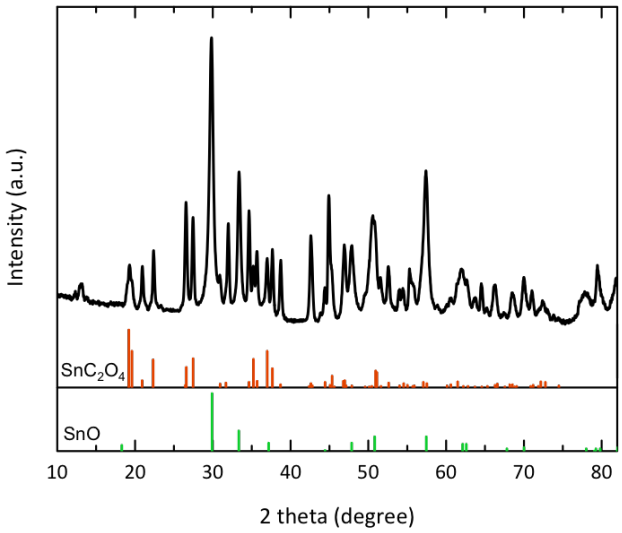

Figure 2.18 X-ray diffraction of tin foil after anodization in oxalic acid at 10 V for 60 min. Reference reflections for tin oxalate (red) and tin oxide (green)

If the anodic bias is increased, pore size increases correspondingly. After 5 minutes, spallation of the porous layer on large domains of the sample occurs (Figure 2.19). Due to increased stress on the film because of a massive increase in oxygen gas evolution visible to the eye, the porous structure is blasted off. A decrease in the anodic bias to less than 5 V leads to a passivation of the surface by precipitation of tin oxalate (Figure 2.20) as reported by Wang *et al.*[18]

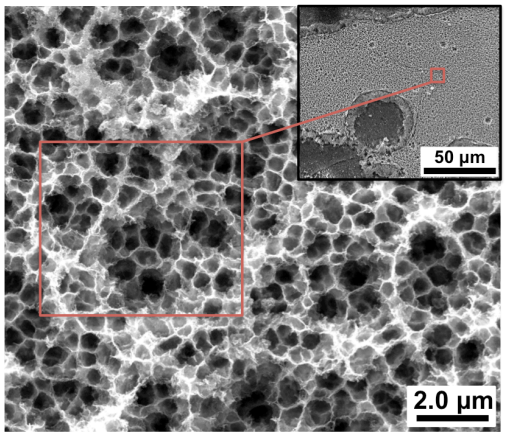

Figure 2.19 SEM image of anodized tin foil in oxalic acid at 30 V for 5 min.

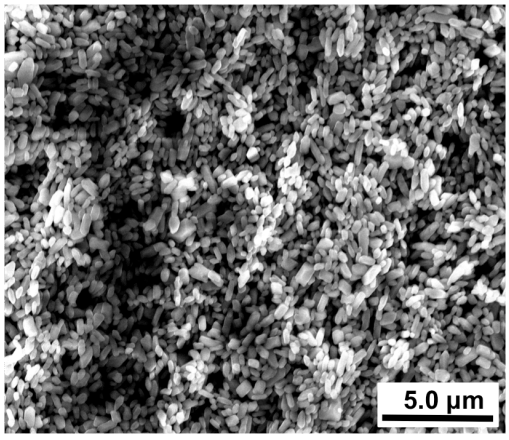

Figure 2.20 SEM image of anodized tin foil in oxalic acid at 2 V for 10 min

Even though anodization in an aqueous oxalic acid solution leads to the formation of a porous structure, the precipitation of tin oxalate occurs. This reaction becomes the dominant one, if the applied bias is decreased. To inhibit this precipitation, the use of a buffered solution with di-potassium oxalate was investigated.

2.4.2 Di-Potassium Oxalate Buffered Solutions

Table 2.2 Anodizations performed in buffered oxalic acid solutions

Solution	c(oxalic acid) / mol/l	c(di-potassium oxalate) / mol/l	Time / min
H_2O	0.25	0.25	10
H_2O	$4*10^{-3}$	0.25	10
H_2O / EG	$4*10^{-3}$	0.25	10
H_2O / EG	$4*10^{-3}$	0.25	60

At a concentration of 0.25 mol/l oxalic acid and di-potassium oxalate, pore walls are frayed and porous as the acid dissolves the oxide material (Figure 2.21). Pore openings are uneven in size with a mean diameter of 46.9 µm and a standard deviation (SD) of 17.2 µm reflecting the inhomogeneity (see Figure 7.1a Appendix). Wall thickness was measured to be 15.8 ± 3.9 µm (see Figure 7.2a Appendix).

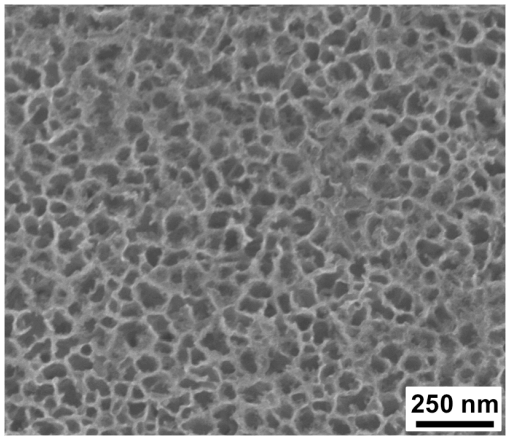

Figure 2.21 SEM image of anodized foil in buffer solution consisting of 3.0 wt% oxalic acid and 4.4 wt% di-potassium oxalate

Decreasing the concentration of oxalic acid diminished the effect. At a concentration of $0.4*10^{-3}$ mol/l oxalic acid and 0.25 mol/l di-potassium oxalate, an evenly porous surface with less frayed walls is produced (Figure 2.22). Pore diameter increases to 60.8 ± 19.1 µm (see Figure 7.1b Appendix). With a higher concentration of oxalic acid and thus an increased dissolution of the oxide, interpore boundaries are attacked resulting in the formation of new pores. By decreasing the concentration of the etchant, pore wall etching is diminished, resulting in an effective increase in pore size. Wall thickness remained constant at 16.1 ± 3.8 µm (see Figure 7.2b Appendix). Additionally, no precipitate of tin oxalate was found on the sample as the buffer solution successfully inhibits the precipitation. Because of the vigorous oxygen evolution, parts of the porous structure splintered resulting in an uneven surface.

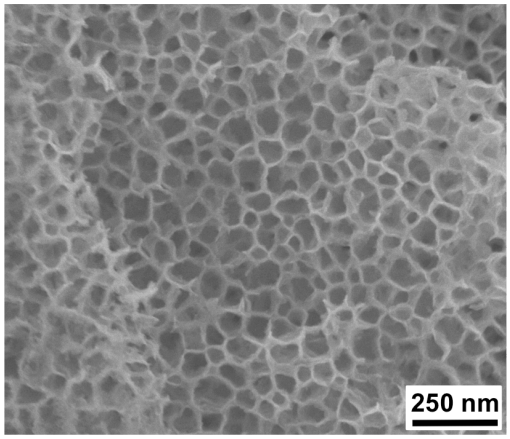

Figure 2.22 SEM image of anodized foil in buffer solution consisting of 0.05 wt% oxalic acid and 4.0 wt% di-potassium oxalate

In order to decrease the size of oxygen bubbles generated as a byproduct of the anodization and to reduce the growth speed of the porous film, due to a slower diffusion in a more viscous solvent, ethylene glycol was added to the buffer solution. Comparison of the anodized surface with a sample after non-buffered anodization

already showed an increase in surface smoothness visible to the eye. In contrast to a rough black surface, reflections of incoming light were visible on the sample. A closer look at the anodized surface reveals the sponge-like structure to be homogeneous with no visible grain boundaries or defects (Figure 2.23).

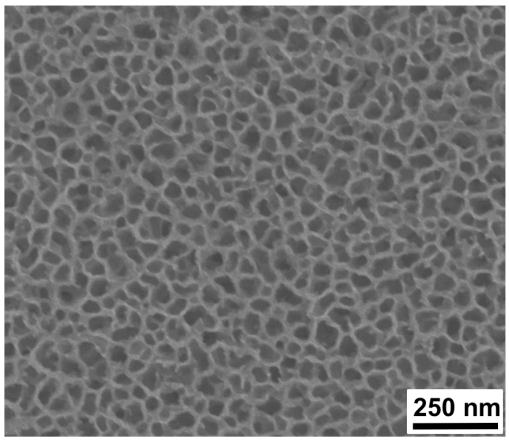

Figure 2.23 SEM image of anodized foil in buffered solution with 33% ethylene glycol after 10 min

Because of the higher viscosity and thus a slower reaction rate, thickness of pore walls is increased to 17.2 ± 3.5 µm (see Figure 7.1c Appendix). Pore size also decreases again to 49.8 µm while homogeneity increases as visible by the slight decrease in SD of 14.7 µm (see Figure 7.2c Appendix). The structure becomes more durable and is able to withstand the stress of volume expansion as the film grows. X-ray diffraction of the porous film revealed the film to consist mainly of tin(II) oxide (Figure 2.24). The diffraction also exhibits an amorphous background originating from amorphous SnO_x in the porous film (see Chapter 5.3.1).

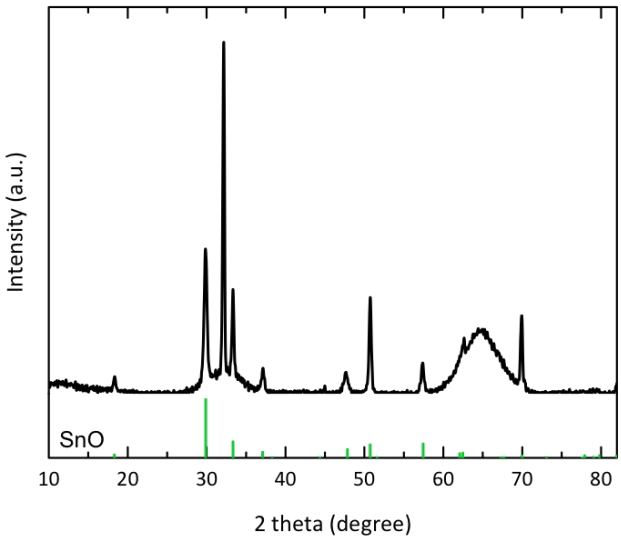

Figure 2.24 X-ray diffraction of tin foil after anodization in buffered electrolyte. Reference reflection of tin(II) oxide (green)

Figure 2.25 shows images of the backside of the anodized sponge and of the underlying tin surface. Backsides of the pores are mostly closed as expected from an anodized structure (see Chapter 1.2). Surface of the underlying tin bulk does show some kind of imprints but in contrast to the regular nature found on the anodized aluminum surfaces, no regular structure is visible. For this reason, a second anodization was not investigated.

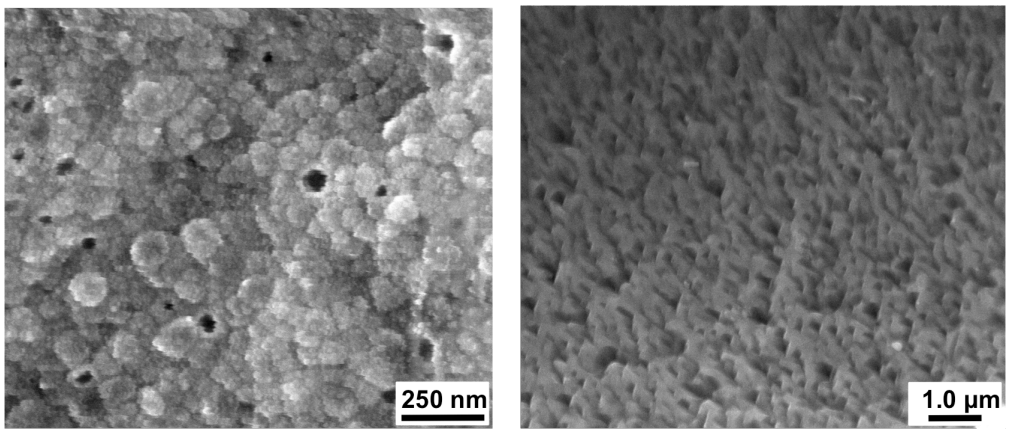

Figure 2.25 SEM image of backside of anodized sponge (left) and imprints in tin bulk (right)

In cross section view, a constant film thickness over the whole sample can be observed, only decreasing close to the edges of the anodized surface. In the first micrometers, beginning from the border of the anodized area, film thickness increases linearly until after 135 µm, a constant thickness is reached (Figure 2.26). The thickness remains constant over the whole sample diameter. This translates into a homogeneous film thickness on 97 % of the sample surface area. Film-thickness was measured to be 26 µm (Figure 2.27).

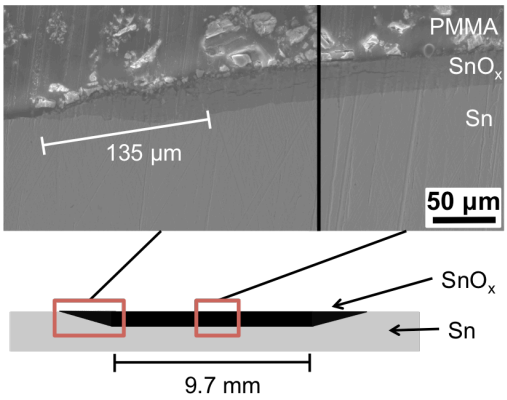

Figure 2.26 Top: Cross section SEM of anodized foil embedded in PMMA at the rim (left) and in the middle (right) of the sample. Bottom: illustration of sample cross section.

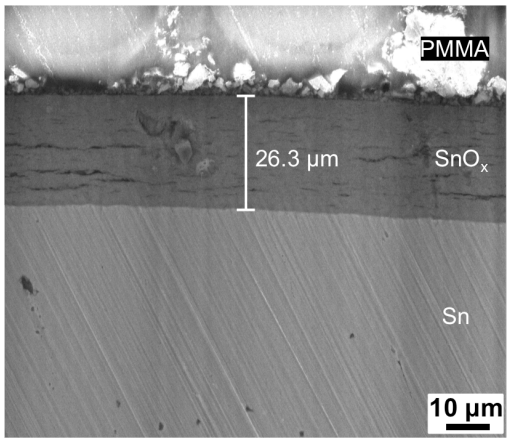

Figure 2.27 Cross section SEM of anodized foil embedded in PMMA.

High-resolution cross section SEM revealed a regular structure of ordered pores arranged in a lamellar manner with a length of ~250 nm (Figure 2.28). Pore diameter remains constant over the whole sample cross section. As mentioned before, the regular cracks in the structure are the result of the stress induced by the constant oxygen evolution. Recently, it was reported by Schmuki *et al.* that anodization in an ammoniumfluoride and sodiumsulfide containing mixture of acetonitrile and water, pore-breaking could be reduced and nanotubes of a length of up to 4.5 µm could be synthesized.[16]

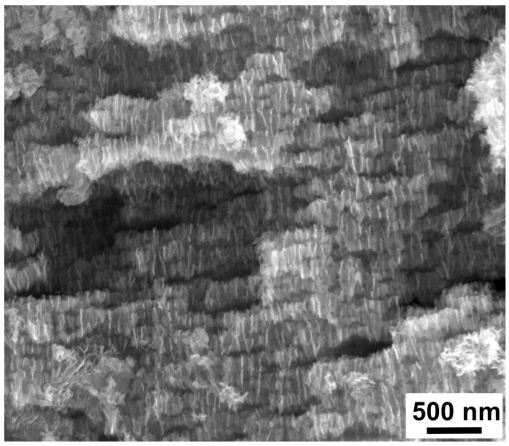

Figure 2.28 High-resolution cross section SEM of anodized tin oxide sponge showing regular alignment of nanopores.

Increasing the reaction time, the structure starts to breaks again as the stress of oxygen evolution becomes too high (Figure 2.29). On a non-tempered sample, cavities had the form of straight lines, originating from the grain boundaries of the underlying tin crystal structure. In contrast to the straight lines, on the tempered sample cavities exhibit random edges since the cavities result from the film breaking apart due to the stress induced by the gas evolution.

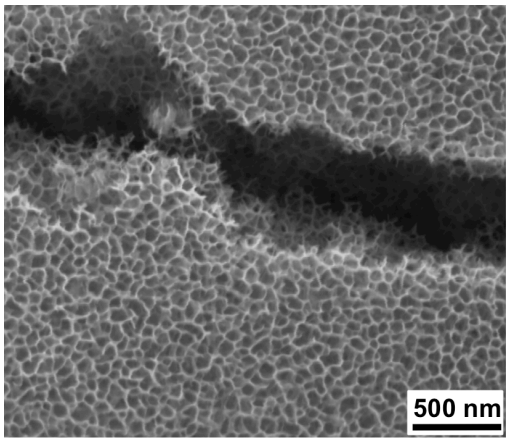

Figure 2.29 SEM image of anodized foil in buffer solution with 33 % ethylene glycol after 60 min.

2.5 Conclusion

An easily reproducible and fast electropolishing method for commercially available tin foils has been established. Using an electrolyte based on alcohols and perchloric acid in combination with a custom made stirring electrode, a single step polish leads to smooth and clean surfaces. Additionally, a three-step electropolishing for tempered samples was established yielding comparably smooth sample surfaces. The second achievement was the vast improvement of film quality of the anodized tin oxide sponge. In the unbuffered aqueous oxalic acid electrolyte, anodization has lead to large trenches at grain boundaries and precipitation of tin oxalate as shown by X-ray powder diffraction. While longer reaction times lead to an uneven surface due to spallation of the sponge, modulation in anodic bias either lead to chipping of the whole porous film or increased precipitation of tin oxalate. By the use of a new, buffered electrolyte solution containing di-potassium oxalate, not only precipitation of tin oxalate was inhibited, but also the evenness and homogeneity of the porous sponge-like structure was increased. In combination with a tempered sample to eliminate defects originating from grain boundaries, macroscopically smooth porous films with an even thickness over the whole anodized surface were achieved.

2.6 References

[1] I. T. Weber, A. Valentini, L. F. D. Probst, E. Longo and E. R. Leite, "Catalytic activity of nanometric pure and rare earth-doped SnO2 samples," *Mater. Lett.*, vol. 62, no. 10–11, pp. 1677–1680, 2008.

[2] A. Y. Jogalekar, R. G. Jaiswal and R. V. Jayaram, "Activity of modified SnO2 catalysts for acid-catalysed reactions," *J. Chem. Technol. Biotechnol.*, vol. 71, no. 3, pp. 234–240, 1998.

[3] J. Kaur, S. C. Roy and M. C. Bhatnagar, "Highly sensitive SnO2 thin film NO2 gas sensor operating at low temperature," *Sensors Actuators, B Chem.*, vol. 123, no. 2, pp. 1090–1095, 2007.

[4] X. Du and S. M. George, "Thickness dependence of sensor response for CO gas sensing by tin oxide films grown using atomic layer deposition," *Sensors Actuators, B Chem.*, vol. 135, no. 1, pp. 152–160, 2008.

[5] J. P. Ahn, J. H. Kim, J. K. Park and M. Y. Huh, "Microstructure and gas-sensing properties of thick film sensor using nanophase SnO2 powder," *Sensors Actuators, B Chem.*, vol. 99, no. 1, pp. 18–24, 2004.

[6] P. Docampo and H. J. Snaith, "Obviating the requirement for oxygen in SnO2-based solid-state dye-sensitized solar cells," *Nanotechnology*, vol. 22, no. 22, p. 225403, 2011.

[7] S. Chappel and A. Zaban, "Nanoporous SnO2 electrodes for dye-sensitized solar cells: Improved cell performance by the synthesis of 18 nm SnO2 colloids," *Sol. Energy Mater. Sol. Cells*, vol. 71, no. 2, pp. 141–152, 2002.

[8] H. Zhang, C. Hu, J. Xu, B. Wan, K. Zhang and X. Li, "SnO2 Nanorods for Light Sensor and UV Detector," *Sens. Lett.*, vol. 9, no. 5, pp. 1643–1648, 2011.

[9] T. Oshima, T. Okuno and S. Fujita, "Thin Film," *Japanese Journal of Applied Physics*, vol. 48, no. 12, p. 120207, 2009.

[10] Y. Idota, "Tin-Based Amorphous Oxide: A High-Capacity Lithium-Ion-Storage Material," *Science*, vol. 276, no. 5317, pp. 1395–1397, 1997.

[11] Y. Yu, C. H. Chen and Y. Shi, "A tin-based amorphous oxide composite with a porous, spherical, multideck-cage morphology as a highly reversible anode material for lithium-ion batteries," *Adv. Mater.*, vol. 19, pp. 993–997, 2007.

[12] S. Yeonmi and L. Seonghoon, "Self-organized regular arrays of anodic TiO2 nanotubes," *Nano Lett.*, vol. 8, no. 10, pp. 3171–3173, 2008.

[13] J. C. Piuppe, *Galvanotechnik*, vol. 95, pp. 2908–2915, 2004.

[14] I. Epelboin, "Über den Mechanismus des Elektropolierens," *Zeitschrift der Elektrochemie, Berichte der Bunsengesellschaft für Phys. Chemie*, vol. 62, pp. 813–818, 1958.

[15] A. Birkel, "Tin (IV) Oxide Nanostructures: Controlled Synthesis, Properties and Applications in Dys-Sensitized Solar Cells," Johannes Gutenberg-University Mainz, 2010.

[16] A. Palacios-Padrós, M. Altomare, A. Tighineanu, R. Kirchgeorg, N. K. Shrestha, I. Díez-Pérez, F. Caballero-Briones, F. Sanz and P. Schmuki, "Growth of ordered anodic SnO2 nanochannel layers and their use for H2 gas sensing," *J. Mater. Chem. A*, vol. 2, p. 915, 2014.

[17] H.-C. Shin, J. Dong and M. Liu, "Porous Tin Oxides Prepared Using an Anodic Oxidation Process," *Adv. Mater.*, vol. 16, no. 3, pp. 237–240, 2004.

[18] M. Wang, Y. Liu, D. Zhang and H. Yang, "Anodization process of Sn in oxalic acid at low applied voltages," *Electrochim. Acta*, vol. 59, pp. 441–448, 2012.

3 Self-Organized Arrays of SnO_2 Lamellae: Synthesis and Growth Mechanism

This Chapter contains an adapted reproduction of a manuscript to be submitted.

3.1 Introduction

Patterned structures, such as arrays of wires, tubes, stripes or rings, are currently a focus of interest because of their scientifically intriguing properties and potential applications in many areas of technology. Many features of materials, in particular of transition metal oxides, become only of practical value when the material is micro- or nanostructured and therefore has a high surface area (e.g. for photoinduced water splitting,[1][2] as photocatalysts for organic degradation,[3][4] self-cleaning substrates[5][6] and solar cell electrodes.[7][8]) or short solid state diffusion paths (e.g. for electrochromic devices[9] or batteries[10]). Many research efforts have been devoted to the design and control of micro- and nanostructures with innovative synthetic strategies.

A great variety of nanostructures have been generated by electrochemical anodization of metals. Al[11][12] and Ti[13][14]) are the most extensively studied metals, and porous nanostructured alumina (Al_2O_3) and titania (TiO_2) can be prepared by electrochemical oxidation of metallic metal substrates under a specific set of environmental conditions.

In analogy to TiO_2, tin dioxide (SnO_2) is a non-toxic wide-gap *n*-type semiconductor that combines high conductivity with high optical transparency in the visible range, making it an important component for optoelectronic applications[15] and as transparent conducting oxide for electrodes in solar cells,[16] gas-sensors,[17][18] catalysts[19] or coatings for architectural glass.[20] In addition, it has the potential to

function as a high capacity anode material for lithium-ion batteries.[21] For many applications (e.g. for dye sensitized solar cells[22]–[24]) SnO_2 is fabricated as a thin film, which can be accomplished by DC magnetron sputtering,[25] chemical vapor deposition,[26] spray pyrolysis[27] or atomic layer deposition (ALD).[28]

In spite of the wealth of applications for SnO_2 there are very few reports on the electrochemical anodization of tin. Jeun *et al.*[29] synthesized irregular nanoporous tin oxide films in 0.3 M oxalic acid solution at 6 V and used it as a gas sensor material. Anodization of tin in oxalic acid solutions at an applied voltage of above 5 V produces highly porous tin oxide structures as described in chapter 2.4. Lower applied voltages lead to a surface passivation by precipitation of tin oxalate.[30] Ono *et al*. studied the formation of porous tin oxide structures in NaOH containing electrolytes and their application in the photocatalytic degradation of methylene blue.[31] Schmuki and coworkers[32] recently introduced an anodization approach in an acetonitrile-water mixture-based electrolyte containing Na_2S and NH_4F to obtain functional, high-aspect ratio, ordered tin oxide films with regular nanochannel structures and top-open pores.

In this chapter it is shown that the anodization of tin at lower applied voltages in buffered solutions leads to the formation of an unusual Sn/SnO_2 lamellar core shell structure and also prevents surface passivation by precipitation of tin oxalate. Composition of the structure and the growth mechanism were investigated in detail.

3.2 Experimental

3.2.1 Materials

All starting materials were used without further purification. Commercially available tin foil with a thickness of 0.25 mm and a purity of 99.998 % was purchased from ABCR. The foil was cut into round plates with a diameter of 15 mm with a hole punch. Polishing solution consisted of n-butanol (99%, Acros Organics), methanol (p.A., Sigma-Aldrich), perchloric acid (Sigma-Aldrich) and MilliQ-water (18.3 ΩM/cm).[33] As part of the electrolyte, oxalic acid (p.A., Merck), di-potassium oxalate (≥ 99 %, Acros) were used.

3.2.2 Synthesis

Prior to electropolishing, the foil was tempered with a heating rate of 5 °C/min and a dwell time of 1 h at 400 °C in a muffle furnace (Nabertherm S27). For electropolishing and anodization, the foil was mounted in a setup consisting of a PTFE-cylinder and a copper block as the anode. For the electropolishing, a solution consisting of 300 mL of methanol (≥ 99.8 %, Sigma-Aldrich), 200 mL of 1-butanol (99 % extra pure, Acros Organics), 29.16 mL of perchloric acid (70% solution in water, Acros Organics) and 4.71 mL of MilliQ-Water were used. A constant anodic bias of 40 V was applied via a Voltcraft PSP 1803 voltage source. A commercially available drilling machine (CMI) equipped with a custom made rotating steel electrode was used as the cathode. The foil was electropolished for 20 s without rotation, 15 s with maximum velocity and finally 7 s without rotation. After electropolishing, the solution was removed, the foil rinsed with MilliQ-Water and air-dried. For anodization, a buffer solution consisting of 0.05 wt% oxalic acid dihydrate (≥ 99.5 %, Sigma-Aldrich), 4.00 wt% di-potassium oxalate monohydrate (for analysis, Emsure ACS, Merck) and deionized water (Millipore) was used. Anodization was carried out under a constant anodic bias of 0 -

2.4 V applied by a Voltcraft Digi 35 voltage source for 24 h. After anodization, the buffer solution was removed, the sample rinsed with deionized water and air-dried. The current was recorded every 10 seconds with a Voltcraft Plus VC960 voltmeter.

3.2.3 Characterization

Scanning electron microscopy (SEM)

Surface topography was analyzed using a high-vacuum mode scanning electron microscope (SEM; FEI Quanta 200 FEG Environmental-SEM, FEI Deutschland GmbH, Frankfurt / Main, Germany) at an acceleration voltage of 15 kV.

Cross section measurement

Samples were embedded in Poly(methyl methacrylate) (PMMA) using DuroFix-2 Kit by Struers GmbH. PMMA cylinder were then cut into disks of approx. 1 mm thickness with an EXAKT 300CP diamond band saw. Disks were glued on Plexiglas slides and polished by Struers RotoPol-31 for 30 seconds with polishing paper of a grain size of 1200 and 2 minutes with a grain size of 4000. Polished samples were then applied to an aluminum stub and measured in SEM using low vacuum mode.

Mössbauer spectroscopy

Mössbauer measurements were performed at room temperature in CEMS mode with constant-acceleration. ^{119}Sn Mössbauer spectrum was measured using a 10 mCi ^{119}Sn ($CaSnO_3$) source. The RECOIL 1.03 Mössbauer analysis software was used to fit the experimental spectrum.

X-ray photoelectron spectroscopy (XPS)

XPS spectra were measured on a PHI 5600 Multi-Technique XPS (Physical Electronics, Lake Drive East, Chanhassen, MN) using monochromatized Al Kα at 1486.6 eV. Atomic concentrations were calculated using MULTIPAK 9.4.1.2 software. Peak fitting was performed with CASA XPS Version 2.3.14 software.

X-ray diffraction (XRD)

The crystal structure of tin was examined via room temperature X-ray diffraction on a Bruker D8 Discover instrument operated in reflection geometry with a MoK$\alpha_{1,2}$ X-ray source.

3.3 Results and Discussion

3.3.1 Structural and physical characterization of the anodization layer

The anodization of Sn metal in the buffer solution at 2.0 – 2.2 V for 24 h resulted in the formation of a new lamellar structure as shown in the inset in Figure 3.1a. The lamellae show a homogeneous, macroscopic ordering over a range of approx. 80 mm^2.

On rotating and tilting the foil, a tunable reflectivity was observed (see digital images in Figure 3.1b,c). When the view direction is perpendicular to the surface of the SnO_2 structure, incoming light is reflected from the smooth surfaces of the lamellae. Thus, the reflectivity of the sample is high, and it appears bright silver. The reflectivity decreases when the foil is tilted. When the incident light is parallel to the surface of the lamellae, it is reflected into the interior of the structure or scattered way from it, *i.e.* the reflectivity is low and the sample appears dark. A similar effect is observed when the sample is rotated. However, as the layers are tilted with respect to the sample surface, the difference in reflectivity is less pronounced.

The lamellae consist of a core shell structure with a shell of SnO_2 and a core of Sn. The Mössbauer spectrum (Figure 3.2) exhibits a doublet with high intensity, which was assigned to the Sn^{4+} species of the surface layer. The underlying tin was associated to the singlet of lower intensity. At a penetration depth for Mössbauer analysis in CEMS mode of about 100 nm, we estimate the thickness of the SnO_2 shell to be less than 90 nm.

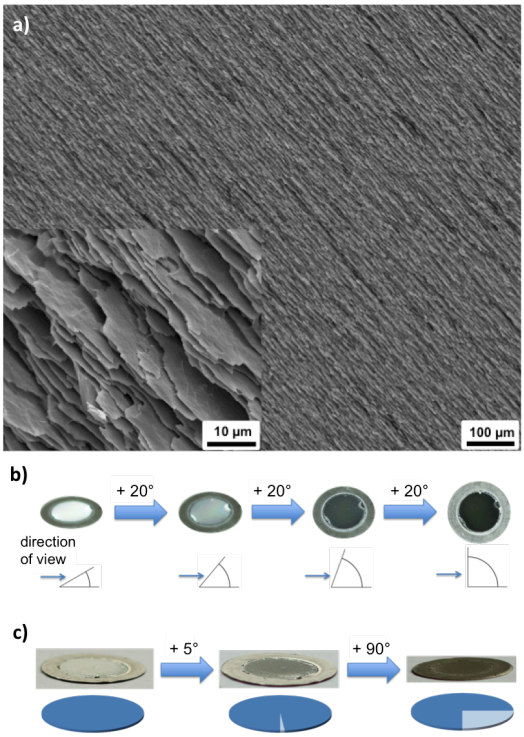

Figure 3.1 (a) SEM image showing the lamellar arrangement of SnO_2 with inset at higher magnification. (b-c) Digital images of the optical behavior of the anodized foil.

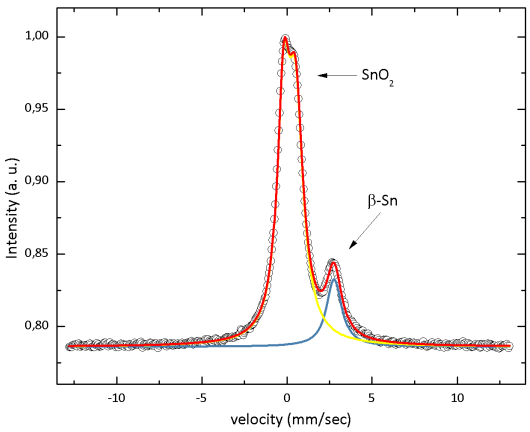

Figure 3.2 Mössbauer spectrum of the anodized surface. Measurement and data treatment were performed by [redacted]

XPS was used to corroborate the Mössbauer spectroscopy results. The spectrum of the anodized surface shows two peaks of high intensity corresponding to 3d3 and 3d5 signals of Sn^{4+} (Figure 3.3a). Both peaks exhibit shoulders at lower binding energies corresponding to the underlying tin bulk. Peak fitting resulted in a contribution of 93.91 % for Sn^{4+} (see Table 7.1 Appendix).

The oxygen 1s signal shows no shoulder and high intensity (Figure 3.3b) which points to a single oxidic species on the surface of the sample. Atomic concentration calculation resulted in 33.0 % Sn3d5 and 67.0 % O1s. The SEM image (Figure 3.3c) shows rough edges of the horizontal lamellae. After sputtering, intensity of both Sn^{4+} peaks decreases, only visible as shoulders in the peaks of elemental Sn (Figure 3.3d). Peak fitting resulted in a residue of 10.0 % Sn^{4+} (see Table 7.2 Appendix).

The oxygen 1s signal was weak and decreased (Figure 3.3e). Atomic concentration calculations resulted in 96.9 % Sn3d5 and 3.1 % O1s. The SEM image after sputtering shows a smooth surface (Figure 3.3f). The remaining signal of SnO_2 can be associated with regions below the edges of the plates. Due to the angle of the ion gun with

respect to the sample, some regions were shielded by the plates from incoming Ar ions. As the X-ray source and the detector were mounted at different angles, the non-sputtered regions were visible in the spectrum. In summary, the results show that the lamellae consist of a SnO_2 shell with a core of unreacted tin.

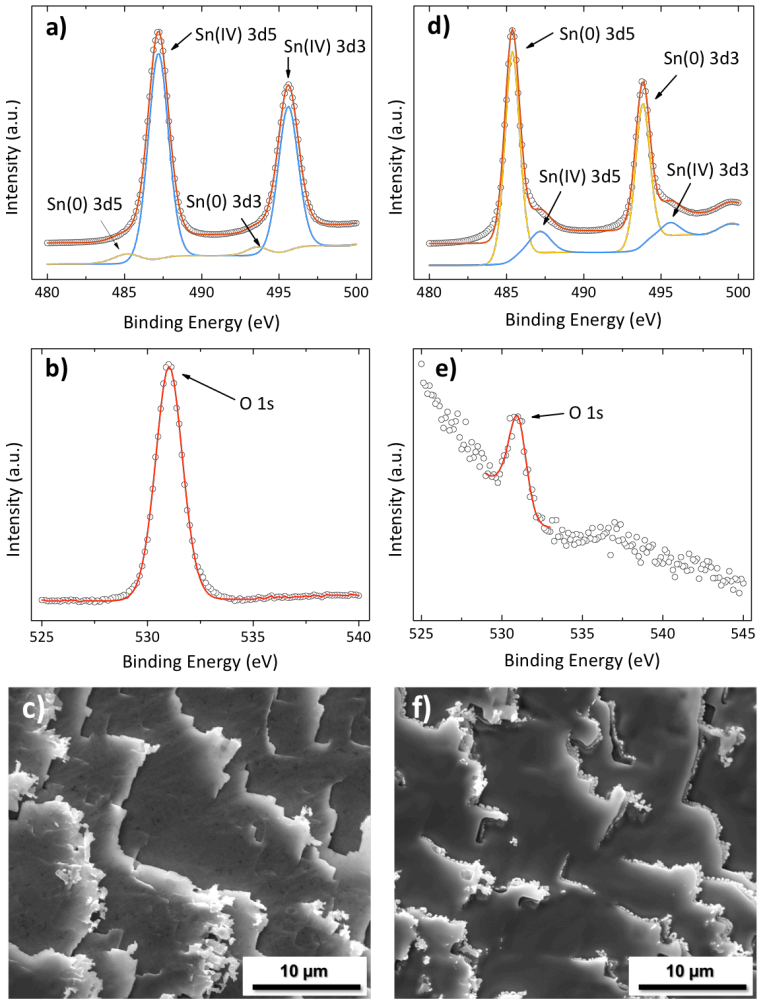

Figure 3.3 XPS spectra and corresponding SEM images of the anodized tin surface before (a-c) and after (d-e) sputtering.

3.3.2 Growth mechanism of the SnO_2 lamellae

The growth direction of the lamellae is correlated to the orientation of the underlying crystal domains. This was first demonstrated with a low-temperature annealed tin foil (155°C for 80h instead of 400 °C for 1h). This leads to a growth of the grains but not a wide-ranging ordered alignment of the crystal structure (as achieved at 400°C). After anodization, several domains appeared, as illustrated by the altered reflectivity at different sample areas in Figure 3.4 (right). Variance in reflectivity corresponds to different orientations of the lamellae with respect to the surface. X-ray micro-diffraction (micro-XRD) measured in four different areas exhibit the reflections exclusively attributed to β-Sn. Yet, the X-ray intensities are strongly biased by texture effects, *i.e.* the orientation of the underlying Sn core of the lamellae (Figure 3.4, left). Bragg intensities of the SnO_2 shell could not be detected, because it is too thin thus the corresponding reflections were too weak. The variation in optical reflectivity due to the orientation of the lamellae, however, shows that the direction of the individual domains varies with respect to the orientation of the crystal structure.

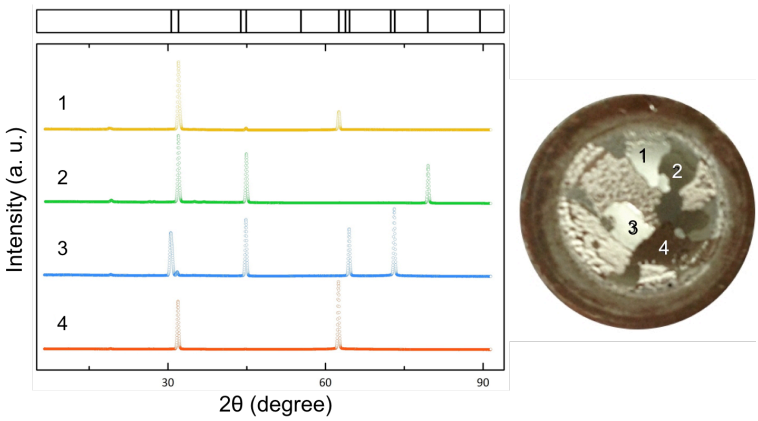

Figure 3.4 Left: XRD pattern of the anodized tin surface on four different spots after low temperature annealing followed by anodization for 24 hours at 2 V. The PDF reference 00-004-0673 for β-Sn is given in the top trace. Right: Digital image of the surface of the anodized Sn foil. The numbers mark the points where the diffractograms were measured.

After tempering at 400°C and electropolishing, tin foils are still polycrystalline but with a high degree of orientation alignment over the whole sample. X-ray diffraction pattern exhibits no Debye-Scherrer rings but isolated, partly split reflections resembling the pattern of a mosaic crystal. When the surface normal of a polished foil was in the diffraction plane, exclusively (101), (211) and (312) reflections were observed in the range from $20° < 2\theta < 90°$. Upon inclining the sample by 20°, all remaining reflections fulfilled the Laue condition on specific ϕ and χ angles and thus were observed (see Figure 7.3-9, Appendix). From the splitting of the (101) reflection, the spatial deviation angle was determined to be about 0.1°.[34] The (101) reflections were inclined by 7.8° and 9.8° with respect to the diffraction plane. As the (101) set of lattice planes includes an angle of 28.3° with the (001) set of lattice planes,[35] one may estimate the tetragonal axis to be inclined by approximately 20° with respect to the surface normal. After anodization of the sample, scanning electron microscopy showed a view direction parallel to the orientation of the layer structure upon tilting the sample by 70° (Figure 3.5). The (001)-axis is perpendicular to the surface of the layers and at an angle of about 20 degrees to the surface normal. The plane spanned by (100) and (101) axis is parallel to the surface of the layers and at an angle of about 70 degrees to the surface normal. This results in a direction of view in the direction of the plane if the sample is tilted by 70° (Figure 3.6). The resulting 90 degree angle between the tetragonal axis of the crystal structure and the orientation of the layers shows the growth of the layer structure to be along the *a,b* plane of the sample

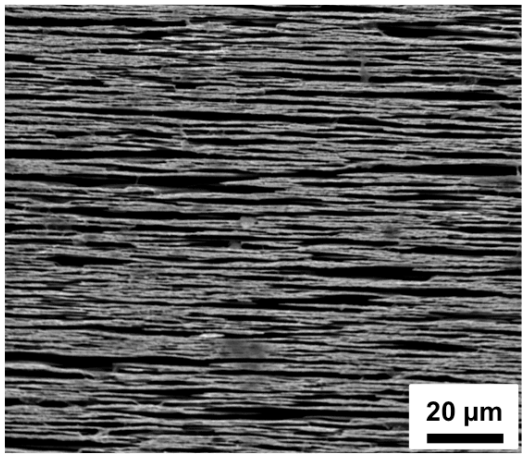

Figure 3.5 SEM image of the layer structure at an angle of 70° to the surface normal

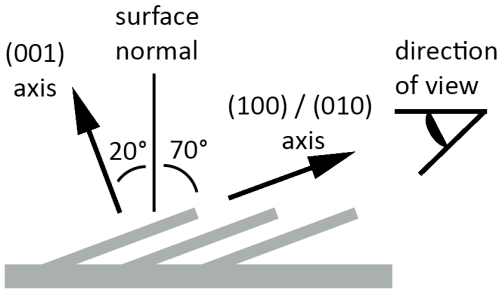

Figure 3.6 Scheme showing the direction of the crystal axis ant direction of view of the SEM image.

The lattice parameters of β-Sn are a = b = 0.583 nm and c = 0.318 nm.[36] The corresponding diffusivity and electrical resistivity of tin along these two directions are: $D_{a,b}$ = 1.3 x 10^{-16} m^2/s, $\rho_{a,b}$ = 13.3 x 10^{-8} Ωm, D_c = 5.0 x 10^{-17} m^2/s, ρ_c = 20.3 x 10^{-8} Ωm.[37] We assume that the anisotropic conductivity leads to a faster oxidation and dissolution of tin in the *a,b* plane, which in turn leads to the formation of the lamellar structure. Supporting this thesis is the investigation of Lucas *et al.* on single crystalline β-Sn.[38] The study revealed that if a single crystal electrode is cycled in

an electrolyte, the Sn(001) surface quickly develops a thin, homogeneous passivation layer significantly inhibiting further reaction. The Sn(100) surface is not able to form such an effective passivation layer and continues to react with the electrolyte.

It was possible to visualize the correlation between orientation of crystal structure and direction of lamellae by applying polishing solution for 30 seconds to the cross section of an anodized sample. Due to faster dissolution of tin in the *a,b* plane, cavities were etched into the surface (Figure 3.7). The direction of the cavities was the same as the lamellae, thus showing the relation between crystal structure and orientation of the lamellae as projected by the XRD measurement.

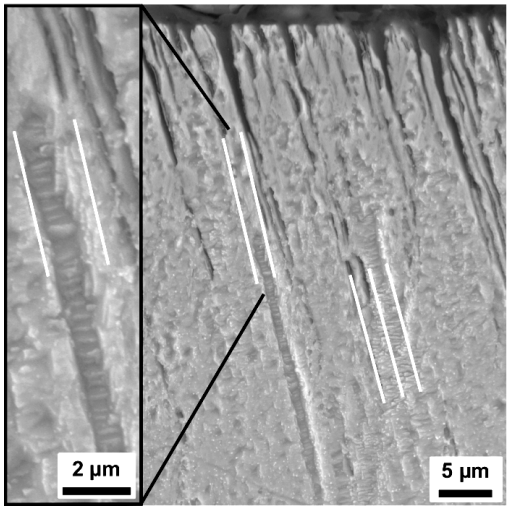

Figure 3.7 Cross section SEM images of anodized samples after application of polishing solution. Right: Several cavities etched over a wide range into bulk material parallel to the growing direction of the lamellae. Left: Detailed view of a cavity showing the parallel alignment to the lamellae.

Cross sections of embedded samples revealed three stages of the growth mechanism as highlighted in a typical current curve in Figure 3.8. A scheme of the different stages of growth in cross section view is shown in Figure 3.9.

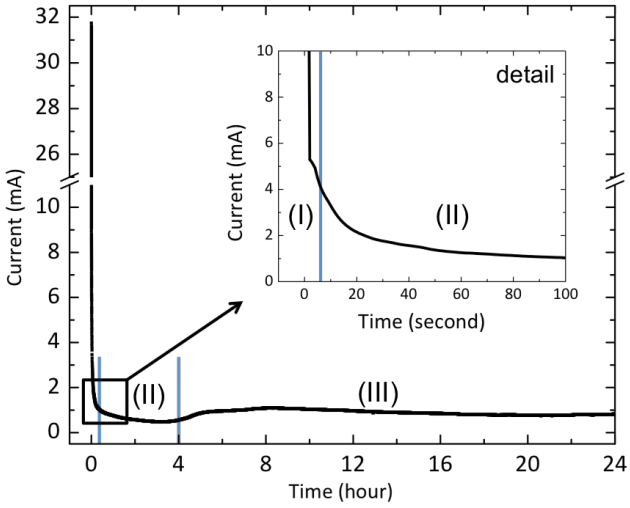

Figure 3.8 Current curve of anodization. Blue lines indicating three stages of the reaction. (I) Surface passivation of tin. (II) Formation of blade-like structure. (III) Transformation of blades to lamellae.

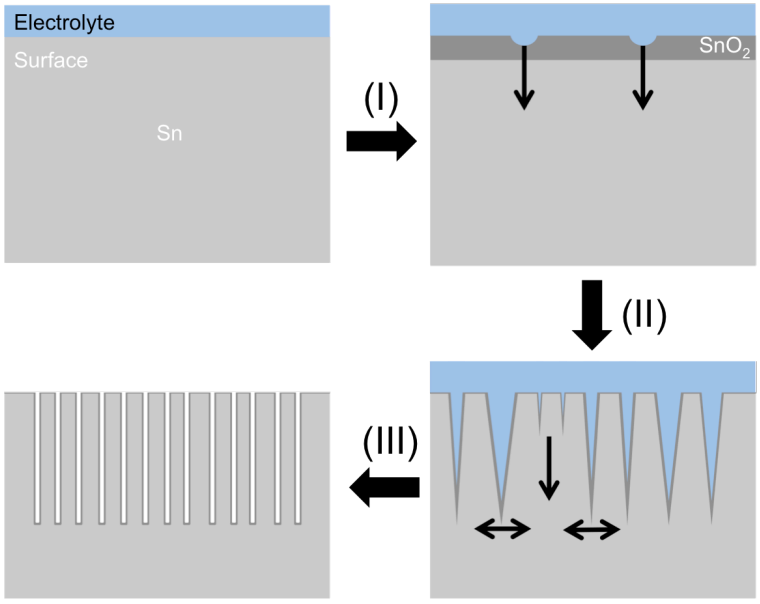

Figure 3.9 Scheme of three-step growth mechanism. (I) Passivation of the surface, (II) formation of blade-like structure and (III) formation of lamellae.

After electropolishing, the surface of the sample is smooth. Top view SEM images of the polished surface exhibits no contrast *i.e.* no height differences (Figure 3.11a). Cross section view shows a straight border between tin metal and the embedding PMMA (Figure 3.11b). In the first stage of the reaction, the surface is passivated (I). This leads to an initial drop in current but only minor changes in surface topography, as grain boundaries become visible (Figure 3.10).

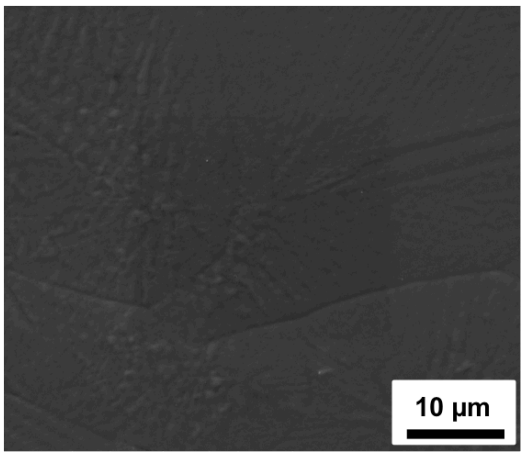

Figure 3.10 SEM image of passivated tin surface after anodization for 7 seconds.

In the second step between 7 seconds and four hours, arrays of blade-like structures are formed (II). The slope of the current curve decreases as tin on the surface is dissolved, beginning at the grain boundaries. After 30 seconds, cavities, all elongated along the same axis, indicated by the arrow in Figure 3.11c, occur. Cross section view reveals the cavities to be less than 1 micrometer deep, only visible as an uneven surface (Figure 3.11d). Below, tin is dissolved and after 30 minutes, arrays of a blade-like structure with tapered tips and a mean length of 6.3 µm become visible (Figure 3.11f). At some regions, the surface layer is already dissolved, exposing some of the structure below (Figure 3.11e). As the reaction continues, the v-shaped trenches

(lines in Figure 3.11h) between the blades propagate into the bulk while large, unetched domains remain (arrows in Figure 3.11h). After 4 hours, the mean length of the blades reaches 12 µm. Mean thickness of the blades is 2.6 µm with a standard deviation (SD) of 1.6 µm (see Figure 7.10a Appendix). The surface layer is completely dissolved, revealing rough edges of the blades (Figure 3.11g). The minimum of the current curve is reached.

In the third step, between 4 and 24 hours, lamellae are formed (III). A minor effect of the long etching time is smoothing of the blade edges (compare Figure 3.11i-k). The more significant effect is, however, the formation of new channels in the large domains of the previously unaffected substrate. These new trenches lead to the formation of an evenly distribution of the blades thus leading to the homogeneously etched surface (arrows Figure 3.11j). Mean thickness of the blades decreases to 1.5 µm while the SD also decreases to 0.8 µm reflecting the narrowed distribution in breadth (see Figure 7.10b Appendix). At the same time widening of the trench tails and smoothing of the blade surfaces with only minor increase in length can be observed (Figure 3.11l). Thus, the diameter of the trenches becomes more uniform over the entire length. Both effects combined lead to the transformation of the blade-like structure into the final lamellae structure with homogeneous thickness as shown in higher magnification in Figure 3.11m. After 24 hours, the lamellae show a mean thickness of 1.6 µm and a SD of 0.7 µm (see Figure 7.10c Appendix) with a mean length of 31.2 µm.

Longer reaction times lead to a gradual destruction of the regular lamellar structure. After 48 hours, ongoing dissolution of the lamellae leads to a rough surface (Figure 3.11n). 24 hours later, only fragments of the former structure remain (Figure 3.11o-p). The lamellae are almost completely dissolved.

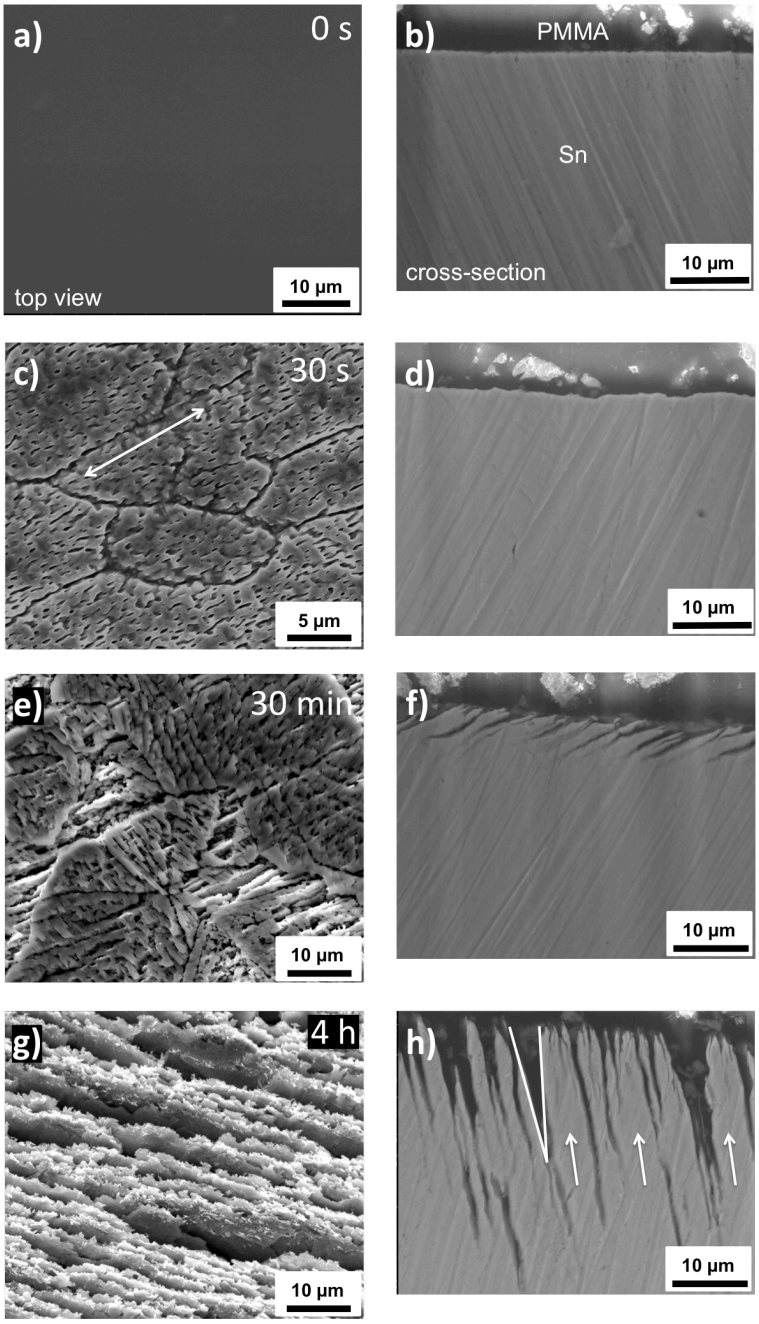

Figure 3.11.1 Top view and cross section SEM images of tin samples after different anodization times.

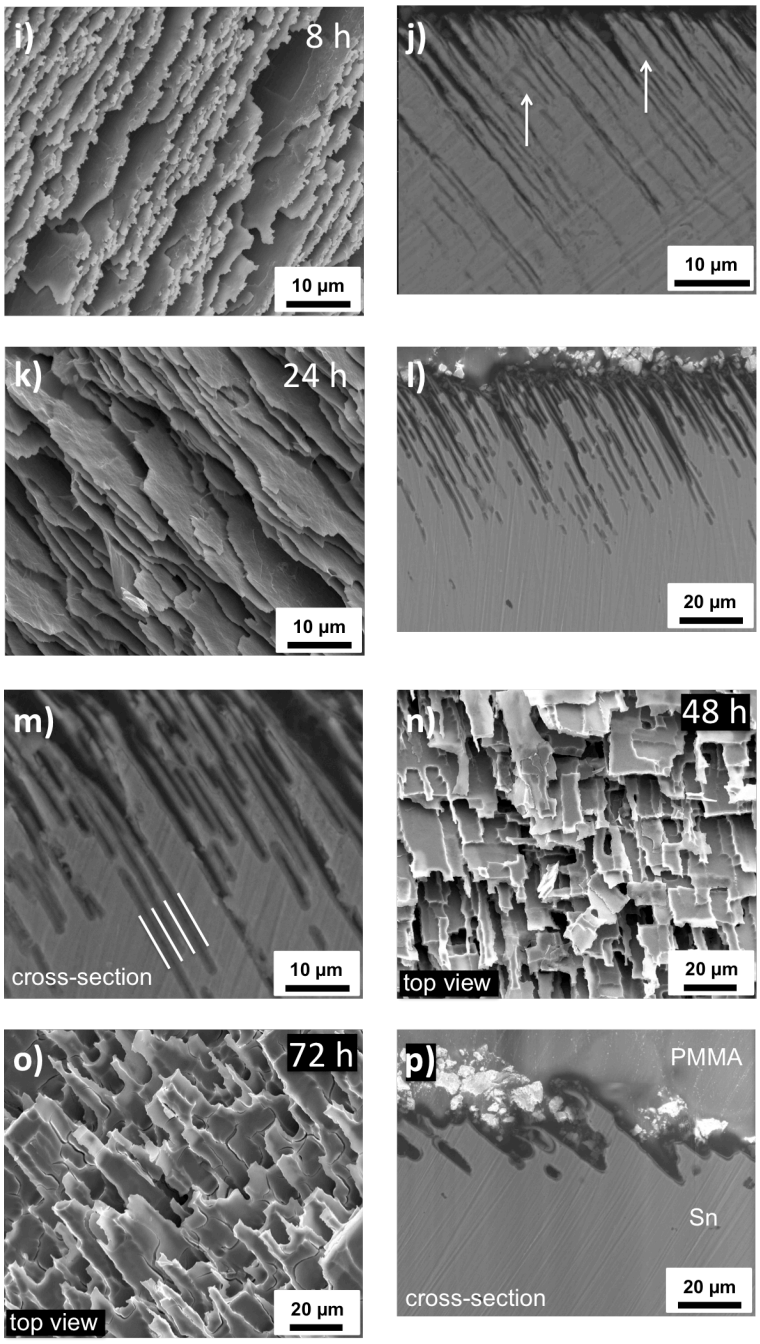

Figure 3.11.2 Top view and cross section SEM images of tin samples after different anodization times.

The difference in orientation of the crystal structure, thus the orientation of the forming lamellae, leads to significant differences in the current curves. This could be used to predict the orientation of the lamellae with respect to the surface. Current curves of three anodizations for samples with horizontal, diagonal and vertical orientations of the lamellae are shown in Figure 3.12a.

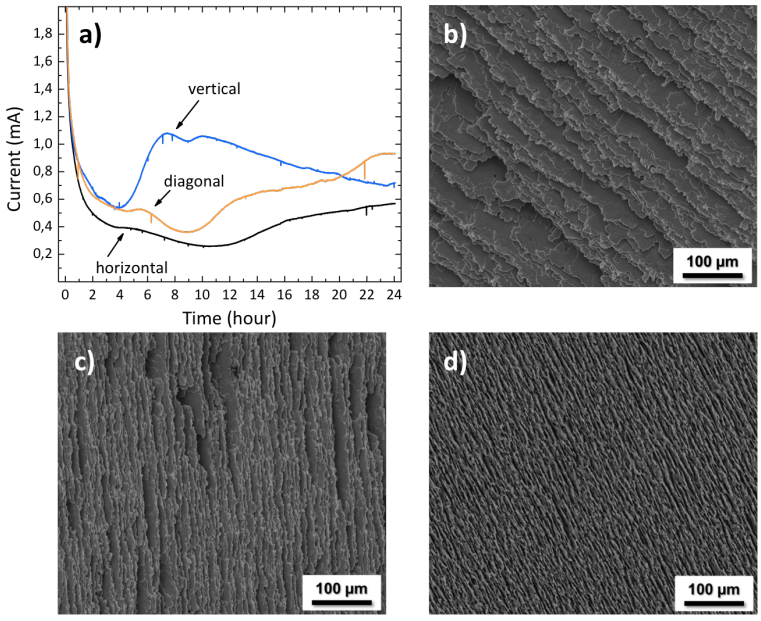

Figure 3.12 Comparison of the current curves for the anodization and different orientations of the lamellae. (a) Current curves of three anodizations at 2 V for 24 hours. (b-d) Corresponding SEM images of the surfaces in (b) horizontal, (c) diagonal and (d) vertical orientation with respect to the surface.

The current minimum is caused by a passivation of the tin surface. In the subsequent step the oxide surface layer is etched. Up to four hours, there seems to be an equilibrium between current required for the oxidation of tin and increase in conductivity due to increased surface thus the current is constant. After 4h, length of the lamellae only slowly increases, minimizing the material transport necessary for the reaction. At this stage, splitting of thick blades and the subsequent increase in

surface leads to an increase in current. Samples with horizontally oriented lamellae have the smallest increase in surface area and accordingly the lowest current (Figure 3.12b). Lamellae with a diagonal orientation (Figure 3.12c) have a larger surface area and therefore lead to higher currents. Vertically oriented lamellae show the highest increase in surface area and therefore the biggest jump in current (Figure 3.12d). With increasing anodization time, the surface area increases as well, which eventually leads to a steadily increasing current. The current of the vertically orientated lamellae decreases eventually as the vertical structure gradually collapses. This leads to a loss of surface area and consequently to a decrease in the current. In order to further understand the growth mechanism, the anodic bias was modulated. When the sample was left in the buffer solution without applying an anodic bias, the surface suffered from acid corrosion and shallow trenches were etched into the sample along the direction of the lamellae (Figure 3.13a). An anodic bias started the anodization. At a bias voltage of up to 1.0 V the anisotropic conductivity is not sufficient to induce the formation of lamellae. Rather, a rough surface consisting of micrometer-sized anisotropic Sn particles is formed (Figure 3.13b), the long axis being directed within the *a*,*b* plane of the crystal structure. At 1.2 V, the difference in the oxidation velocity due to the anisotropic conductivity is large enough to allow the formation of lamellae (Figure 3.13c). However, etching at intermediate voltages induced a sizeable surface roughness and the surface exhibits a large defect density (Figure 3.13d). With increasing anodic bias the rate of the directed etching increased. Figure 3.13e-f shows that at 1.8 V distinct SnO_2 lamellae with rough edges were formed. In the optimum bias voltage range of 2.0 – 2.2 V, an ordered array of lamellae structure without apparent defects was formed (Figure 3.13g). Further increase in the bias voltage leads to the precipitation of tin oxalate by reaction of the stannate intermediate that was formed during the anodization with the oxalic acid etchant (Figure 3.13h).

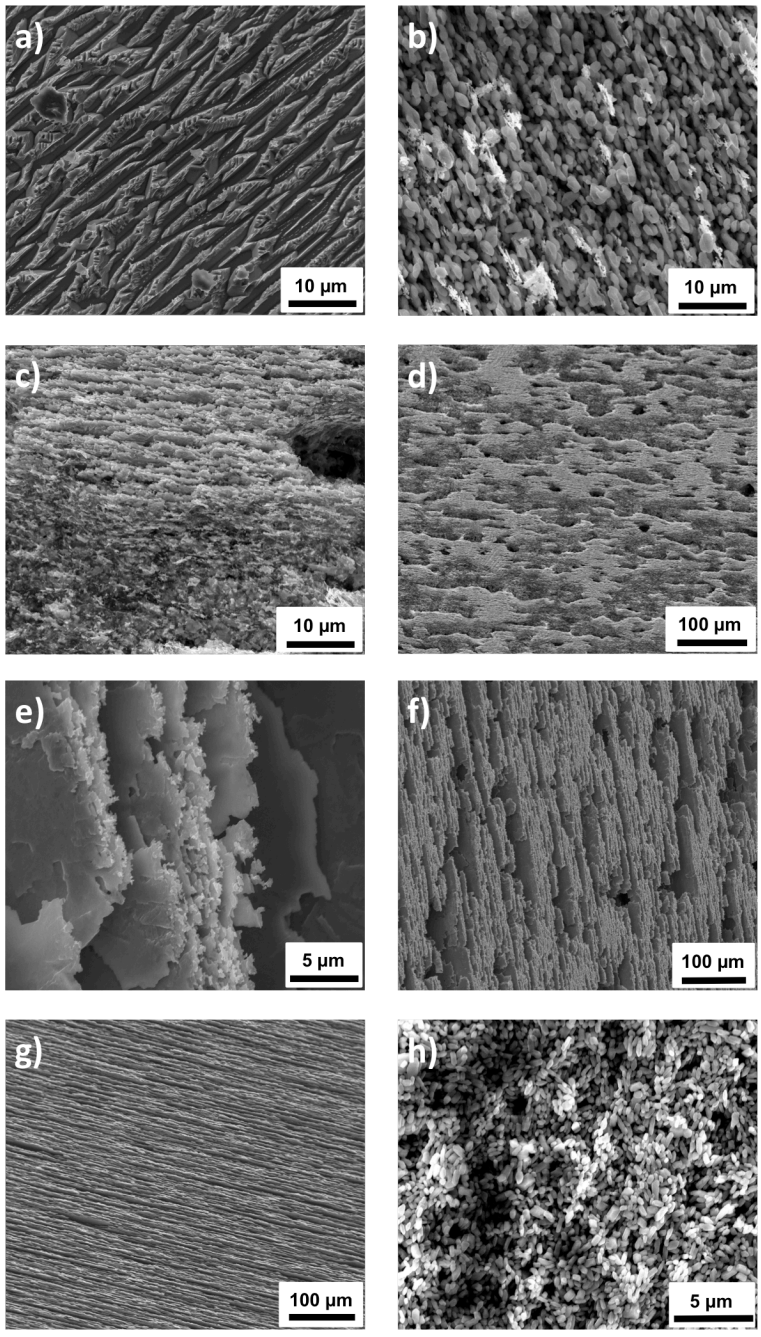

Figure 3.13 Variation of the applied anodic bias from 0 to 2.3 V.

For a better understanding of the role of the electrolyte in the reaction, we anodized samples using different concentrations of oxalic acid. A concentration of 0.05 wt%, anodization leads to the already mentioned homogeneous lamellar structure. Decreasing the amount of oxalic acid leads to a passivation of the surface (Figure 3.14a). The non-optimal composition of the buffer solution is not capable of inhibiting the precipitation of tin oxalate thus allowing the formation of lamellae. Increasing the amount of oxalic acid produces lamellae but with jagged edges and a high degree of defects (Figure 3.14b). The acid dissolves the edges of the lamellae faster preventing the formation of a homogeneous structure.

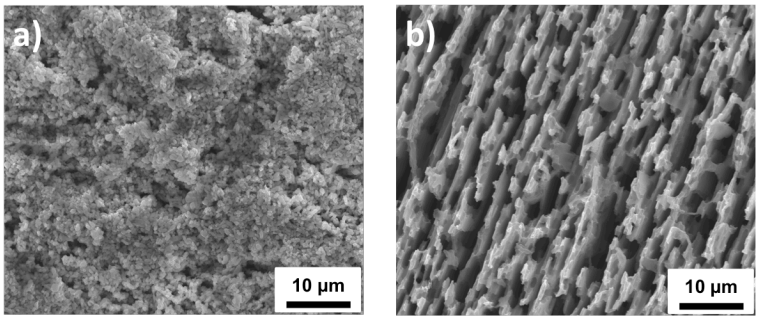

Figure 3.14 Surface of anodized tin foil with lower (a) and higher (b) concentration of oxalic acid.

3.4 Conclusions

In summary, it was demonstrated that a macroscopically homogeneous, nanostructured SnO_2 structure with a surface roughness depending on the bias voltage can be fabricated by anodization of tin in a buffer solution of oxalic acid and di-potassium oxalate. The anodization layer has a thickness of approx. 90 nm and consists of SnO_2 microplates arranged in a lamellar manner with an Sn core as demonstrated by Mössbauer and XPS-spectroscopy. The regular surface structure was demonstrated by the reflectivity of the sample upon rotation and tilting in combination with scanning electron microscopy. The growth direction of the lamellae is correlated to the orientation of the underlying Sn crystal domains. The lamellae growth can be divided into three steps. After passivation of the surface, a blade-like structure is formed which subsequently is transformed into lamellae. Comparison of the current curves makes it possible to predict the orientation of the lamellae.

3.5 References

[1] A. Fujishima and K. Honda, "Electrochemical photolysis of water at a semiconductor electrode.," *Nature*, vol. 238, no. 5358, pp. 37–38, 1972.

[2] J. H. Park, S. Kim and A. J. Bard, "Novel carbon-doped TiO 2 nanotube arrays with high aspect ratios for efficient solar water splitting," *Nano Lett.*, vol. 6, no. 1, pp. 24–28, 2006.

[3] M. R. Hoffmann, M. R. Hoffmann, S. T. Martin, S. T. Martin, W. Choi, W. Choi, D. W. Bahnemannt and D. W. Bahnemannt, "Environmental Applications of Semiconductor Photocatalysis," *Chem. Rev.*, vol. 95, no. 1, pp. 69–96, 1995.

[4] A. Fujishima, X. Zhang and D. A. Tryk, "TiO2 photocatalysis and related surface phenomena," *Surface Science Reports*, vol. 63, no. 12, pp. 515–582, 2008.

[5] A. Fujishima and D. Kagaku, "Self-cleaning effect using TiO2 photocatalyst," *Electrochemistry*, vol. 64, pp. 1052–1055, 1996.

[6] I. P. Parkin and R. G. Palgrave, "Self-cleaning coatings," 2005.

[7] B. O'Regan and M. Grätzel, "A low-cost, high-efficiency solar cell based on dye-sensitized colloidal TiO2 films," *Nature*, vol. 353, no. 6346, pp. 737–740, 1991.

[8] J. N. Tiwari, R. N. Tiwari and K. S. Kim, "Zero-dimensional, one-dimensional, two-dimensional and three-dimensional nanostructured materials for advanced electrochemical energy devices," *Progress in Materials Science*, vol. 57, no. 4, pp. 724–803, 2012.

[9] C. Santato, M. Odziemkowski, M. Ulmann and J. Augustynski, "Crystallographically oriented mesoporous WO3 films: Synthesis, characterization, and applications," *J. Am. Chem. Soc.*, vol. 123, no. 43, pp. 10639–10649, 2001.

[10] A. S. Aricò, P. Bruce, B. Scrosati, J.-M. Tarascon and W. van Schalkwijk, "Nanostructured materials for advanced energy conversion and storage devices.," *Nat. Mater.*, vol. 4, no. 5, pp. 366–377, 2005.

[11] H. Masuda and K. Fukuda, "Ordered metal nanohole arrays made by a two-step replication of honeycomb structures of anodic alumina.," *Science*, vol. 268, no. 5216, pp. 1466–1468, 1995.

[12] F. Li, L. Zhang and R. Metzger, "On the growth of highly ordered pores in anodized aluminum oxide," *Chem. Mater.*, vol. 10, no. 28, pp. 2470–2480, 1998.

[13] J. M. Macak, H. Tsuchiya, L. Taveira, S. Aldabergerova and P. Schmuki, "Smooth anodic TiO2 nanotubes," *Angew. Chemie - Int. Ed.*, vol. 44, no. 45, pp. 7463–7465, 2005.

[14] A. Ghicov and P. Schmuki, "Self-ordering electrochemistry: a review on growth and functionality of TiO2 nanotubes and other self-aligned MO(x) structures.," *Chem. Commun. (Camb.)*, pp. 2791–2808, 2009.

[15] T. T. Emons, J. Li and L. F. Nazar, "Synthesis and characterization of mesoporous indium tin oxide possessing an electronically conductive framework," *J. Am. Chem. Soc.*, vol. 124, no. 29, pp. 8516–8517, 2002.

[16] F. Yang and S. R. Forrest, "Organic Solar Cells Using Transparent SnO2-F Anodes," *Adv. Mater.*, vol. 18, no. 15, pp. 2018–2022, 2006.

[17] A. Kolmakov, Y. Zhang, G. Cheng and M. Moskovits, "Detection of CO and O2 using tin oxide nanowire sensors," *Adv. Mater.*, vol. 15, no. 12, pp. 997–1000, 2003.

[18] E. R. Leite, I. T. Weber, E. Longo and J. A. Varela, "A New Method to Control Particle Size and Particle Size Distribution of SnO2 Nanoparticles for Gas Sensor Applications," *Adv. Mater. Commun.*, no. 13, pp. 965–968, 2000.

[19] I. T. Weber, A. Valentini, L. F. D. Probst, E. Longo and E. R. Leite, "Catalytic activity of nanometric pure and rare earth-doped SnO2 samples," *Mater. Lett.*, vol. 62, no. 10–11, pp. 1677–1680, 2008.

[20] M. Vergöhl, N. Malkomes, T. Matthée, G. Bräuer, U. Richter, F. W. Nickol and J. Bruch, "In situ monitoring of optical coatings on architectural glass and comparison of the accuracy of the layer thickness attainable with ellipsometry and photometry," *Thin Solid Films*, 2001, vol. 392, no. 2, pp. 258–264.

[21] Y. Wang, I. Djerdj, B. Smarsly and M. Antonietti, "Antimony-doped sno2 nanopowders with high crystallinity for lithium-ion battery electrode," *Chem. Mater.*, vol. 21, no. 14, pp. 3202–3209, 2009.

[22] L. Vayssieres and M. Graetzel, "Highly ordered SnO2 nanorod arrays from controlled aqueous growth," *Angew. Chemie - Int. Ed.*, vol. 43, no. 28, pp. 3666–3670, 2004.

[23] H. J. Snaith and C. Ducati, "SnO2-Based dye-sensitized hybrid solar cells exhibiting near unity absorbed photon-to-electron conversion efficiency," *Nano Lett.*, vol. 10, no. 4, pp. 1259–1265, 2010.

[24] A. Birkel, Y.-G. Lee, D. Koll, X. Van Meerbeek, S. Frank, M. J. Choi, Y. S. Kang, K. Char and W. Tremel, "Highly efficient and stable dye-sensitized solar cells based on SnO2 nanocrystals prepared by microwave-assisted synthesis," *Energy & Environmental Science*, vol. 5, no. 1, p. 5392, 2012.

[25] C. Jin, T. Yamazaki, K. Ito, T. Kikuta and N. Nakatani, "H2S sensing property of porous SnO2 sputtered films coated with various doping films," *Vacuum*, vol. 80, no. 7 SPEC. ISS., pp. 723–725, 2006.

[26] J. Pena, J. Perez-Pariente and M. Vallet-Regi, "Textural properties of nanocrystalline tin oxide obtained by spray pyrolysis," *Journal of Materials Chemistry*, vol. 13, no. 9, p. 2290, 2003.

[27] J. Sundqvist, J. Lu, M. Ottosson and A. Hårsta, "Growth of SnO2 thin films by atomic layer deposition and chemical vapour deposition: A comparative study," *Thin Solid Films*, vol. 514, no. 1–2, pp. 63–68, 2006.

[28] J. W. Elam, D. A. Baker, A. J. Hryn, A. B. F. Martinson, M. J. Pellin and J. T. Hupp, "Atomic layer deposition of tin oxide films using tetrakis(dimethylamino) tin," *Journal of Vacuum Science & Technology A: Vacuum, Surfaces, and Films*, vol. 26, no. 2, p. 244, 2008.

[29] J.-H. Jeun and S.-H. Hong, "CuO-loaded nano-porous SnO2 films fabricated by anodic oxidation and RIE process and their gas sensing properties," *Sensors Actuators B Chem.*, vol. 151, no. 1, pp. 1–7, 2010.

[30] M. Wang, Y. Liu, D. Zhang and H. Yang, "Anodization process of Sn in oxalic acid at low applied voltages," *Electrochim. Acta*, vol. 59, pp. 441–448, 2012.

[31] S. Ono, Y. Kobayashi, R. Kobayashi and H. Asoh, "Fabrication of Self-Organized Nanoporous Oxide Semiconductors by Anodization," *ECS Trans.*, vol. 16, no. 3, pp. 353–358, 2008.

[32] A. Palacios-Padrós, M. Altomare, A. Tighineanu, R. Kirchgeorg, N. K. Shrestha, I. Díez-Pérez, F. Caballero-Briones, F. Sanz and P. Schmuki, "Growth of ordered anodic SnO2 nanochannel layers and their use for H2 gas sensing," *J. Mater. Chem. A*, vol. 2, p. 915, 2014.

[33] S. Yeonmi and L. Seonghoon, "Self-organized regular arrays of anodic TiO2 nanotubes," *Nano Lett.*, vol. 8, no. 10, pp. 3171–3173, 2008.

[34] Z. Guo, T. Fu and H. Fu, "Crystal orientation measured by XRD and annotation of the butterfly diagram," *Mater. Charact.*, vol. 44, no. 4, pp. 431–434, 2000.

[35] H. Mark and M. Polanyi, "Die Gitterstruktur, Gleitrichtungen und Gleitebenen des weißen Zinns," *Zeitschrift für Phys.*, vol. 18, no. 1, pp. 75–96, 1923.

[36] O. Madelung, U. Rössler and S. M., *Landolt-Börnstein - Group III, Condensed Matter, Numerical Data and Functional Relationships in Science and Technology*, vol. 41C, 1998.

[37] A. F. Hollemann, E. Wiberg and N. Wiberg, *Lehrbuch der Anorganischen Chemie (in German)*, 1985.

[38] I. T. Lucas, J. Syzdek and R. Kostecki, "Interfacial processes at single-crystal β-Sn electrodes in organic carbonate electrolytes," *Electrochem. commun.*, vol. 13, pp. 1271–1275, 2011.

4 Application of Self-Organizing Arrays of SnO_2 Microplates with Enhanced Photocatalytic and Antimicrobial Properties in Comparison to Sponge-like SnO_x

This Chapter contains an adapted reproduction of a manuscript to be submitted.

4.1 Introduction

Many features of materials, in particular of transition metal oxides, become only of practical value when the material is micro- or nanostructured and therefore has a high surface area (e.g. for photoinduced water splitting,[1][2] as photocatalysts for organic degradation,[3][4] self-cleaning substrates[5][6] and solar cell electrodes.[7][8]) or short solid state diffusion paths (e.g. for electrochromic devices[9] or batteries[10]). Following the discovery of the new lamellar Sn/SnO_2 structure, a comparison of possible applications with the well-known sponge-like SnO_2 structure was inevitable. Tin dioxide (SnO_2) is a non-toxic wide-gap *n*-type semiconductor that combines high conductivity with high optical transparency in the visible range, making it an important component for optoelectronic applications[11] and as transparent conducting oxide for electrodes in solar cells,[12] gas-sensors,[13] catalysts[14] or coatings for architectural glass.[15] In addition, it has the potential to function as a high capacity anode material for lithium-ion batteries.[16] SnO_2 is often doped with fluorine[17] or antimony[18] to improve its electrical conductivity. It is also used to make indium tin oxide composites (ITO),[15] one of the important transparent conducting oxides that find application in touch-screen devices. For many applications (e.g. for dye sensitized solar cells[19]–[21]) SnO_2 is fabricated as a thin film, which can be accomplished by DC magnetron sputtering[22], chemical vapor deposition,[23] spray pyrolysis[24] or atomic layer deposition (ALD). [25] The

underlying principle of all the photocatalytic reactions is that UV light induces the formation of electron–hole pairs in the semiconducting oxide. The generated charge carriers are ejected to the surrounding electrolyte where they generate valence band holes (h+) as highly reactive redox species, which – after transfer to the aqueous electrolytes – have a sufficient energy to produce OH• radicals. These radicals can be used to trigger chain scission in attached hydrocarbon chains, and thus liberate terminal payloads.

Herein the chemical, physical and biological applications of the lamellar microstructure were investigated in detail and compared to sponge-like SnO_x. The capabilities to photodegrade Rhodamine B, amphiphilic behavior and antibacterial behavior were compared. SnO_2 lamellae exhibit higher photo-reactivity and are actively involved in the degradation of organic molecules upon exposure to UV light. In contrast to the SnO_x sponge, the lamellae also exhibit a switchable amphiphilic behavior. In combination with the photocatalytic and photobiocidal abilities of SnO_2, this could pave the way for the fabrication of self-cleaning surfaces.

4.2 Experimental

4.2.1 Materials

All starting materials were used without further purification. Commercially available tin foil with a thickness of 0.25 mm and a purity of 99.998 % was purchased from ABCR. The foil was cut into round plates with a diameter of 15 mm with a hole punch. Polishing solution consisted of n-butanol (99%, Acros Organics), methanol (p.A., Sigma-Aldrich), perchloric acid (Sigma-Aldrich) and MilliQ-water (18.3 ΩM/cm).[26] As part of the electrolyte, oxalic acid (p.A., Merck) and di-potassium oxalate (≥ 99 %, Acros) were used.

4.2.2 Synthesis

Prior to electropolishing, the foil was tempered with a heating rate of 5 °C/min and a dwell time of 1 h at 400 °C in a muffle furnace (Nabertherm S27). For electropolishing and anodization, the foil was mounted in a setup consisting of a PTFE-cylinder and a copper block as the anode. For the electropolishing, a solution consisting of 300 mL of methanol (≥ 99.8 %, Sigma-Aldrich), 200 mL of 1-butanol (99 % extra pure, Acros Organics), 29.16 mL of perchloric acid (70% solution in water, Acros Organics) and 4.71 mL of MilliQ-Water was used. A constant anodic bias of 40 V was applied via a Voltcraft PSP 1803 voltage source. A commercially available drilling machine (CMI) equipped with a custom made rotating steel electrode was used as the cathode. The foil was electropolished for 20 s without rotation, 15 s with maximum velocity and finally 7 s without rotation. After electropolishing, the solution was removed, the foil rinsed with MilliQ-Water and air-dried. For anodization, a buffer solution consisting of 0.05 wt% oxalic acid dihydrate (≥ 99.5 %, Sigma-Aldrich), 4.00 wt% di-potassium oxalate monohydrate (for analysis, Emsure ACS, Merck) and deionized water (Millipore) was used. Anodization was carried out under a constant anodic bias of 2 -

10 V applied by a Voltcraft Digi 35 voltage source for 10 min to 24 h. After anodization, the buffer solution was removed, the sample rinsed with deionized water and air-dried.

4.2.3 Characterization

Scanning electron microscopy (SEM)

Surface topography was analyzed using a high-vacuum mode scanning electron microscope (SEM; FEI Quanta 200 FEG Environmental-SEM, FEI Deutschland GmbH, Frankfurt / Main, Germany) at an acceleration voltage of 15 kV.

Cross section measurement

Samples were embedded in Poly(methyl methacrylate) (PMMA) using DuroFix-2 Kit by Struers GmbH. PMMA cylinder were then cut into disks of approx. 1 mm thickness with an EXAKT 300CP diamond band saw. Disks were glued on Plexiglas slides and polished by Struers RotoPol-31 for 30 seconds with polishing paper of a grain size of 1200 and 2 minutes with a grain size of 4000. Polished samples were then applied to an aluminum stub and measured in SEM using low vacuum mode.

Contact angle measurements

Contact angle (CA) goniometry was performed on a drop shaped analysis system (DSA 10-Mk2, Krüss GmbH, Germany), equipped with a thermostat chamber (TC3010/3410, Krüss GmbH, Germany), which in turn was connected to a Thermo Haake K 10/ThermoHaake DC 10 circulation system for temperature control inside the chamber. The reported water CAs were measured using the DropSnake plugin for ImageJ 1.46r.

Antibacterial assay

Freshly prepared *E. coli* (TOP 10 Invitrogen) culture was incubated at 37 °C over night under constant shaking. The anodized foil was placed in a petri dish and covered with 4 ml LB medium. 0.5 ml *E. coli* culture were added and the sample was incubated overnight at 37 °C. The foil was moved into a new petri dish containing 2 ml fresh LB medium to prevent drying out of the bacteria. Then, the samples were irradiated with UV light at 254 and 366 nm for 1 h. After irradiation, the foil was washed with 2 ml LB medium and placed on a LB agar plate without ampicillin for 15 min, with the anodized side of the foil facing the substrate. With the 2 ml LB medium used for washing of the foil, a wavy line was applied on the substrate using an inoculation loop. Then, the LB plates were incubated overnight at 37 °C.

Photocatalytic degradation of Rhodamine B

The ability to photodegrade a dye was measured by placing the sample in a vessel containing 5 ml of an aqueous Rhodamine B-solution (2 mmol/l). The sample was irradiated with UV light at 254 and 366 nm for 210 min. After 0, 5, 10, 15, 20, 25, 30, 40, 50, 60, 90, 120, 150, 180 and 210 min of irradiation, 1 ml aliquot of the solution was transferred into a cuvette. The UV-Vis spectrum of the solution was measured using a Varian Cary 5G UV-Vis-NIR Spectrophotometer in absorption mode. After the measurement, the aliquot was returned to the jar.

4.3 Results and Discussion

Anodization in a buffered solution consisting of oxalic acid and di-potassium oxalate at 2.0-2.2 volt for 24 hours results in a microstructured lamellar structure consisting of a tin dioxide shell and a metal core (Figure 4.1a,b). At higher voltages of 5 - 10 volts, anodization in a solution of solely oxalic acid leads to a nanoporous sponge-like surface consisting of tin dioxide with a thickness of up to 20 micrometer after anodization for 10 minutes (Figure 4.1c,d).

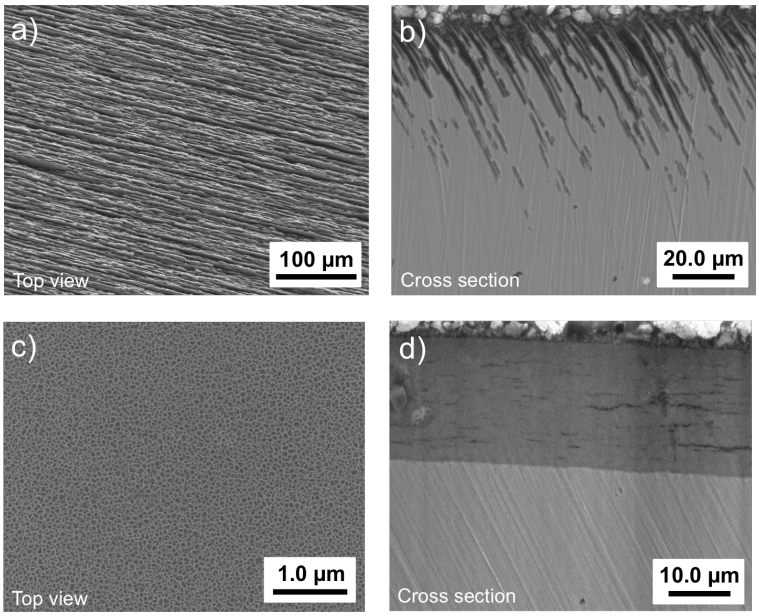

Figure 4.1 SEM images of anodized tin from the top (left) and in cross section view (right) of lamellar (a-b) and sponge-like (c-d) tin oxide.

4.3.1 Photocatalytic activity

An immediate application of the SnO_2 surface is the fabrication of self-cleaning surfaces. Semiconductors such as SnO_2 with photocatalytic activity[27] have attracted great interest due to their potential application in the degradation of organic pollutants, highly toxic and non-biodegradable dyes from the textile or printing industry being the most common examples.[28] The degradation of Rhodamine B or other dyes is a standard assay for testing the photocatalytic activity of free TiO_2,[29] ZnO[30] or SnO_2 nanoparticles[31][32] or SnO_2 nanocomposites.[33]

Upon irradiation with UV light, photocatalytically generated hydroxyl radicals ($OH^{\bullet -}$) and superoxide anions ($O_2^{\bullet -}$) are the reactive species at the surface of the anodized foils (and of many metal oxides).[34][35] The subsequent oxidation of the dye results in a discoloration of the aqueous Rhodamine B-solution. As shown inFigure 4.2, irradiation with UV light for 210 min yielded a degradation of 88.98 % of the dye. Sponge-like SnO_x only degraded 70.85 % of of the dye at the same conditions. Due to the oxidization of the surface from tempering, after electropolishing an oxidized rim remains. For this reason a polished reference sample shows a degradation of 10 %. Furthermore, Rhodamine B was irradiated without a sample. A degradation of less than 0.05 % was calculated showing that the dye is stable under UV irradiation.

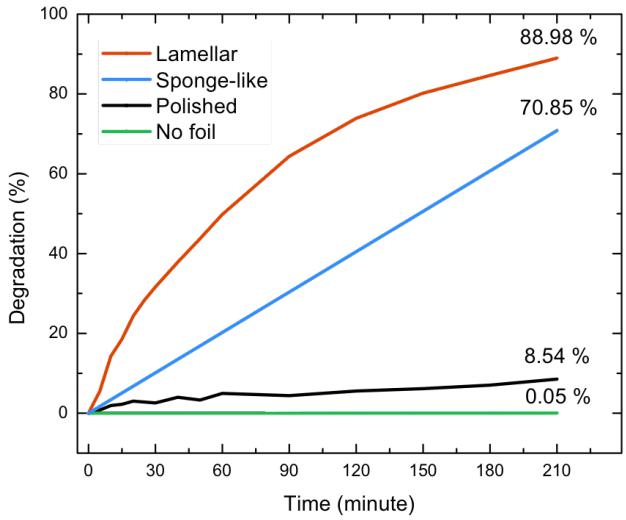

Figure 4.2 Degradation of Rhodamine B under UV irradiation on an anodized Sn surface

If a lamellar sample was kept in the dark while being in contact with Rhodamine B solution, no color change was observed, indicating that the degradation of the dye was caused by the photocatalytic effect of the anodized SnO_2 foil (see Figure 7.11 Appendix).

4.3.2 Wetting behavior

As rough solid surfaces often show superhydrophilicity and/or superhydrophobicity,[36] the wettability of the rough SnO_2 lamellae for water was examined. The microstructured SnO_2 surface exhibited a structure-dependent amphiphilic behavior upon exposure to UV light, as demonstrated by measuring the contact angle of the surface in the presence of water. Figure 4.3a shows that the surface of a sample with horizontally oriented lamellae is hydrophobic under dark conditions (contact angle 133°). After irradiation with UV light for 3 h, the contact angle decreased to 35°. When the surface was dried and kept in the dark for 24 hours, this behavior could be reversed, *i.e.* the surface became hydrophobic again. The same experiment applied to a sample with vertically oriented lamellae did not lead to a measurable contact angle, *i.e.* the surface texture did not support a stable solid-liquid-air interface, as the contact area between the SnO_2 lamellar array and the water droplet became too small.

Sponge-like SnO_x also does not exhibit switchable amphiphilic behavior (see Figure 4.3b). Irradiating with UV light or keeping the sample in the dark over night did not change the initially measured contact angle. Additionally, in the matter of minutes after placing the drop of water on the sample, it soaked the nanoporous structure.

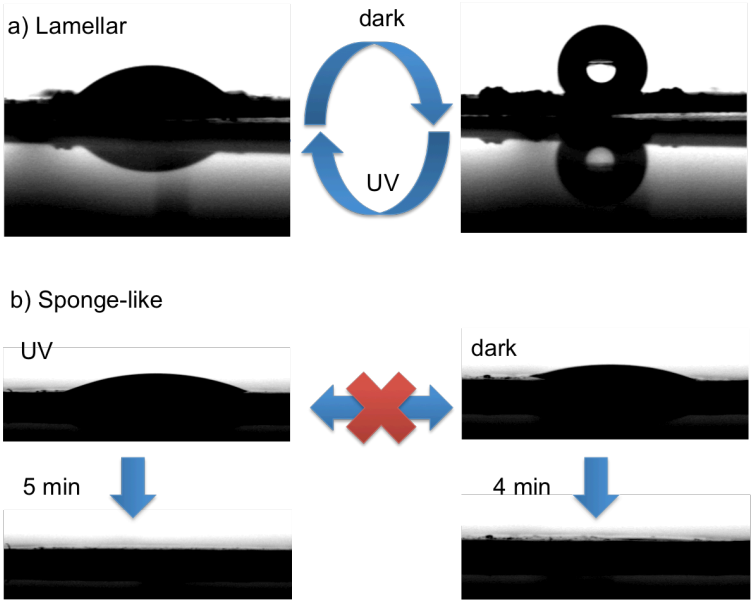

Figure 4.3 Hydrophilic and hydrophobic behavior of the anodized surface with horizontally orientated layers (a) and sponge-like tin oxide (b). Digital images of the contact angle of a water droplet after irradiation with UV light for 3 hours (left) and after keeping the sample in the dark for 24 hours (right).

4.3.3 Antibacterial behavior

The photocatalytic properties of active surfaces can be further explored for antimicrobial applications, giving them great technological interest. The photocatalytic properties of the anodized SnO_2 foils were exploited for antimicrobial applications based on formation of radical species upon illumination. The antimicrobial properties were assessed with cell cultures of *E. coli*, a common biological contaminant in wastewater and food. For this purpose *E. coli* cultures were incubated with anodized foils overnight at 37 °C under dark conditions. Subsequently, these surfaces were exposed to UV light at 254 and 366 nm for 1 h. The foils were washed with LB medium and the active surface was pressed against a LB agar culture plate. From the supernatant washing solution a wavy line was also applied to the agar plate. The plates where left to incubate at 37 °C overnight, and visually inspected after this time (Figure 4.4). The same procedure was done for a non-anodized foil (control). In Figure 4.4a it can be seen that almost no bacterial growth was observed on the area where the anodized lamellar foil (after UV light exposure) was in contact with the agar surface. Also from the supernatant washing solution inoculated on the agar plate, highly reduced bacterial growth was observed. Sponge-like SnO_x in contrast showed lower efficiency in antibacterial behavior as shown by the remnants of bacteria from the supernatant washing solution (Figure 4.4b). With a polished foil (Figure 4.4c), a high growth of bacteria was observed. This indicates that for the anodized foil after exposure to UV light very few bacteria survived, in contrast to the polished foil. The bacterial damage can be attributed to the formation of radical species by the photoactive SnO_2 surface.

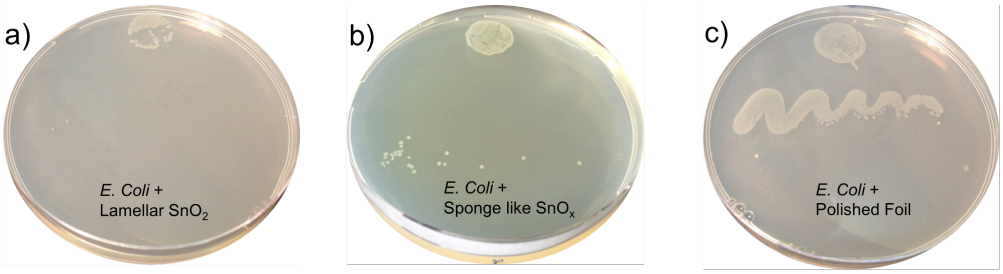

Figure 4.4 Representative digital images showing the influence of the catalytic activity of anodized tin foil on the growth of *E. coli* bacteria of lamellar SnO_2 (a), sponge-like SnO_x (b) and a polished foil (c). Experiment was performed by [redacted]

In general, toxicity is triggered by the induction of oxidative stress by free radical formation,[37][38] that is, radical oxide species (ROS) like superoxide or hydroxyl radicals. However, as the ROS species in this work were generated on SnO_2 surfaces by illumination with light, and considering furthermore that no severe toxicity effects have been reported for SnO_2 nanopartices,[39] and that SnO_2 is highly insoluble in aqueous media,[40][41] we assume that the anti-microbial properties are due to radical metabolites formed by photooxidation (a specific reaction) rather than to SnO_2 toxicity (which may be related to a variety of chemical processes).

The reactivity of solid surfaces is associated with desired (catalytic) or unwanted (toxic) effects. The solubility or degradation of solids are important contributors to their reactivity in a biological environment.[39][42] The highly polymeric oxides of the group 4 elements (Si, Ge, Sn) and the early transition metals (e.g. Ti, Zr, Ta) are highly insoluble (and therefore highly inert),[43] whereas oxides of the later 3d transition metals (e.g. Mn, Fe, Co, or Zn) metals are instable under acidic/basic conditions or in the presence of coordinating ligands.[44] As SnO_2 forms a dense layer of aligned lamellae, its uptake by cells is very unlikely. These assumptions are in harmony with the results of a study indicating that SnO_2 nanoparticles have no toxic

effects on guppy.[39] SnO_2 nanoparticles may penetrate into the fish blood through the gills and intestine, finding their way to various organs, but - because of their insolubility - they have no toxic effects. Similar results were obtained in earlier experiments on rainbow trout exposed to titanium dioxide nanoparticles,[45][46] whereas copper-containing nanoparticles were toxic for *D. rerio*,[47] and silver and zinc oxide nanoparticles penetrating into the gonads and eggs of *D. rerio* caused disturbances in embryonic development.[48][49]

4.4 Conclusions

In summary, it was demonstrated that a macroscopically homogeneous, lamellar SnO_2 structure fabricated by anodization of tin in a buffer solution of oxalic acid and di-potassium oxalate exhibits a distinctively higher photoactivity upon exposure to UV light than sponge-like SnO_x. Due to their intrinsic photocatalytic activity paired with high surface area, the anodized lamellar SnO_2 surfaces can degrade organic contaminants like Rhodamine B and in addition act as efficient photobiocides towards bacterial pathogens like *E. coli*. Related phenomena were observed recently for bio-inspired SnO_2 coatings on glass.[50] In addition, it could be demonstrated that the anodized lamellar tin surfaces present amphiphilic properties by switching from a hydrophobic to a hydrophilic behavior upon sunlight exposure. The sponge-like SnO_x structure does not express this comportment. As a conclusion it can be said that the lamellar SnO_2 structure shows increased performance in every aspect investigated compared to sponge-like SnO_x. This discovery could lead to the development of new protective, antibacterial and antifouling coatings[50] by a simple anodization of tin.

4.5 References

[1] A. Fujishima and K. Honda, "Electrochemical photolysis of water at a semiconductor electrode," *Nature*, vol. 238, no. 5358, pp. 37–38, 1972.

[2] J. H. Park, S. Kim and A. J. Bard, "Novel carbon-doped TiO2 nanotube arrays with high aspect ratios for efficient solar water splitting," *Nano Lett.*, vol. 6, no. 1, pp. 24–28, 2006.

[3] M. R. Hoffmann, M. R. Hoffmann, S. T. Martin, S. T. Martin, W. Choi, W. Choi, D. W. Bahnemann, and D. W. Bahnemannt, "Environmental Applications of Semiconductor Photocatalysis," *Chem. Rev.*, vol. 95, no. 1, pp. 69–96, 1995.

[4] A. Fujishima, X. Zhang and D. A. Tryk, "TiO2 photocatalysis and related surface phenomena," *Surface Science Reports*, vol. 63, no. 12, pp. 515–582, 2008.

[5] A. Fujishima and D. Kagaku, "Self-cleaning effect using TiO2 photocatalyst," *Electrochemistry*, vol. 64, pp. 1052–1055, 1996.

[6] I. P. Parkin and R. G. Palgrave, "Self-cleaning coatings," *J. Mater. Chem.*, vol. 15, pp. 1689-1695, 2005.

[7] B. O'Regan and M. Grätzel, "A low-cost, high-efficiency solar cell based on dye-sensitized colloidal TiO2 films," *Nature*, vol. 353, no. 6346, pp. 737–740, 1991.

[8] J. N. Tiwari, R. N. Tiwari and K. S. Kim, "Zero-dimensional, one-dimensional, two-dimensional and three-dimensional nanostructured materials for advanced electrochemical energy devices," *Progress in Materials Science*, vol. 57, no. 4, pp. 724–803, 2012.

[9] C. Santato, M. Odziemkowski, M. Ulmann and J. Augustynski, "Crystallographically oriented mesoporous WO3 films: Synthesis, characterization, and applications," *J. Am. Chem. Soc.*, vol. 123, no. 43, pp. 10639–10649, 2001.

[10] A. S. Aricò, P. Bruce, B. Scrosati, J.-M. Tarascon and W. van Schalkwijk, "Nanostructured materials for advanced energy conversion and storage devices," *Nat. Mater.*, vol. 4, no. 5, pp. 366–377, 2005.

[11] T. T. Emons, J. Li and L. F. Nazar, "Synthesis and characterization of mesoporous indium tin oxide possessing an electronically conductive framework," *J. Am. Chem. Soc.*, vol. 124, no. 29, pp. 8516–8517, 2002.

[12] F. Yang and S. R. Forrest, "Organic Solar Cells Using Transparent SnO2-F Anodes," *Adv. Mater.*, vol. 18, no. 15, pp. 2018–2022, 2006.

[13] E. R. Leite, I. T. Weber, E. Longo and J. A. Varela, "A New Method to Control Particle Size and Particle Size Distribution of SnO2 Nanoparticles for Gas Sensor Applications," *Adv. Mater. Commun.*, no. 13, pp. 965–968, 2000.

[14] I. T. Weber, A. Valentini, L. F. D. Probst, E. Longo and E. R. Leite, "Catalytic activity of nanometric pure and rare earth-doped SnO2 samples," *Mater. Lett.*, vol. 62, no. 10–11, pp. 1677–1680, 2008.

[15] M. Vergöhl, N. Malkomes, T. Matthée, G. Bräuer, U. Richter, F. W. Nickol and J. Bruch, "In situ monitoring of optical coatings on architectural glass and comparison of the accuracy of the layer thickness attainable with ellipsometry and photometry," *Thin Solid Films*, 2001, vol. 392, no. 2, pp. 258–264.

[16] Y. Wang, I. Djerdj, B. Smarsly and M. Antonietti, "Antimony-doped SnO2 nanopowders with high crystallinity for lithium-ion battery electrode," *Chem. Mater.*, vol. 21, no. 14, pp. 3202–3209, 2009.

[17] M. Adnane, H. Cachet, G. Folcher and S. Hamzaoui, "Beneficial effects of hydrogen peroxide on growth, structural and electrical properties of sprayed fluorine-doped SnO2 films," *Thin Solid Films*, vol. 492, no. 1–2, pp. 240–247, 2005.

[18] H. Viirola and L. Niinistö, "Controlled growth of antimony-doped tin dioxide thin films by atomic layer epitaxy," *Thin Solid Films*, vol. 251, no. 2, pp. 127–135, 1994.

[19] H. J. Snaith and C. Ducati, "SnO2-Based dye-sensitized hybrid solar cells exhibiting near unity absorbed photon-to-electron conversion efficiency," *Nano Lett.*, vol. 10, no. 4, pp. 1259–1265, 2010.

[20] A. Birkel, Y.-G. Lee, D. Koll, X. Van Meerbeek, S. Frank, M. J. Choi, Y. S. Kang, K. Char and W. Tremel, "Highly efficient and stable dye-sensitized solar cells based on SnO2 nanocrystals prepared by microwave-assisted synthesis," *Energy & Environmental Science*, vol. 5, no. 1, p. 5392, 2012.

[21] C. Jin, T. Yamazaki, K. Ito, T. Kikuta and N. Nakatani, "H2S sensing property of porous SnO2 sputtered films coated with various doping films," *Vacuum*, vol. 80, no. 7 SPEC. ISS., pp. 723–725, 2006.

[22] R. Kohler, H. Besser, M. Hagen, J. Ye, C. Ziebert, S. Ulrich, J. Proell and W. Pfleging, "Laser micro-structuring of magnetron-sputtered SnOx thin films as anode material for lithium ion batteries," *Microsyst. Technol.*, vol. 17, no. 2, pp. 225–232, 2011.

[23] J. Sundqvist, J. Lu, M. Ottosson and A. Hårsta, "Growth of SnO2 thin films by atomic layer deposition and chemical vapour deposition: A comparative study," *Thin Solid Films*, vol. 514, no. 1–2, pp. 63–68, 2006.

[24] J. Pena, J. Perez-Pariente and M. Vallet-Regi, "Textural properties of nanocrystalline tin oxide obtained by spray pyrolysis," *Journal of Materials Chemistry*, vol. 13, no. 9, p. 2290, 2003.

[25] J. W. Elam, D. A. Baker, A. J. Hryn, A. B. F. Martinson, M. J. Pellin and J. T. Hupp, "Atomic layer deposition of tin oxide films using tetrakis(dimethylamino) tin," *Journal of Vacuum Science & Technology A: Vacuum, Surfaces, and Films*, vol. 26, no. 2, p. 244, 2008.

[26] S. Yeonmi and L. Seonghoon, "Self-organized regular arrays of anodic TiO2 nanotubes," *Nano Lett.*, vol. 8, no. 10, pp. 3171–3173, 2008.

[27] R. André, M. N. Tahir, H. C. C. Schröder, W. E. G. Müller and W. Tremel, "Enzymatic synthesis and surface deposition of tin dioxide using silicatein-α," *Chem. Mater.*, vol. 23, no. 24, pp. 5358–5365, 2011.

[28] I. K. Konstantinou and T. A. Albanis, "TiO2-assisted photocatalytic degradation of azo dyes in aqueous solution: Kinetic and mechanistic investigations: A review," *Appl. Catal. B Environ.*, vol. 49, no. 1, pp. 1–14, 2004.

[29] A. L. Linsebigler, A. L. Linsebigler, J. T. Yates Jr, G. Lu, G. Lu and J. T. Yates, "Photocatalysis on TiO2 Surfaces: Principles, Mechanisms, and Selected Results," *Chem. Rev.*, vol. 95, no. 3, pp. 735–758, 1995.

[30] M. N. Tahir, F. Natalio, M. A. Cambaz, M. Panthofer, R. Branscheid, U. Kolb and W. Tremel, "Controlled synthesis of linear and branched Au@ZnO hybrid nanocrystals and their photocatalytic properties," *Nanoscale*, vol. 5, no. 20, pp. 9944–9949, 2013.

[31] B. Esen, T. Yumak, A. Sinağ and T. Yildiz, "Investigation of photocatalytic effect of SnO2 nanoparticles synthesized by hydrothermal method on the decolorization of two organic dyes," *Photochem. Photobiol.*, vol. 87, no. 2, pp. 267–274, 2011.

[32] S. Dai and Z. Yao, "Synthesis of flower-like SnO2 single crystals and its enhanced photocatalytic activity," *Applied Surface Science*, vol. 258, no. 15, pp. 5703–5706, 2012.

[33] C. Wang, B.-Q. Xu, X. Wang and J. Zhao, "Preparation and photocatalytic activity of ZnO/TiO2/SnO2 mixture," *Journal of Solid State Chemistry*, vol. 178, no. 11, pp. 3500–3506, 2005.

[34] J. Herrmann, "Heterogeneous photocatalysis: fundamentals and applications to the removal of various types of aqueous pollutants," *Catalysis Today*, vol. 53, no. 1. pp. 115–129, 1999.

[35] M. Lu, P. Pichat, *Photocatalysis and Water Purification: From Fundamentals to Recent Applications*, Weinheim: Wiley-VCH, 2013.

[36] X. Deng, L. Mammen, H.-J. Butt and D. Vollmer, "Candle Soot as a Template for a Transparent Robust Superamphiphobic Coating," *Science*, vol. 335, no. 2012, pp. 67–70, 2012.

[37] R. F. Schmidt, F. Lang and M. Heckmann, *Die Physiologie des Menschen*, 31st ed. Berlin, Heidelberg: Springer, 2010.

[38] H. Rehm and F. Hammar, *Biochemie light*, Frankfurt: Verlag Harri Deutsch, 2011.

[39] E. Y. Krysanova, T. B. Demidova, L. A. Pel'gunova, S. M. Badalyan, M. N. Rumyantseva and A. M. Gas'kov, "Effect of hydrated tin dioxide (SnO2 x xH2O) nanoparticles on guppy (Poecilia reticulata Peters, 1860)," *Dokl. Biol. Sci.*, vol. 426, pp. 288–289, 2009.

[40] D. Rai, M. Yui, H. T. Schaef and A. Kitamura, "Thermodynamic model for SnO2(cr) and SnO2(am) solubility in the aqueous Na+-H+-OH--Cl--H2O system," *J. Solution Chem.*, vol. 40, no. 7, pp. 1155–1172, 2011.

[41] G. Janderg and E. Blasius, *Lehrbuch der präparativen anorganischen Chemie*, Stuttgart: S. Hirzel Verlag, 1970.

[42] W. J. Stark, "Nanopartikel in biologischen Systemen," *Angew. Chemie*, vol. 123, no. 6, pp. 1276–1293, 2011.

[43] M. J. Harnpden-Smith, T. A. Wark and C. J. Brinke, "The solid state and solution structures of tin (IV) alkoxide compounds and their use as ecursors to form tin oxi ceramics via sol-gel-type hydrolysis and condensation," *Coord. Chem. Rev.*, vol. 112, pp. 81–116, 1992.

[44] W. Kaim, B. Schwederski and A. Klein, *Bioinorganic Chemistry - Inorganic Elements in the Chemistry of Life*, Weinheim: Wiley-VCH, 2013.

[45] G. Federici, B. J. Shaw and R. D. Handy, "Toxicity of titanium dioxide nanoparticles to rainbow trout (Oncorhynchus mykiss): Gill injury, oxidative stress, and other physiological effects," *Aquat. Toxicol.*, vol. 84, no. 4, pp. 415–430, 2007.

[46] D. B. Warheit, R. A. Hoke, C. Finlay, E. M. Donner, K. L. Reed and C. M. Sayes, "Development of a base set of toxicity tests using ultrafine TiO2 particles as a component of nanoparticle risk management," *Toxicol. Lett.*, vol. 171, no. 3, pp. 99–110, 2007.

[47] R. J. Griffitt, R. Weil, K. A. Hyndman, N. D. Denslow, K. Powers, D. Taylor and D. S. Barber, "Exposure to copper nanoparticles causes gill injury and acute lethality in zebrafish (Danio rerio)," *Environ. Sci. Technol.*, vol. 41, no. 23, pp. 8178–8186, 2007.

[48] K. J. Lee, P. D. Nallathamby, L. M. Browning, C. J. Osgood and X. H. Nancy Xu, "In vivo imaging of transport and biocompatibility of single silver nanoparticles in early development of zebrafish embryos," *ACS Nano*, vol. 1, no. 2, pp. 133–143, 2007.

[49] X. Zhu, L. Zhu, Z. Duan, R. Qi, Y. Li and Y. Lang, "Comparative toxicity of several metal oxide nanoparticle aqueous suspensions to Zebrafish (Danio rerio) early developmental stage," *J. Environ. Sci. Health. A. Tox. Hazard. Subst. Environ. Eng.*, vol. 43, no. 3, pp. 278–284, 2008.

[50] R. André, F. Natalio, M. N. Tahir, R. Berger and W. Tremel, "Self-cleaning antimicrobial surfaces by bio-enabled growth of SnO2 coatings on glass," *Nanoscale*, vol. 5, pp. 3447–56, 2013.

5 Synthesis and Characterization of Carbon Coated Sponge-like Tin Oxide Films and Their Application as Electrode Materials in Lithium Ion Batteries

This Chapter contains an adapted reproduction of a manuscript to be submitted. Results originate partly from cooperation with [redacted] in Prof. Zentel's group who performed the synthesis of the polymer, carbon coating and the electrochemical characterization.

5.1 Introduction

The interest in the synthesis of carbon coated nanostructured materials with a high surface area has increased within the last years, as such kind of materials can be applied in various fields such as in catalysts,[1][2] and as electrode materials in energy storage devices, especially in lithium-ion batteries.[3]–[5] Currently, lithium-ion batteries are the leading energy storage devices in portable electronic devices and are furthermore attractive candidates for up-scale applications such as electric vehicles. However, the state-of-the-art batteries contain electrode materials with rather limited specific capacities, whereby on the anode side graphite is applied with a theoretical capacity of 372 mAh g^{-1}. Therefore, the exploration of new electrode materials with higher specific capacities is indispensable, for instance to increase the driving range of electric vehicles.

As alternative electrode materials, *inter alia* tin and tin oxides (SnO or SnO_2) are interesting, due to their theoretical specific capacity of around 790 mAh g^{-1}.[6][7] As conversion-alloying compounds tin oxides first undergo a conversion reaction forming elemental tin and Li_2O. This conversion is followed by alloying reaction of elemental tin and lithium described as follows.[8][9]

$$SnO_2 + 4Li^+ + 4e^- \rightarrow Sn + 2Li_2O \qquad (1)$$

$$Sn + x\,Li + x\,e^- \leftrightarrow Li_xSn\ (0 \leq x \leq 4.4) \qquad (2)$$

These oxides suffer from the irreversible formation of Li_2O and from the volume changes during the (de-)alloying progress. Both issues cause a capacity fading during electrochemical cycling.[10]–[12] Thus, especially in case of tin oxides the architecture of active material morphology has a high impact on the battery performance. Current approaches to address these issues range from the use of zero-dimensional nanoparticles to three-dimensional nano-sized morphologies with hollow structures,[6][13]–[15] for instance hollow tin dioxide microspheres,[16] whereby the motivation to create hollow structures is driven by the idea that the void space buffers the volume changes.[13] Furthermore, nanoporous tin oxides have been investigated recently, but suffered from very short cycling lifetime.[17]–[19] In addition to the downsizing of active material to nano-size, the application of a carbon coating on the surface of nano-sized active material lowers the intrinsically high electrical resistance within the electrode composite and improves the battery performance, as it has been applied to numerous active materials including also tin oxides.[20][21]

Herein, the synthesis of a carbon coated nanoporous sponge-like morphology of SnO_x was investigated. The sponge-like morphology of SnO_x is derived by first electrodepositing Sn immediately onto Cu-foil, which serves as the current collector, followed by the anodization of the Sn film in an aqueous medium resulting in the nanoporous sponge-like morphology. Thus, for this approach there is no need for the addition of electrochemically inactive binding material and no need of slurry preparation using toxic organic solvents such as *N*-methyl pyrrolidone (NMP), which is a common procedure in many of the reports in this area of research.[22] The motivation for the use of this sponge-like morphology is the nanoporous structure, which might buffer the volume changes during (de-)lithiation, and porous structure

enables short diffusion pathways for the lithium-ions due to the nano-sized dimensions. Furthermore, these films are functionalized with block copolymers containing an anchor block and a graphitizable block to obtained homogenous carbon film.[5][21][23] As a carbon source polyacrylonitrile is used and a rather low pyrolysis temperature (350 °C) is applied. At this temperature a flexible carbonaceous material (also described as cyclized polyacrylonitrile) is obtained, a strategy similarly reported to buffer volume changes of silicon, a further alloying based electrode material for lithium-ion batteries.[24] A detailed structural and morphological characterization of the as-synthesized material as well as the carbon coated material is described in this manuscript. Furthermore, the synthesized materials are applied as an electrode material in lithium-ion batteries and the influence of the carbon coating is investigated by comparing as-anodized and carbon coated material. Ex-situ scanning electron microscopy was applied after electrochemical cycling of the SnO_x material to investigate the morphology and structural changes after electrochemical cycling.

5.2 Experimental

5.2.1 Synthesis of SnO_x Sponges on Copper Foil

Copper foil (Schlenk) was cut into round pieces of 15 mm in diameter. The passivation layer on the surface was then removed by applying 1 ml of a solution consisting of 300 mL of methanol (≥ 99.8 %, Sigma-Aldrich), 200 mL of 1-butanol (99 % extra pure, Acros Organics), 29.16 mL of perchloric acid (70% solution in water, Acros Organics) and 4.71 mL of MilliQ-Water were used. After 30 s the samples were cleaned with MilliQ-Water and air-dried. For electrodeposition and anodization, the foil was mounted in a custom made setup (see Chapter 2.2.3). Instead of the PTFE-cylinder used in the anodization of tin, a custom made version with a conical shape was used. For electrodeposition, a solution consisting of 0.22 mol / l tin (II) chloride dihydrate (≥ 99.99 %, Sigma-Aldrich) and tri-ammonium citrate (≥ 97 %, Alfa Aesar) and deionized water was used. Electrodeposition was carried out at a constant current of 4 mA applied via an Agilent E3646A voltage source for 25 min. After electrodeposition, the solution was removed, the foil rinsed with MilliQ-Water and air-dried. For the anodization, a solution consisting of 5.9 wt% oxalic acid dihydrate (≥ 99.5 %, Sigma-Aldrich) and deionized water (Millipore) was used. Anodization was carried out under a constant anodic bias of 10 V applied by a Voltcraft PSP 1803 voltage source for 6 min. After anodization, the solution was removed, the sample rinsed with deionized water and air-dried.

5.2.2 Carbon Coating of SnO_x Sponges

The carbon precursor block copolymer was synthesized according to a previous synthesis strategy.[5] Briefly, acrylonitrile (AN) was polymerized by RAFT polymerization technique using 2-dodecylsulfanylthiocarbonylsulfanyl-2-methyl propionic acid (DMP) as a chain transfer agent and α,α-azoisobutyronitrile (AIBN) as

initiator. The ratio of AN:CTA:AIBN was set to be 250:1:0.1. For the block copolymerization, PAN was chosen as a macro-CTA and *N*-acryloxysuccinimide (NAS) [25] as the monomer and 2,2_-azobis(4-methoxy-2,4-dimethylvaleronitrile) (AMDV) as the initiator. The molar ratio was NAS:PAN:AMDV = 25:1:0.2 and the reaction was conducted in DMSO for 48 h at 30 °C. Finally, the reactive ester was aminolyzed by the use of dopamine hydrochloride in DMSO resulting in P(AN-b-DAAM).

^{1}H-NMR (400 MHz, DMSO-*d6*) δ [ppm] = 6.20–6.70 (d, Ar-H), 3.42 (s, CONH–CH_2), 3.14 (s, C*H* of polymer backbone), 2.03 (s, CH_2 of polymer backbone and CONH-CH-CH_2).

FT-IR: 2940 (C-H valence band), 2443 (nitrile valence band), 1702 (NH amide band), 1520 (NH deformation band), 1444, 1384, 1282, 1251 cm^{-1}.

The copper foil with the deposited SnO_x sponges was placed in 1 ml of a 20 mg ml^{-1} solution of P(AN-b-DAAM) in DMSO. The foil was removed after 8 h from the solution and washed with DMF to remove unbound polymer. The sample was dried under vacuum and then pyrolyzed. The heat treatment was conducted in two steps by first heating to 300 °C for 240 min and then heating to 350 °C for 45 min.

5.2.3 Characterization

X-ray photoelectron spectroscopy (XPS)

XPS spectra were measured on a PHI 5600 Multi-Technique XPS (Physical Electronics, Lake Drive East, Chanhassen, MN) using monochromatized Al Kα at 1486.6 eV. Prior to measurement, the surface was sputtered for 1 s with Ar^+ ions to remove adsorbed CO_2. Atomic concentrations were calculated using MULTIPAK 9.4.1.2 software.

X-ray diffraction (XRD)

The crystal structure of was examined via room temperature X-ray diffraction on a Bruker D8 Discover instrument operated in reflection geometry with a CuK$\alpha_{1,2}$ X-ray source.

Scanning electron microscopy (SEM)

Surface topography was analyzed using a high-vacuum mode scanning electron microscope (SEM; FEI Quanta 200 FEG Environmental-SEM, FEI Deutschland GmbH, Frankfurt / Main, Germany) at an acceleration voltage of 15 kV.

Cross section measurement

Samples were embedded in Poly(methyl methacrylate) (PMMA) using DuroFix-2 Kit by Struers GmbH. PMMA cylinder were then cut into disks of approx. 1 mm thickness with an EXAKT 300CP diamond band saw. Disks were glued on Plexiglas slides and polished by Struers RotoPol-31 for 30 seconds with polishing paper of a grain size of 1200 and 2 minutes with a grain size of 4000. Polished samples were then applied to an aluminum stub and measured in SEM using low vacuum mode.

Characterization of the polymer

NMR (nuclear magnetic resonance) spectroscopy was conducted using a Bruker ARX 400, and FTIR spectroscopy (Fourier transform infrared) was carried out using Jasco FT/IR 4100 with an ATR unit. Size exclusion chromatography (SEC) was performed with hexafluoroisopropanol as solvent. The detector system contained refractive index (Agilent) and UV-vis (Agilent) units. The calibration was done using polymethylmethacrylate standards, purchased from Polymer Standard Services.

Electrochemical Characterization of SnO_x Sponge

The content of SnO_x was in average 2.89 mg. Swagelok™ cells were assembled in a glove box (MBraun) with water and oxygen content of less than 0.1 ppm. Polypropylene fleeces (FS2190 Freudenberg, Germany) were used as separator and were drenched with an ethylene carbonate: diethyl carbonate 3:7 electrolyte containing 1M $LiPF_6$. As a counter and reference electrode lithium foil (Rockwood Lithium) was used, so that all given potentials refer to the Li/Li^+ redox couple. The electrochemical experiments were conducted at 20 °C ± 2 °C. A Maccor Battery Tester was used for galvanostatic cycling experiments. Cyclic voltammetry was performed using a VMP3 potentiostat (BioLogic), applying a sweep rate of 0.05 mV/s in the range of 0.01 V and 3.0 V.

5.3 Results and Discussion

5.3.1 Structural and morphological characterization of carbon coated SnO_x sponges

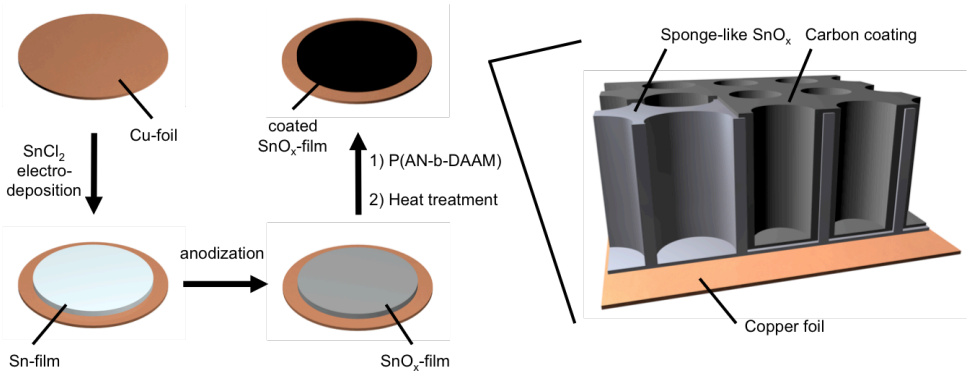

Figure 5.1 Scheme showing the different steps of sample preparation (left) and magnification of the schematic sample structure (right).

A tin film was electrodeposited from a tin(II) chloride and tri-ammonium citrate containing solution[26] onto copper foil, which can be used as the current collector in the lithium-ion battery setup (see Figure 5.1). SEM image of the deposited film is shown in Figure 5.2a. The surface exhibits a pre-structuring resulting from intertwined single crystals grown during the deposition. By applying a common anodization technique described in Chapter 2.4.1,[27] a sponge-like SnO_x film can be formed as shown by the SEM image in Figure 5.2b. As already mentioned in Chapter 1.3 the anodization of tin generates large amounts of oxygen. The formed oxygen is the reason for pore breaking and inhibits regular pore growth, thus resulting in the well-known sponge-like structure as reported before.[25][26] Images at higher magnifications prove the sponge-like morphology with pore diameters of 30-60 nm and wall thicknesses of 10-15 nm as shown in Figure 5.2c.

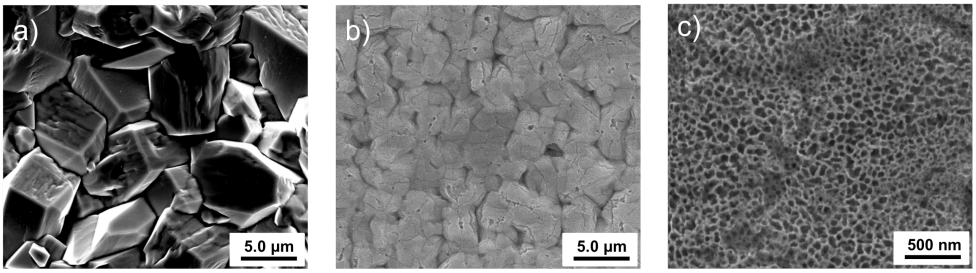

Figure 5.2 SEM images of tin surface after deposition and anodization. a) Deposited metallic tin with different oriented single crystalline tin domains, b) anodized SnO_x surface, c) high resolution image of sponge-like SnOx surface.

Cross section measurement of the anodized sample reveals a nanoporous SnO_x film thickness of 20 - 25 µm (Figure 5.3). Longer anodization times than the herein applied time of 6 min result in spallation of the oxide layer, because once the reaction reaches the bottom of the tin layer, oxygen evolution results in detachment of the SnO_x from the copper foil. Thus, anodization was interrupted shortly before the copper surface was reached. A thin layer of non-oxidized tin remained, gluing the porous tin oxide to the copper foil.

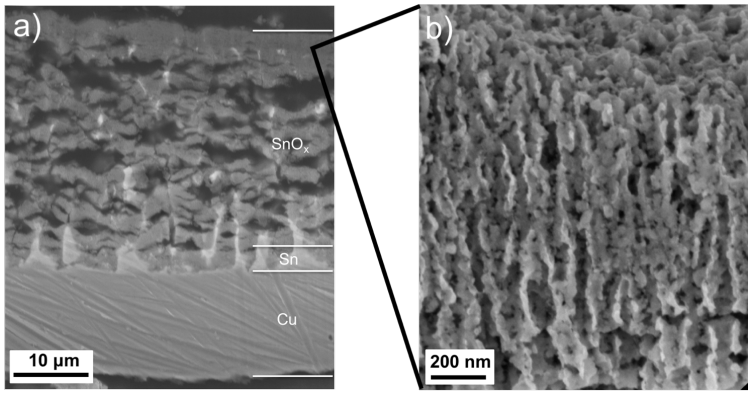

Figure 5.3 a) Cross section SEM image of anodized sample. Top: Sponge-like nanoporous SnO_x (grey), cracks from oxygen evolution breaking up regular tubular structure (black). Middle: Thin tin gluing layer connecting nanoporous tin oxide to underlying copper foil. Bottom: Copper foil. b) High resolution cross section SEM image of the SnO_x layer showing the nanoporosity.

The crystallinity of the film was investigated by X-ray diffraction (XRD) as shown in Figure 5.4. As commonly observed for SnO_x, broad reflections appear, which can be attributed to SnO_2.[27][28] Sharp reflections of low intensity originate from metallic Sn of the gluing layer. Remaining high intensity reflections can be attributed to the underlying copper foil. Reflections from SnO could not be detected due to the highly amorphous nature of the film.[31]

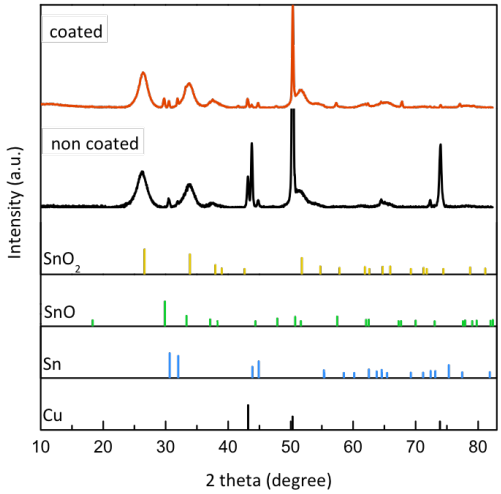

Figure 5.4 XRD patterns before (black) and after coating and tempering (red), reference patterns of SnO_2 (JCPDS 00-041-1445), SnO (JCPDS 01-085-0423), Sn (JCPDS 01-065-0296) and Cu. (JCPDS 01-070-3038)

A recently developed carbon coating approach based on the use of a block copolymer containing was applied to the sponge-like SnO_x thin film.[5][19] The block copolymer contains a carbon precursor block, in this case polyacrylonitrile (PAN), and a block, that can coordinate onto a metal oxide surface. As a coordinating species, dopamine was chosen and incorporated into the polymer, as dopamine containing polymers were reported to bind onto SnO_2 nanoparticle surfaces.[32] The reversible addition-fragmentation chain transfer (RAFT) polymerization based synthesis route is described in Figure 5.5a.

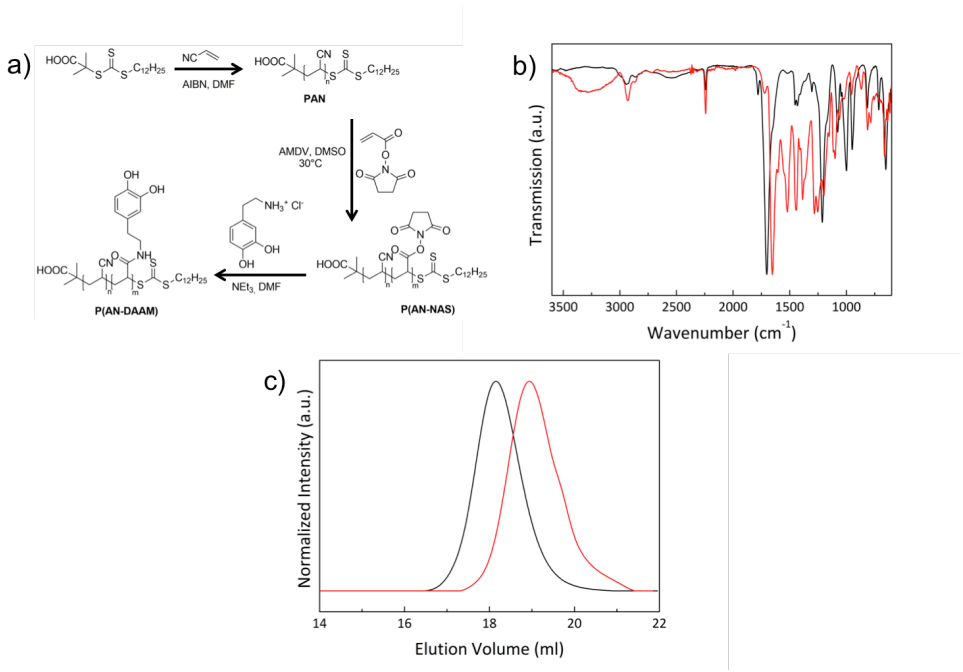

Figure 5.5 a) Reaction scheme for the synthesis of P(AN-b-DAAM). b) IR spectra of P(AN-b-NAS) (black) and P(AN-b-DAAM) (red). c) SEC of P(AN) (red) and P(AN-b-DAAM) (black). Measurement and data treatment were performed by [redacted]

Briefly, first the polyacrylonitrile block is synthesized with an averaged number of repeating unit of ~70 as confirmed by NMR spectroscopy (see Figure 7.12 Appendix). Dopamine is attached to the polymer after the block copolymerization with a reactive ester monomer (average dopamine containing repeating unit of 23(see NMR spectra in Figure 7.13 Appendix) by the aminolysis of the reactive ester to finally obtain poly(acrylonitrile-dopamine acrylamide) (P(AN-DAAM)). The successful synthesis of the polymer can be proven by IR spectroscopy, which proves the attachment of dopamine due to the presence of the amide band (1702 cm^{-1}) and the disappearance of the reactive ester band (1654 cm^{-1}) (see Figure 5.5b), size exclusion chromatography (SEC) showing a shift to lower elution volumes after the block copolymerization (Figure 5.5c), and NMR spectroscopy (see Figure 7.14 Appendix).

The polymer was bound onto the sponge-like inorganic structure by dipping the inorganic material into a polymer solution in DMF for 6 h. Unbound polymer was removed by repeated washing with DMF. The polymer coating is transformed into cyclized polyacrylonitrile by pyrolysis at 350 °C. Cross section SEM of embedded samples showed the structure to be unchanged after coating and heat treatment (see Figure 5.6).

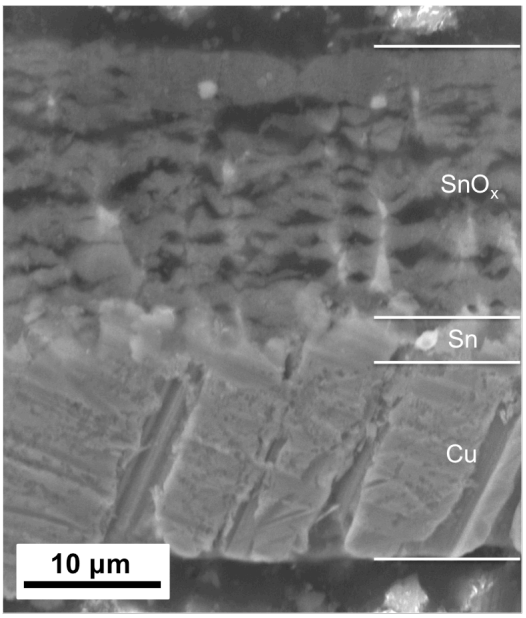

Figure 5.6 Cross section SEM image of coated sample. Top: Sponge-like nanoporous SnO_x (grey), cracks from oxygen evolution breaking up regular tubular structure (black). Middle: Tin gluing layer connecting nanoporous tin oxide to underlying copper foil. Bottom: Copper foil.

In XRD measurement, new reflections appear (Figure 5.4) after the coating, which can be attributed to tin(II) oxide appear, as the heat treatment increases the crystallinity of SnO.

Energy dispersive X-ray (EDX) spectroscopy was used to further investigate the composition of the sponge-like SnO_x (Figure 5.7). In contrast to the constant Sn:O

ratio observed for the as anodized sample (Figure 5.7a), which was determined to be around 1:1 throughout the whole sample (see Table 7.3 and Figure 7.15 Appendix), the Sn:O ratio of the heat treated and carbon coated sample is 1:1 in volume fraction close to the Cu foil (see Figure 5.7b), but increases starting from the middle of the sponge in direction of the surface (see Table 7.4 and Figure 7.16 Appendix). In contrast to previous reports observing an increase in oxidation state upon heat treatment of the sponge,[31][32] the combination of polymer coating and heat treatment in oxygen free atmosphere seem to create a reducing atmosphere. The gradient in oxygen concentration further supports the assumption of a reduction of tin(IV) oxide during the heat treatment in the presence of carbonaceous material as the effect occurs predominantly on the surface of the sample where most of the polymer is expected to coordinate. A constant concentration of carbon between 2.1 - 3.6 % throughout the sample cross section was measured for the coated sample (see Figure 5.7b), confirming the homogeneous coating of the sponge, whereas no carbon signal could be detected in the case of the uncoated sample.

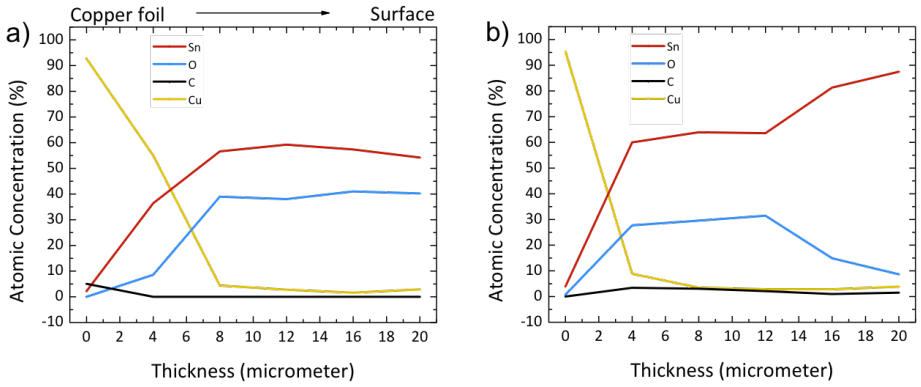

Figure 5.7 EDX cross section analysis before (a) and after coating and tempering (b).

The elemental composition of the film was further studied by X-ray photoelectron spectroscopy (XPS). High-resolution spectra of C and Sn elements before and after coating and tempering are shown in Figure 5.8a-b. Representative survey spectra are shown in Figure 5.8c. In the case of the non-coated sample, a low intensity carbon signal could be detected. Since XPS is a surface sensitive technique and as no carbon signal could be detected by EDX analysis, we assume the signal to originate from adventitious carbon. Curve fitting showed the signal to exhibit the typical peaks at 284.6, 286.2 and 288.9 eV resulting from C-C, C-O and C=O components respectively.[35] After coating, an increase in intensity of 18 % was observed for the C 1s-peak while the intensity of the Sn 3d5- and O 1s-peak decreased. A slight shift to lower binding energies indicates a lower oxidation state of the carbon as expected for the polymer. Two additional peaks appear at 287.7 and 292.6 eV. The peak at 287.7 eV can be attributed to the C-N bond resulting from nitrogen incorporated in the conjugated organic structure of the coating after pyrolysis.[36] A second peak is expected to appear at 285.9 eV originating from the C-N double bond. Because of the large overlap with the C-O peak, it was not possible to distinguish them, but the increase in intensity observed for the C-O peak compared to the non-coated sample points towards an additional contribution from the C-N double bond in the coating. Furthermore, a N 1s peak was observed at a binding energy of 400.1 eV in the coated sample, but not visible in the non-coated one (Figure 5.8d). Since cyanide groups appear at lower binding energies and the peak is rather broad (FWHM = 3.4 eV), we assume it to be the result from an overlap of the C-N bond and double bond peaks as suggested by Boyd *et al.*[37] The broad, low-intensity peak at 292.6 eV is the result of π-π* transitions (shake up) in the conjugated system. The Sn 3d5-signal consists of three components at 484.6, 486.3 and 487.0 eV, which could be attributed to Sn(0),

Sn(II) and Sn(IV) respectively, further confirming the appearance of SnO in the sample. The ratio of Sn to O was found to be 1:1.12, which is in good agreement with the results from EDX analysis. After coating, the Sn(II) signal increases from 78% to 85% while the Sn(IV) signal shows a decrease from 17% to 11% compared to the uncoated sample, reaffirming the observation of reduction of SnO_2 due to the heat treatment.

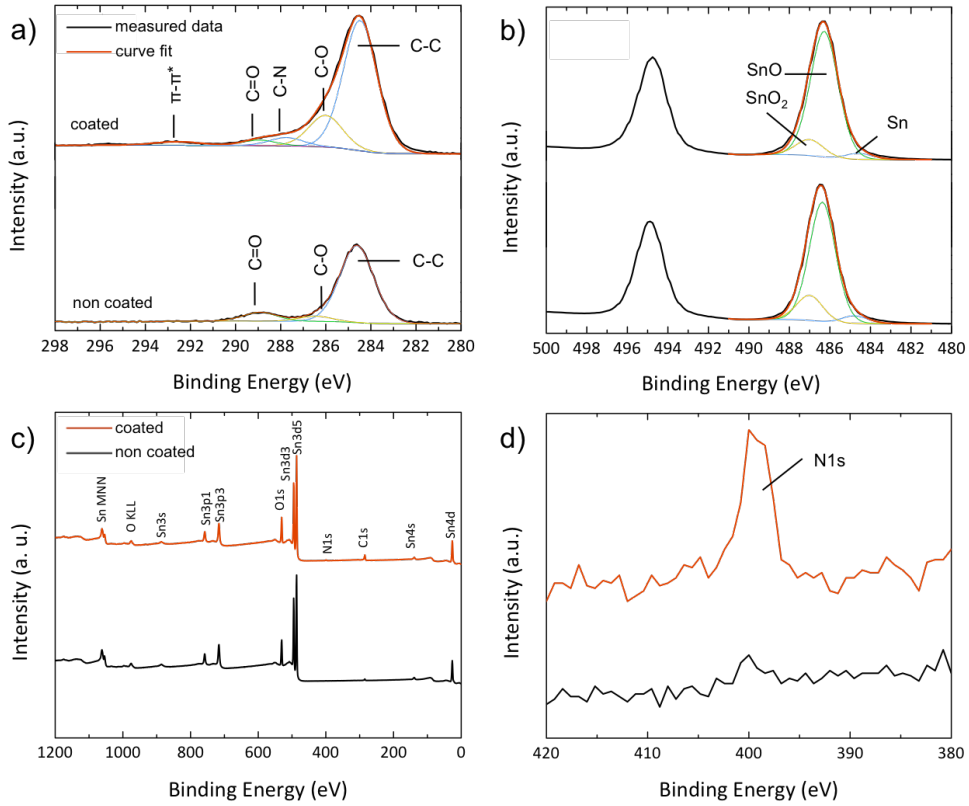

Figure 5.8 XPS spectra before and after coating and tempering. (a-b) High-resolution spectra from C1s and Sn3d peaks. c) Survey of anodized sample before (black) and after (red) coating and tempering. d) Magnification of N1s peak from survey.

The Raman spectrum (Figure 5.9) proves the presence of two bands typically observed for carbonaceous material, namely the D-band (1355 cm^{-1}) and the G-band (1591 cm^{-1}), which can be attributed to a delocalized sp^2 π -bonding.[38] As expected, none of these bands are observed for the uncoated sample.

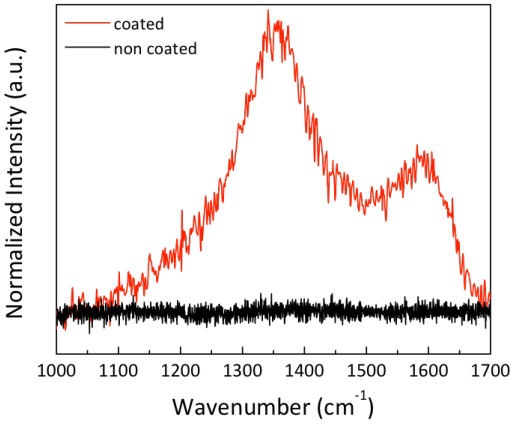

Figure 5.9 Raman spectrum of SnO_x sponge before (black) and after (red) coating. Measurement and data treatment performed by [redacted]

5.3.2 Electrochemical characterization of carbon coated SnO_x sponges

Electrodes based on as synthesized and carbon coated SnO_x sponges were applied as anodes in a lithium-ion battery half-cell set-up. Figure 5.10 shows the results of cyclic voltammetry for the uncoated and coated sample.

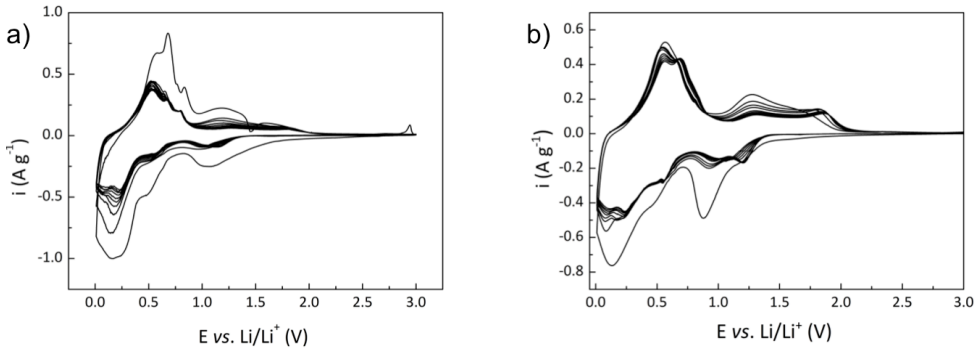

Figure 5.10 Cyclic voltammogram of uncoated SnO_x sponges (a) and carbon coated SnO_x sponges (b). Measurement and data treatment performed by [redacted]

In the first cathodic sweep of the carbon coated sponges a reduction peak at 0.9 V with a shoulder at 1.2 V can be observed, which is ascribed to the partially irreversible stepwise formation of elemental Sn and Li_2O as well as the formation of the solid electrolyte interface due to the decomposition of the electrolyte.[37][38][41] A shoulder at 0.45 V is followed by the main cathodic peak of the first cycle at 0.15 V, whereby the reactions occurring in the range of 0 to 0.6 V are ascribed to the formation of Li_xSn alloys.[40][41] The anodic main peak at 0.55 V as well as a second peak at 1.28 V are correlated to the stepwise dealloying processes of the Li_xSn alloys.[43] The peak at 1.6 V is ascribed to the at least partial decomposition of Li_2O.[41][42] The second as well as the following cycles show some differences compared to the first cycle, as the cathodic peak at 0.9 V is less pronounced and a

peak shows up at 1.2 V. Furthermore, the main cathodic is less pronounced. There is no change with respect to the anodic main peak, however, the intensity of the anodic peak at 1.28V is decreased and a second peak shows up at 1.8 V due to the decomposition of Li_2O.[42]

Compared to the carbon coated SnO_x sample, the uncoated sample shows similar features including an intensive cathodic peak due to the SEI formation, a cathodic main peak due to the alloying as well as the dealloying peaks. However, in the following cycles, the intensity of the cathodic peak at 1.2V and the anodic peak at 1.8 V is strongly reduced. Thus, the partial decomposition of Li_2O seems to be more reversible in the presence of the carbon coating.

In Figure 5.11 a comparison of the rate capability of coated and uncoated SnO_x sponges is presented. At the applied specific currents of 50, 100, 200 and 500 mA g^{-1} specific charge capacities of 400, 287, 220 and 102 mAh g^{-1}, respectively can be obtained for the uncoated SnO_x sponges. Significantly higher charge capacities of 600, 505, 431 and 260 mAh g^{-1} respectively can be obtained for the coated, which is for all applied specific currents more than 200 mAh g^{-1} higher compared to the uncoated sample, proving the positive influence of the carbon coating.

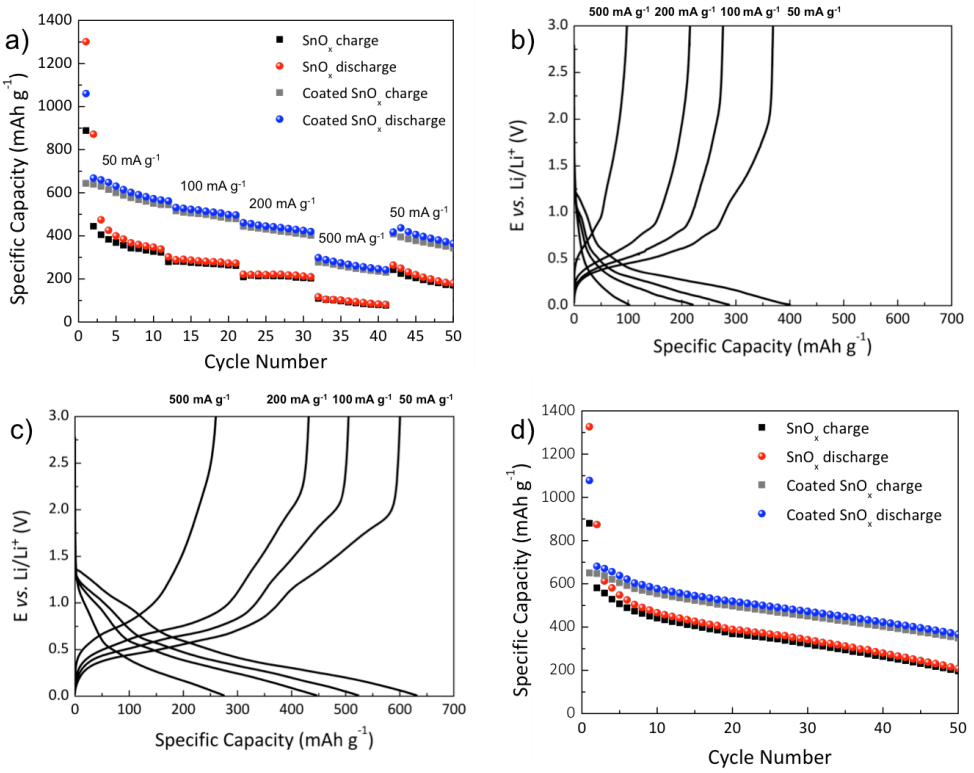

Figure 5.11 C-rate performance of uncoated and carbon coated SnOx sponges (a) and corresponding selected voltage profiles at the different applied specific currents of uncoated (b) and coated (c) SnOx sponges. d) Cycling at a constant specific current of 50 mA g-1; cut-off potentials: 0.01 and 3.0 V. Measurement and data treatment performed by [redacted].

Selected potential profiles of coated and uncoated sponges for the different specific currents are shown in Figure 5.11b and c respectively and are in a good agreement with the results from cyclic voltammetry. A voltage plateau at 0.45 V can be observed during the discharge and plateau at 0.5 V during the charge due to the alloying and dealloying reactions. These plateaus are more pronounced at lower specific currents and are more pronounced for the coated compared to the uncoated sample. Furthermore, in case of the coated sample a higher gain of specific capacity can be observed during charge in the region of 1.25 V to 2.0 V related to a higher reversibility of the decomposition of Li_2O due to the presence of a conductive carbon

coating.[23] Figure 5.11d shows 50 cycles of the carbon coated and uncoated SnO_x sponges at 50 mA g^{-1}. In case of the uncoated sponges the charge capacity drops rapidly within the first 10 cylces from 880 to 441 mAh g^{-1}. In contrast, the initial discharge capacity of the coated sample is lower (650 mAh g^{-1}), but the capacity retention is higher, as the discharge capacity after 10 cycles is still 555 mAh g^{-1}. The obtained specific capacity for the coated sample is up to the 50^{th} cycle constantly 120 mAh g^{-1} higher compared to the uncoated sponges.

Potential profiles of selected cycles up to cycle 20 are shown in Figure 7.17 (Appendix) and prove the enhanced cycling performance of coated SnO_x sponges. In case of uncoated sponges the plateau of the charge profile in the voltage region between 0.5 and 0.75 V decreases, but more dramatically is even the decrease of capacity gain above 1.0 V upon cycling, whereas the plateau between 0.5 and 0.75 V related to the dealloying reaction appears to be very reversible in case of the coated sample.

Compared to previous reports on nanoporous tin oxide, which report capacities of less than 300 mAh g^{-1} after 20 cycles in the voltage range of 0.01 V to voltages higher than 1.8 V,[17][18] the carbon coated sample shows a strongly enhanced battery performance, as still a discharge capacity of 497 mAh g^{-1} can be obtained.

The morphology of the sponge-like structure was investigated after galvanostatic cycling by *ex situ* SEM measurements as shown in Figure 5.12 for C-SnO_x samples after the first and fifth charge. Obviously, the sponge-like morphology could be retained upon continuous (dis-)charging, as the porous structure is clearly observable after cycling.

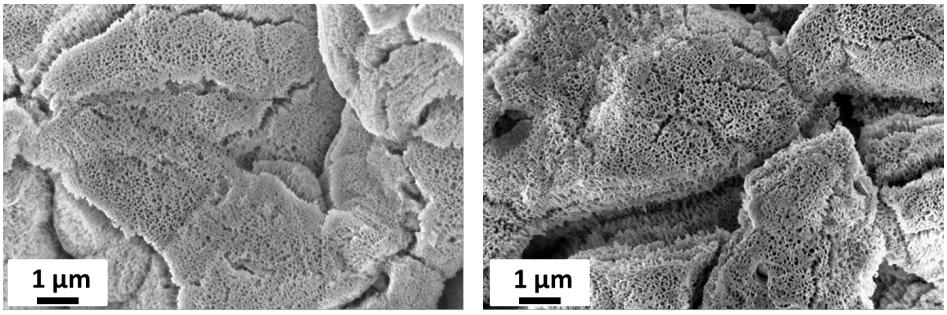

Figure 5.12 SEM images of C-SnO_x electrodes after a) the first charge and b) after the fifth charge showing the preservation of the sponge-like morphology even after cycling. Measurement performed by [redacted]

5.4 Conclusions

In summary, the synthesis of sponge-like SnO_x films deposited onto copper foil was described. The film was coated with a block copolymer containing carbon precursor polymer, followed by annealing to get a thin homogeneous carbon film. Composition of the SnO_x film was investigated before and after coating using XRD, EDX, XPS and Raman-spectroscopy and proves the sponge-like morphology and the presence of a carbon film in case of the coated sample. The tin oxide film was found to mainly consist of tin(II) oxide prior to coating, while a partial reduction was observed during the heat treatment. Electrochemical characterization shows that the coated SnO_x sponge exhibits an increased specific capacity and higher cycling stability compared to the non-coated sample. The porous structure of the SnO_x film could be retained even upon cycling as proven by ex situ SEM measurements.

5.5 References

[1] S. Shanmugam and A. Gedanken, "Carbon-coated anatase TiO2 nanocomposite as a high-performance electrocatalyst support," *Small*, vol. 3, no. 7, pp. 1189–1193, 2007.

[2] C. Mahendiran, T. Maiyalagan, K. Scott and A. Gedanken, "Synthesis of a carbon-coated NiO/MgO core/shell nanocomposite as a Pd electro-catalyst support for ethanol oxidation," *Mater. Chem. Phys.*, vol. 128, no. 3, pp. 341–347, 2011.

[3] A. S. Aricò, P. Bruce, B. Scrosati, J.-M. Tarascon and W. van Schalkwijk, "Nanostructured materials for advanced energy conversion and storage devices," *Nat. Mater.*, vol. 4, no. 5, pp. 366–377, 2005.

[4] P. G. Bruce, B. Scrosati and J.-M. Tarascon, "Nanomaterials for rechargeable lithium batteries.," *Angew. Chem. Int. Ed. Engl.*, vol. 47, no. 16, pp. 2930–2946, 2008.

[5] B. Oschmann, D. Bresser, M. N. Tahir, K. Fischer, W. Tremel, S. Passerini and R. Zentel, "Polyacrylonitrile block copolymers for the preparation of a thin carbon coating around TiO2 nanorods for advanced lithium-ion batteries," *Macromol. Rapid Commun.*, vol. 34, no. 21, pp. 1693–1700, 2013.

[6] J. S. Chen and X. W. Lou, "SnO2-based nanomaterials: Synthesis and application in lithium-ion batteries," *Small*, vol. 9, no. 11, pp. 1877–1893, 2013.

[7] Y. Idota, "Tin-Based Amorphous Oxide: A High-Capacity Lithium-Ion-Storage Material," *Science*, vol. 276, no. 5317, pp. 1395–1397, 1997.

[8] J. M. Tarascon and M. Armand, "Issues and challenges facing rechargeable lithium batteries.," *Nature*, vol. 414, no. 6861, pp. 359–367, 2001.

[9] J. S. Chen, Y. L. Cheah, Y. T. Chen, N. Jayaprakash, S. Madhavi, Y. H. Yang and X. W. Lou, "SnO2 nanoparticles with controlled carbon nanocoating as high-capacity anode materials for lithium-ion batteries," *J. Phys. Chem. C*, vol. 113, no. 47, pp. 20504–20508, 2009.

[10] X. W. Lou, J. S. Chen, P. Chen and L. A. Archer, "One-pot synthesis of carbon-coated SnO2 nanocolloids with improved reversible lithium storage properties," *Chem. Mater.*, vol. 21, no. 13, pp. 2868–2874, 2009.

[11] D. Larcher, S. Beattie, M. Morcrette, K. Edström, J.-C. Jumas and J.-M. Tarascon, "Recent findings and prospects in the field of pure metals as negative electrodes for Li-ion batteries," *Journal of Materials Chemistry*, vol. 17, no. 36, p. 3759, 2007.

[12] J. Besenhard, M. Hess and P. Komenda, "Dimensionally stable Li-alloy electrodes for secondary batteries," *Solid State Ionics*, vol. 40–41, pp. 525–529, 1990.

[13] L. Zhang, H. Bin Wu and X. (David) Wen Lou, "Growth of SnO2 nanosheet arrays on various conductive substrates as integrated electrodes for lithium-ion batteries," *Mater. Horizons*, vol. 1, p. 133, 2014.

[14] X. W. Lou, L. A. Archer and Z. Yang, "Hollow micro-/nanostructures: Synthesis and applications," *Advanced Materials*, vol. 20, no. 21, pp. 3987–4019, 2008.

[15] B. Wang, B. Luo, X. Li and L. Zhi, "The dimensionality of Sn anodes in Li-ion batteries," *Mater. Today*, vol. 15, no. 12, pp. 544–552, 2012.

[16] C. Wang, G. Du, K. Ståhl, H. Huang, Y. Zhong and J. Z. Jiang, "Ultrathin SnO2 nanosheets: Oriented attachment mechanism, nonstochiometric defects, and enhanced lithium-ion battery performances," *J. Phys. Chem. C*, vol. 116, no. 6, pp. 4000–4011, 2012.

[17] G. F. Ortiz, P. Lavela, P. Knauth, T. Djenizian, R. Alcántara and J. L. Tirado, "Tin-Based composite Materials Fabricated by Anodic Oxidation for the Negative Electrode of Li-Ion Batteries," *Journal of The Electrochemical Society*, vol. 158, no. 10, p. A1094, 2011.

[18] J. W. Lee, S. J. Park and H. C. Shin, "Electrochemical characterization of anodic tin oxides with nano-porous structure," *Korean J. Mater. Res.*, vol. 21, no. 1, pp. 21–27, 2011.

[19] S. J. Park and H. C. Shin, "Fabrication of nano-channeled tin oxide film electrode and evaluation of its electrochemical properties," *Korean J. Mater. Res.*, vol. 22, no. 1, pp. 1–7, 2012.

[20] H. Li and H. Zhou, "Enhancing the performances of Li-ion batteries by carbon-coating: present and future," *Chemical Communications*, vol. 48, no. 9, p. 1201, 2012.

[21] D. Bresser, B. Oschmann, M. N. Tahir, F. Mueller, I. Lieberwirth, W. Tremel, R. Zentel and S. Passerini, "Carbon-Coated Anatase TiO2 Nanotubes for Li- and Na-Ion Anodes," vol. 162, no. 2, pp. A3013–A3020, 2015.

[22] A. Moretti, G. T. Kim, D. Bresser, K. Renger, E. Paillard, R. Marassi, M. Winter and S. Passerini, "Investigation of different binding agents for nanocrystalline anatase TiO2 anodes and its application in a novel, green lithium-ion battery," *J. Power Sources*, vol. 221, pp. 419–426, 2013.

[23] B. Oschmann, M. N. Tahir, F. Mueller, D. Bresser, I. Lieberwirth, W. Tremel, S. Passerini and R. Zentel, "Precursor Polymers for the Carbon Coating of Au@ZnO Multipods for Application as Active Material in Lithium-Ion Batteries," *Macromol. Rapid Commun.*, vol. 36, no. 11, pp. 1075-1082, 2015.

[24] D. M. Piper, T. A. Yersak, S. B. Son, S. C. Kim, C. S. Kang, K. H. Oh, C. Ban, A. C. Dillon and S. H. Lee, "Conformal coatings of cyclized-PAN for mechanically resilient Si nano-composite anodes," *Adv. Energy Mater.*, vol. 3, no. 6, pp. 697–702, 2013.

[25] D. E. Bergbreiter, P. L. Osburn, and C. Li, "Soluble polymer-supported catalysts containing azo dyes," *Org. Lett.*, vol. 4, no. 5, pp. 737–740, 2002.

[26] A. He, Q. Liu, and D. G. Ivey, "Electrodeposition of tin: A simple approach," *J. Mater. Sci. Mater. Electron.*, vol. 19, pp. 553–562, 2008.

[27] H.-C. Shin, J. Dong, and M. Liu, "Porous Tin Oxides Prepared Using an Anodic Oxidation Process," *Adv. Mater.*, vol. 16, no. 3, pp. 237–240, 2004.

[28] J. W. Lee, S. J. Park, W. S. Choi, and H. C. Shin, "Well-defined meso- to macro-porous film of tin oxides formed by an anodization process," *Electrochim. Acta*, vol. 56, no. 17, pp. 5919–5925, 2011.

[29] X. Hou, Y. Hu, H. Jiang, Y. Li, W. Li, and C. Li, "One-step synthesis of SnO_x nanocrystalline aggregates encapsulated by amorphous TiO_2 as an anode in Li-ion battery," *J. Mater. Chem. A*, vol. 3, no. 18, pp. 9982–9988, 2015.

[30] D. M. Mukhamedshina, K. a. Mit, N. B. Beisenkhanov, E. a. Dmitriyeva, and I. V. Valitova, "Influence of plasma treatments on the microstructure and electrophysical properties of SnOx thin films synthesized by magnetron sputtering and sol-gel technique," *J. Mater. Sci. Mater. Electron.*, vol. 19, pp. 382–387, 2008.

[31] L. Zaraska, N. Czopik, M. Bobruk, G. D. Sulka, J. Mech, and M. Jaskuła, "Synthesis of nanoporous tin oxide layers by electrochemical anodization," *Electrochim. Acta*, vol. 104, pp. 549–557, 2013.

[32] M. Zorn, S. Meuer, M. N. Tahir, Y. Khalavka, C. Sönnichsen, W. Tremel and R. Zentel, "Liquid crystalline phases from polymer functionalised semiconducting nanorods," *Journal of Materials Chemistry*, vol. 18, no. 25, p. 3050, 2008.

[33] J.-H. Jeun, H.-S. Ryu and S.-H. Hong, "Nanoporous SnO2 Film Gas Sensor Formed by Anodic Oxidation," *J. Electrochem. Soc.*, vol. 156, no. 9, p. J263, 2009.

[34] A. Palacios-padrós, M. Altomare, K. Lee and I. Díez-pørez, "Controlled Thermal Annealing Tunes the Photoelectrochemical Properties of Nanochanneled Tin-Oxide Structures," *ChemElectroChem*, vol. 1, no. 7, pp. 1133–1137, 2014.

[35] T. L. Barr, "Nature of the use of adventitious carbon as a binding energy standard," *Journal of Vacuum Science & Technology A: Vacuum, Surfaces, and Films*, vol. 13, no. 3, p. 1239, 1995.

[36] K. D. B. J.F. Moulder, W.F. Stickle, P.E. Sobol, *Handbook of X-ray Photoelectron Spectroscopy*. Eden Prairie, MN: Perkin-Elmer Corp, 1992.

[37] K. J. Boyd, "Formation of C–N thin films by ion beam deposition," *Journal of Vacuum Science & Technology A: Vacuum, Surfaces and Films*," vol. 13, no. 4. p, 2110, 1995.

[38] A. C. Ferrari and J. Robertson, "Raman spectroscopy of amorphous, nanostructured, diamond-like carbon and nanodiamond," *Philos. Trans. A. Math. Phys. Eng. Sci.*, vol. 362, no. 1824, pp. 2477–2512, 2004.

[39] I. A. Courtney, "Electrochemical and In Situ X-Ray Diffraction Studies of the Reaction of Lithium with Tin Oxide Composites," *Journal of The Electrochemical Society*, vol. 144, no. 6, p. 2045, 1997.

[40] Z. Wen, F. Zheng, H. Yu, Z. Jiang and K. Liu, "Hydrothermal synthesis of flowerlike SnO2 nanorod bundles and their application for lithium ion battery," *Mater. Charact.*, vol. 76, pp. 1–5, 2013.

[41] E. Peled, "The Electrochemical Behavior of Alkali and Alkaline Earth Metals in Nonaqueous Battery Systems—The Solid Electrolyte Interphase Model," *Journal of The Electrochemical Society*, vol. 126, no. 12, p. 2047, 1979.

[42] X. W. Lou, C. M. Li and L. A. Archer, "Designed synthesis of coaxial SnO2@carbon hollow nanospheres for highly reversible lithium storage," *Adv. Mater.*, vol. 21, no. 24, pp. 2536–2539, 2009.

[43] M. Mohamedi, S.-J. Lee, D. Takahashi, M. Nishizawa, T. Itoh and I. Uchida, "Amorphous tin oxide films: preparation and characterization as an anode active material for lithium ion batteries," *Electrochimica Acta*, vol. 46, no. 8, pp. 1161–1168, 2001.

[44] T. Brousse, "Thin-Film Crystalline SnO2-Lithium Electrodes," *Journal of The Electrochemical Society*, vol. 145, no. 1, p. 1, 1998.

6 Controlled Synthesis and Growth Mechanism for the Anodization of Iron

6.1 Introduction

Iron can be oxidized to different valence states such as FeO, Fe_3O_4 and Fe_2O_3. Among those valence states, Fe_2O_3 has been investigated widely because of the potential application as photocatalyst,[1][2][3][4][5] gas sensor,[6][7] and lithium ion battery electrode.[8][9] Among various nanostructure morphologies, vertically aligned nanotubes offer a high degree of surface area while the anodization route allows an easy control of pore length, diameter and wall thickness. In contrast to the anodization of other valve metals, which are usually carried out at room temperature, anodization of iron is strongly dependent on the temperature of the electrolyte *e.g.* Brownian motion and mass transport.[10] At room temperature well defined iron oxide nanotubes of up to 1 µm in length could be prepared by vigorously stirring the electrolyte.[11] A sonoelectrochemical anodization method yielded nanotubes with a length from 40nm to 2 µm.[12] At lower temperatures only nanoporous structures can be synthesized with a length of about 500 nm.[13] By increasing the temperature and thus increasing the viscosity and diffusion speed of the electrolyte, nanotubes with a length of up to 3 µm could be achieved.[10]

The goal of this work is a better understanding of the growth mechanism of iron oxide nanotubes and to increase pore length and control pore diameter while maintaining a high film quality.

In this chapter, several parameter of the anodization were investigated on their effect on film quality. A growth mechanism could be proposed, explaining the current behavior and varying film quality during the anodization. Composition of the film was

investigated via X-ray diffraction and by cross section measurements. A thinning of the nanotube diameter towards the bottom and imprints in the bulk metal could be observed. The imprints could be used in the future to further increase film quality by a second anodization.

6.2 Experimental

6.2.1 Materials

All starting materials were used without further purification. Commercially available iron foil with a thickness of 0.25 mm and a purity of ≥ 99.99% trace metal basis was purchased from Sigma Aldrich. The foil was cut down to round plates with a diameter of 20 mm. Polishing solution consisted of n-butanol (99%, Acros Organics), methanol (p.A., Sigma-Aldrich), perchloric acid (Sigma-Aldrich) and MilliQ-water (18.3 ΩM/cm[14]). As electrolyte, ammoniumfluoride (p.A., Sigma-Aldrich), ethyleneglycol (99%, ChemPur) and MilliQ-water (18.3 ΩM/cm) was used.

6.2.2 Experimental Setup

Anodic bias for all reactions was applied via a Voltcraft PSP 1803 voltage source. For the reactions, a custom made setup was used (see Chapter 2.2.3). Instead of the PTFE-cylinder utilized in the anodization of tin, a modified version with a larger cutout at the bottom of 15 mm and a conical shape was applied. A custom made steel electrode was used as cathode. It was coupled to a Velp Scientifica Stirrer ES laboratory stirrer to enable rotation. For heating of the electrolyte, a custom-made glass coil was used, coupled to a thermostat for temperature control.

6.2.3 Sample Preparation

Prior to electropolishing, samples were rinsed ultrasonically in ethanol, washed with acetone and air-dried. Electropolishing was performed with the standard polishing solution (see Chapter 2.2.1). The solution consisted of 900 ml MeOH, 600 ml BuOH, 85.7 ml 70% $HClO_4$ and 14.3 ml MilliQ-water. For every electropolishing step, 30 ml of cooled (T = -28 °C) solution were filled into the PTFE-cylinder and a constant anodic bias of 40 V was applied for 5 minutes via an rotating steel electrode positioned at the bottom of the cylinder cutout, close to the sample surface. After electropolishing, the sample was quickly washed with water, acetone and then air-dried to prevent oxidation. Anodization was carried out in the same setup equipped with a custom-made glass coil, which was connected to a circuit heater to control the temperature of the electrolyte. The electrolyte consisted of 0.3 wt% ammoniumfluoride and ethylene glycole[10] containing different percentages of water. The solution was heated to different temperatures, varying applied voltage and reaction times.

6.2.4 Characterization

Scanning electron microscopy (SEM)

Surface topography was analyzed using a high-vacuum mode scanning electron microscope (SEM; FEI Quanta 200 FEG Environmental-SEM, FEI Deutschland GmbH, Frankfurt / Main, Germany) at an acceleration voltage of 15 kV.

Laser Microscopy

Laser microscopy images were recorded using a confocal Keyence VK-8710 laser microscope. As guiding value for surface roughness, the Rq value was used. It is calculated as followed:

$$R_q = \sqrt{(\frac{1}{N} * \sum (z(x) - < z >)^2)}$$

The variable z is the difference between the heights of the sample to an imaginary plane through the mean height of the sample.

X-ray diffraction (XRD)

The crystal structure of tin was examined via room temperature X-ray diffraction on a Bruker D8 Discover instrument operated in reflection geometry with a CuK$\alpha_{1,2}$ X-ray source.

6.3 Results and Discussion

6.3.1 Electropolishing

As purchased iron foil exhibits a noticeable roughness from rolling of the foil. Compared to tin, surface roughness is even higher with an Rq-value of 0.67 µm and height differences of more than 5 µm are visible as shown by laser microscopy (Figure 6.1).

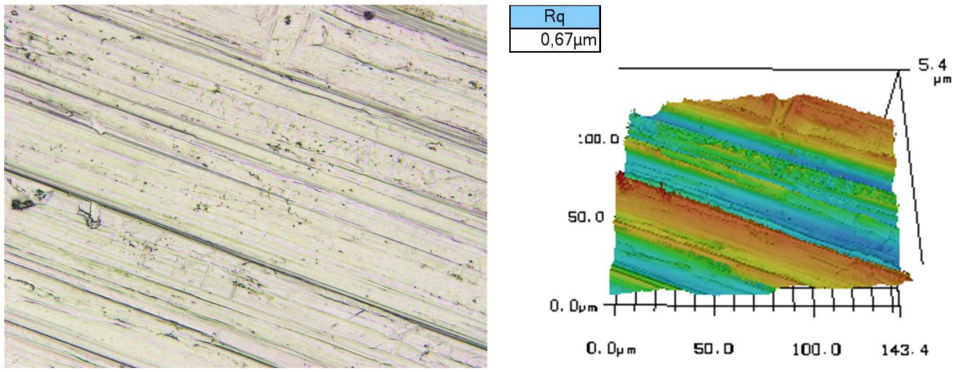

Figure 6.1 As purchased iron foil. Left: Light microscopy image Right: 3D topographic image extended 10-fold in z-axis

If an anodic bias is applied to the foil without stirring of the solution, the surface is oxidized and a brown-orange colored film becomes visible. This film, presumably iron oxide judging from the color, functions as a blocking layer, resulting in a drop in current density. Based on the experience with tin, stirred polishing was examined. Even though a larger version of the stirring cathode was manufactured (see Figure 6.2 left) to comply with the increased diameter of the foils, stirring did not seem to be effective enough to remove the oxide as fast as it was produced. Because of the larger diameter of the electrode, the increased height difference between the lowest and highest point of the tip also became a problem. Since the outer regions of the foil were

dissolved more quickly due to higher current density and possibly better stirring, the surface of polished foils became uneven, rough in the center and smooth on the rim. Following those results, a new double-cut electrode and an adjusted PTFE-cylinder were manufactured (Figure 6.2 right). The axe-like shape of the tip increased stirring close to the surface while decreasing the effective height difference. The PTFE-cylinder maximized stirred volume of the solution by removing the tunnel-like shape of the cutout. Result of both measures was an effective removal of the oxide from the surface, allowing homogeneous polishing of the foil.

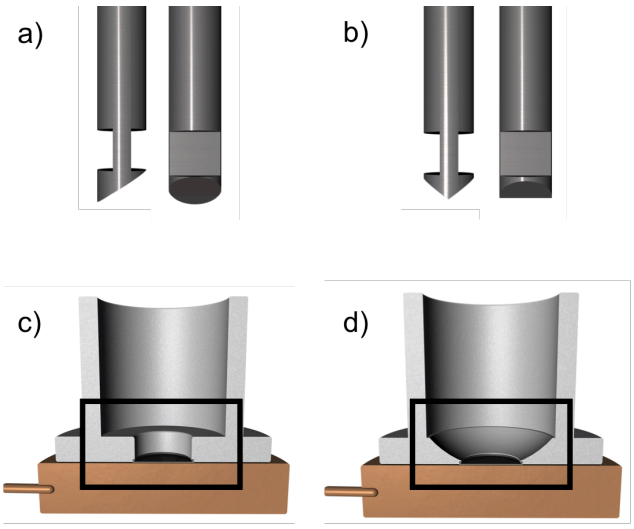

Figure 6.2 Illustration of electrode tips and setups used for electropolishing a) Single-cut electrode b) Double-cut electrode c) PTFE-cylinder without cutout d) Adjusted PTFE-cylinder with conical cutout.

After electropolishing, the surface was almost completely flat as it can be seen in the light microscopy image (Figure 6.3 left). Dark spots remained, possible due to impurities of the foil, as it was not possible to eliminate them by any measure taken. Roughness decreased drastically to 0.07 µm confirming a successful polishing.

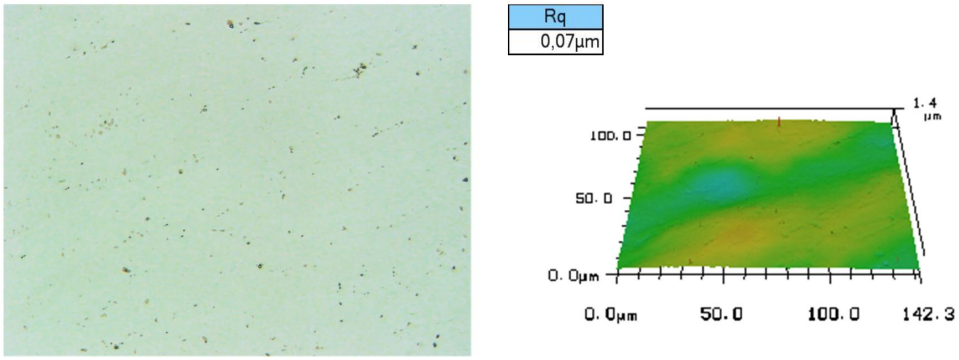

Figure 6.3 Polished iron foil. Left: Light microscopy image Right: 3D topographic image extended 10-fold in z-axis.

6.3.2 Anodization

As mentioned above, anodization temperature has a strong effect on the morphology of the anodized film. Since the setup consists of a large copper block with a great heat capacity, values found in literature had to be adjusted. The time the electrolyte was in contact with the foil without applied bias was minimized by heating the electrolyte in a plastic beaker to the desired temperature controlled by a contact thermometer. By using a custom-built glass coil connected to a circuit heater, a temperature in the setup as stable as possible was achieved. To find the optimal temperature for the electrolyte, short anodizations of three minutes were carried out at different temperatures. Up to 50°C, no porous structure is formed. The surface is covered in nanoleaflets and flower-like structures (see Figure 6.4 top left).[15] Compared to higher temperatures, the initial drop in current is less steep as the surface passivation layer does not seem to be as thick or complete as the one produced at higher reaction temperatures (Figure 6.5). As the reaction continues, the current slowly increases and exhibits several spikes. These can be attributed to a continuous passivation and dissolution of the passive layer. At a temperature of 60 °C, some regions of the sample show a porous film with holes of about 19 nm in diameter (Figure 6.4 top right and Figure 7.18a Appendix). In other regions, nanoleaflets are found, as the reaction is not homogeneous over the whole sample. The initial drop in current is comparable to the reaction at 50 °C, reflecting the incomplete or thin coverage by the passivation layer, but no spikes in current are visible pointing to a more homogeneous reaction (Figure 6.5). Further increase of the temperature to 65 °C leads to a uniform porous layer with a pore diameter on the surface of 22 nm (Figure 6.4 bottom left and Figure 7.18b Appendix). As the viscosity decreases the mobility of the electrolyte, and so the mass transport, increases. The initial drop in current is higher as the whole surface

passivates (Figure 6.5). Subsequently, a slow increase is visible reaching a plateau after about 120 seconds. The increase in current is due to the formation of the nanopores as the passivation layer is dissolved and the thickness *e.g.* the effective resistivity decreases (see Chapter 6.3.3). At 70 °C, pore distribution is more homogeneous and first self-ordering can be observed (see magnification Figure 6.4 bottom right). Diameter of the pores openings increases to 30 nm (Figure 7.18c Appendix). Initial drop in current is once again higher due to a thicker passivation layer (Figure 6.5). As expected from the similarity in surface structure, the current shows a behavior comparable to the reaction at 65 °C. Due to the capacities of the thermostat used, investigation of higher electrolyte temperatures was not possible.

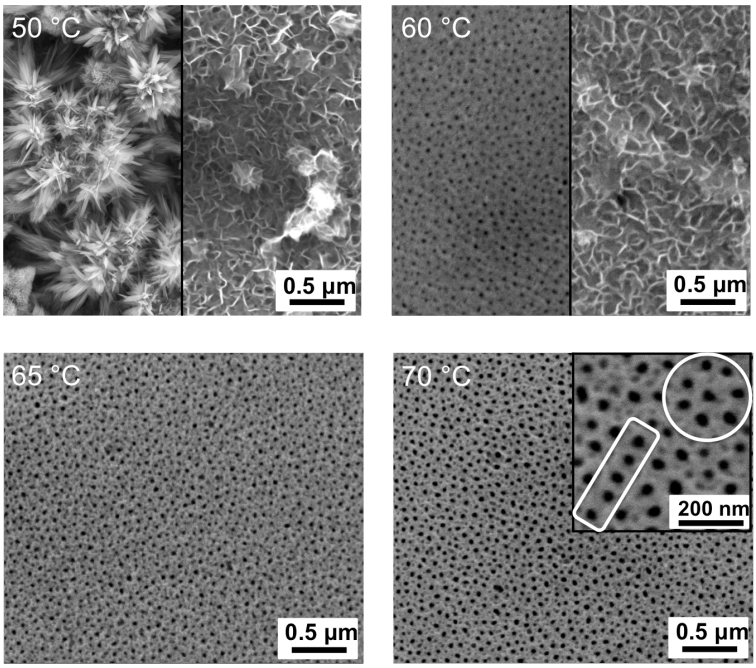

Figure 6.4 SEM images of iron foil after anodization for 3 min at 50 V in electrolyte heated to temperature of 50 to 70 °C.

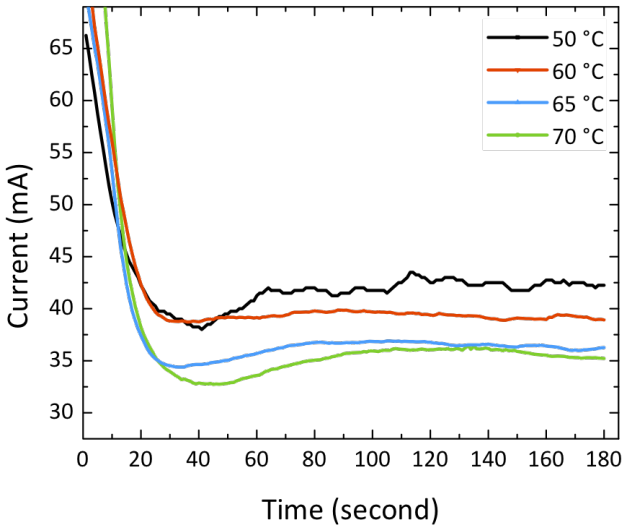

Figure 6.5 Current curves of anodization in electrolyte heated to different temperatures.

Anodization for 30 minutes at 70 °C leads to a homogeneous nanoporous film of 2.80 µm thickness (Figure 6.6). Diameter of the opening of the pores increases massively up to 50 nm with a decreased standard deviation of 6 nm reflecting the higher homogeneity of the film (see Figure 7.19a Appendix).

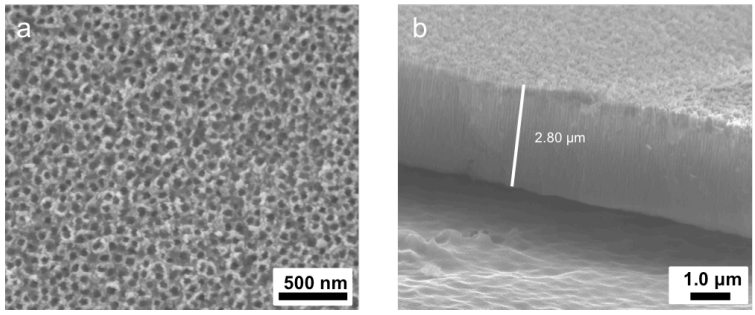

Figure 6.6 SEM images of iron foil after anodization at 70 °C with 50 V for 30 min. a) Top view of nanoporous film with a pore diameter of 50 nm. b) Cross section view of anodized film.

6.3.3 Growth Mechanism

For a further understanding of the growth mechanism, the anodized foil was investigated in SEM after different anodization times. Even though, the growth mechanism was already studied for the initial 120 seconds of anodization by Misra *et al.,*[16] no detailed analysis of the subsequent reaction steps was reported in literature. In the theoretical approach to pore formation, a current curve exhibits an initial drop in current due to passivation of the surface. Then, current increases as pores are etched into the oxide. After some time, equilibrium is reached, as the increase in current due to increase in surface area is evened out by the thicker oxide film and thus a decreasing mass transport through the pores. The result is a constant current, which slowly decreases after some time as pores get grow and mass transport through the pores decreases (see Chapter 1.2.3).

The current curve for the anodization of iron is noticeable different. A typical current curve is shown in Figure 6.7. A longer anodization time was used for further explanation of the growth mechanism.

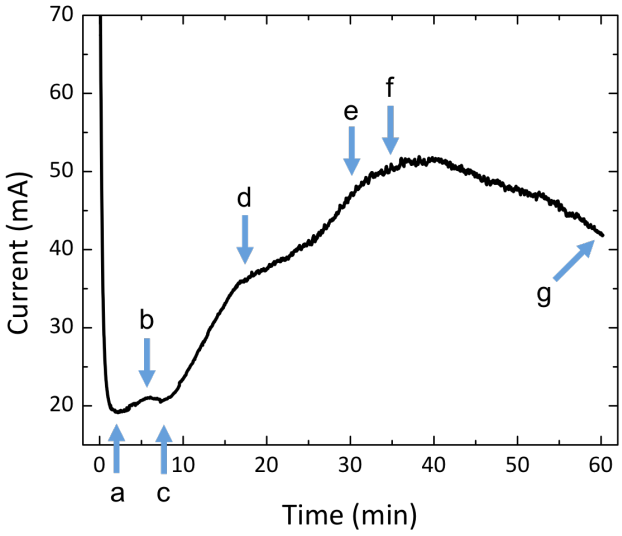

Figure 6.7 Current curve for an anodization at 50 V for 2 h. (a) First minimum after initial drop, (b) Local Maximum, (c) Second Minimum, (d) First Increase, (e) Second Increase ,(f) Maximum, (g) Final decrease

In the beginning of the reaction, the surface is passivated as the iron reacts with water (1) and fluoride ions (2) in the electrolyte forming a mixed layer of iron oxide and iron fluoride. As iron oxide is a semiconductor and iron fluoride an insulator, current flow is decreased. Since dissolution of the oxide already begins, the film appears porous. Cross section measurement reveals the "pores" to be mere indentations on the surface of the compact passivation layer with thickness of about 300 nm (see Figure 6.10a1-2). Since the diffusion rate of fluoride ions is two times the rate of oxygen ions, fluoride-containing iron accumulates closer to the surface, forming a bottom layer.

$$2\,Fe\ +\ 3\,H_2O\ \rightarrow\ Fe_2O_3\ +\ 6\,e^-\ +\ 6H^+ \qquad (1)$$

$$Fe\ +\ 3F^-\ \rightarrow\ FeF_3\ +\ 3\,e^- \qquad (2)$$

In the next step, pores are formed by dissolution of the oxide layer to iron(III) hexafluoride anions (IHF) (3), resulting in an increase in current density (Figure 6.10b). Since hydroxide ions are necessary for the reaction, locally the pH seems to drop to a certain degree, allowing for the hydrolysis of iron(II) fluoride (4). Hydrofluoric acid formed in the reaction also promotes the dissolution of iron oxide.

$$Fe_2O_3\ +\ 6\,H^+\ +\ 12\,F^-\ \rightarrow\ 2\,[FeF_6]^{3-}\ +\ 3\,H_2O \qquad (3)$$

$$FeF_3\ +\ 3\,H_2O\ \rightarrow\ Fe(OH)_3\ +\ 3\,HF \qquad (4)$$

$$HF\ \rightarrow\ H^+\ +\ F^- \qquad (5)$$

For the following decrease in current, several explanations are possible. The theory showing the highest probability is presented here but it should be noted that further investigation is necessary for a final decision on the validity of this theory. Since the solution is not agitated, IHF seem to accumulate at the bottom of the pores and decreases the effective potential. Since the pores are short, the effect of the anodic protection, as described by Wang *et al.*,[17] is small. The decrease in potential at the bottom of the pores seems to equilibrate the potential difference, slowing the dissolution of oxide at the bottom of the pores, which leads to an effective decrease in the current flow. The surface morphology does not change significantly during this time as seen in Figure 6.10c. The surface is slightly etched, which is expected as the dissolution reaction of the oxide on top of the pores continues. Due to Brownian motion, the accumulated IHFs are slowly transported out of the pores, while bringing

in fresh electrolyte. This approach is supported by a comparison of the current curve with an anodization where the electrolyte was stirred. Figure 6.8 shows current curves of an anodization for three minutes with and without stirring. While both reactions produce a nanoporous film, the non-stirred reaction does not show the observed decrease in current. Stirring motion quickly transports the dissolved iron fluoride out of the pores and prevents accumulation. Even though, stirring seems to homogenize the reaction conditions, it was not used due to several disadvantages mentioned in Chapter 6.3.7. Furthermore, pore formation is only observed at high temperatures, which means increased Brownian motion. Another approach to increase film quality was the assistance of ultrasonic sound, which also can be translated into micro stirring as it increases mass transport.[12] A decrease of the concentration of water also reduces the effect since it slows down the reaction, decreasing the rate of accumulation of IHF. At 2 wt% only a slight decrease of the slope of the current curve is visible while at 1 wt% the effect does not occur at all. Brownian motion seems to remove IHF as fast as it is produced (see Chapter 6.3.6).

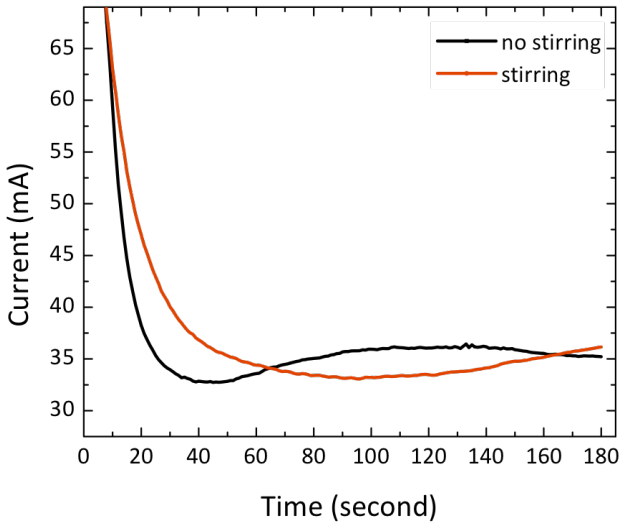

Figure 6.8 Current curves of anodization with (red) and without (black) stirring.

When IHF is transported out of the pores the effective anodic potential increases and the dissolution reaction begins again. Pores grow as the bottom layer is thinned by partial dissolution, visible by the increase in current. In the following 10 minutes, the pores grow to a length of up to 2.2 µm (Figure 6.10d1-2). Since the current curve shows almost plateau-like behavior before and after the current increase, the possibility of a phase transfer was also investigated by comparing X-ray diffraction patterns of the film after different anodization times (see Figure 6.9). After 6.5 min, right after the second current decrease, the sample consists of a thin layer of amorphous Bernalite, Iron Oxide Hydroxide and Magnetite. Remaining reflexes can be attributed to the underlying iron foil. After 20 min and the subsequent current increase, the sample shows a higher degree of crystallinity and consists of Akaganeite and Magnetite.

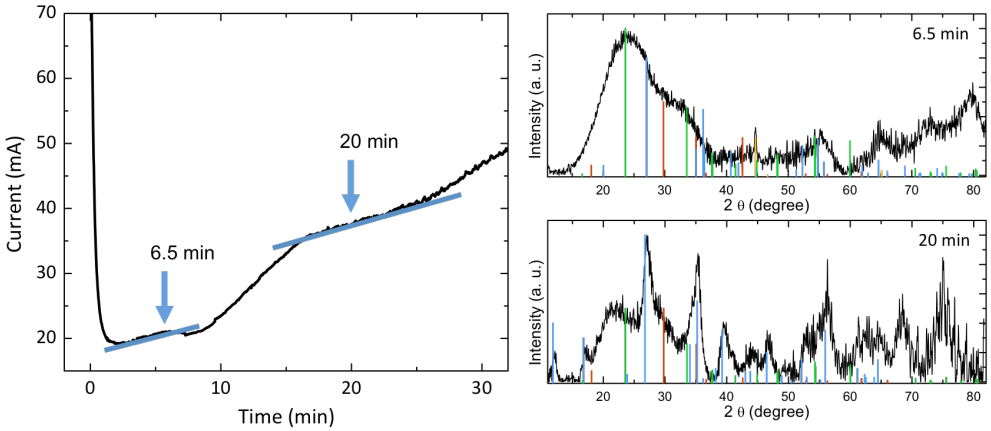

Figure 6.9 Current curve with two plateaus as indicated by blue lines (left) and X-ray micro diffraction of anodized iron foil after 6.5 min (top right) and 20 min (bottom right) Reflex patterns for Iron (yellow), Magnetite (blue), Akaganeite (red) and Bernalite (green)

Relative intensity of the main reflection of Bernalite decreased, indicating a lower degree of hydration of the film. Because of the now thicker film, no reflexes of iron were visible. Changes in crystallinity and hydration indicate a possible phase transfer but due to the amorphous nature of the film, relative quantity and composition could not be distinguished exactly.

As the reaction continues, subsequent accumulation of IHF leads to a decrease in reaction rate, but due to the higher length of the pores and the increased anodic protection, the effect is less pronounced, only decreasing the slope of the current curve. Furthermore, as the pores grow longer, fluoride ions seem to migrate preferentially in a radial direction because of the electric field present within the nanopores.[16] The interpore boundaries are enriched with fluoride, decreasing the concentration of fluoride and thus the effective accumulation of IHF at the pore bottom. After 3 - 4 minutes, speed of the pore formation increases again but due to longer pores and the slower mass transport, the increase is also less pronounced. The pores grow to the final size of 2.8 µm (Figure 6.10e1-2). Now, different effects come

into play. Accumulation of IHF again leads to a slightly decreased dissolution of the pore bottom. Also the pH has decreased over the reaction time, increasing the rate of dissolution of iron fluoride in the interpore boundaries. This leads to a slow transformation of the nanopores to nanotubes (see Figure 6.10f) as reported by Schmuki *et al*.[18] Due to the in-situ formed hydrofluoric acid, nanotubes are slowly dissolved from the top but are still increasing in length due to a continuing oxidation of the metal. The mass transport through the tubes seems to become the dominating factor, slowing down the dissolution reaction at the bottom permanently as the current slowly starts to decrease.

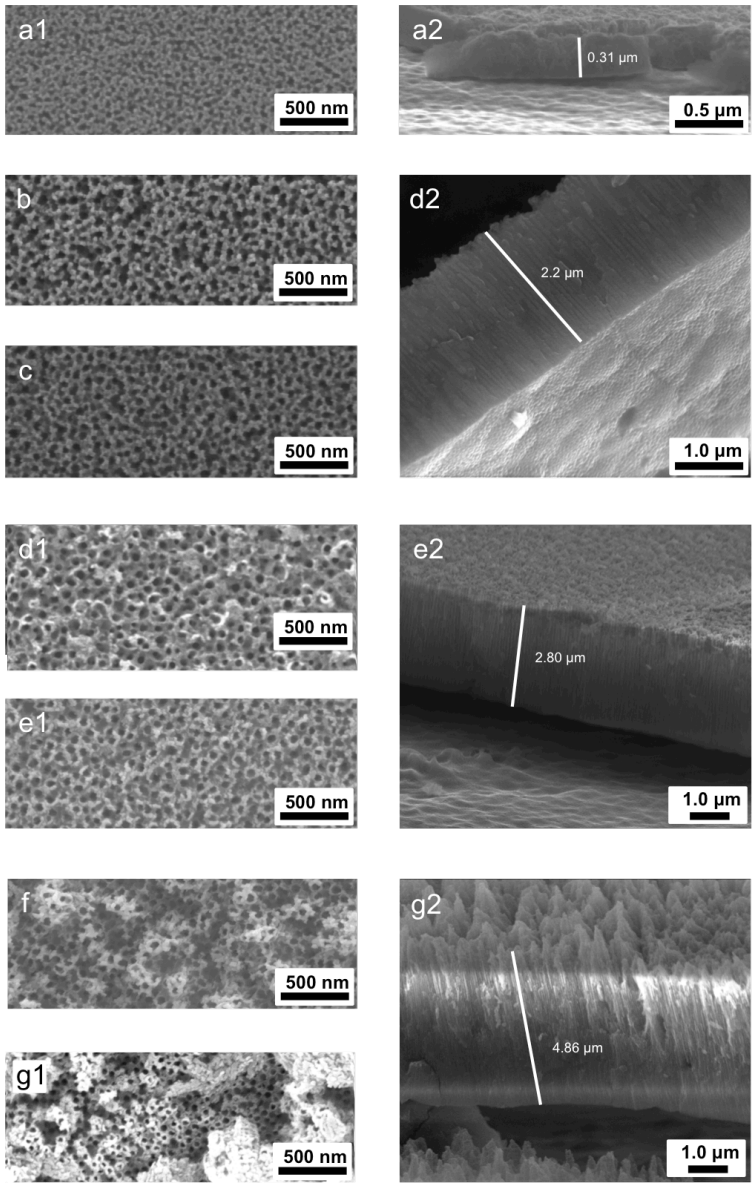

Figure 6.10 SEM images of iron foil after (a) 2.1, (b) 5.8, (c) 7.5, (d) 18.3, (e) 30, (f) 35 and (g) 60 min of anodization.

After 60 minutes, while increased in length (Figure 6.10g2), the nanotubular structure is unevenly etched, chunks of oxide material lay on the surface and the nanotubes look like they were melted together (Figure 6.10g1). This is the result of the increased dissolution of interpore iron(III) fluoride, which produces hydrofluoric

acid. The acid dissolves the pores from the outside, which results in the observed collapse of the pores. Also delamination of the film occurs due to the increased temperature at the bottom of the sample. During the reaction, the iron foil is in thermal contact with a massive copper block, with a high heat capacity and which is at room temperature at the beginning of the reaction. Since it takes longer time to heat the block, the foil also only slowly reaches the temperature of the electrolyte. It seems that at a certain temperature, migration of fluoride ions through the oxide is increased so much, that the formation of an oxyfluoride phase occurs on the metal surface resulting in delamination of the layer as reported by Habazaki *et al*.[19] In order to test this theory a reaction was carried out in which the copper block was heated to 70 °C by a hot plate. After only three minutes, delamination of the oxide film was observed (see Figure 6.11).

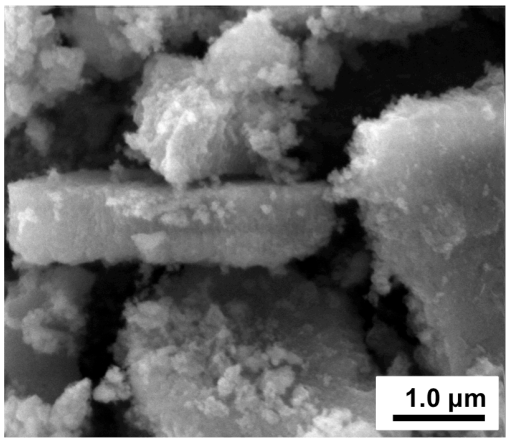

Figure 6.11 SEM image of anodized surface with a heated copper block.

6.3.4 Cross Section Measurement

If the foil anodized is bent, the film starts to break into pieces due to the induced stress. This can be used for further investigation of the structure. As mentioned above, diameter of the pores openings is about 50 nm. They exhibit a concave shape as the diameter decreases to 35 - 40 nm over the range of several nanometers. From there, a constant narrowing towards the end can be observed. While in the middle being 20 - 25 nm, diameter decreases close to the bottom to 10 - 15 nm (Figure 6.12 left). The bottom of the pores is closed with a barrier layer of about 2.5 nm in thickness. The metal surface shows imprints of the pore bottoms (Figure 6.12 right). Those imprints were also reported for AAO[20] and are used as a mask for higher ordering of the pores after a second anodization. Interpore distance is constant with 70 - 80 nm as measured on top of the pores, in the middle, at the bottom and on the imprints in the metal.

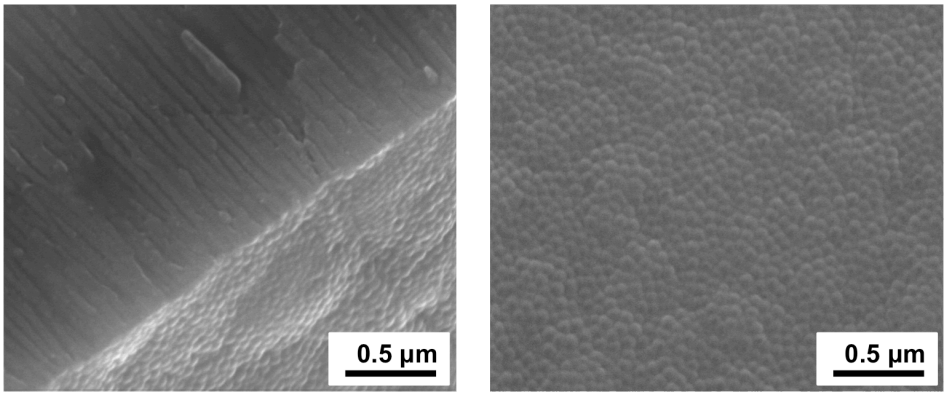

Figure 6.12 SEM images of anodized film Left: Bottom view of closed pores Right: Imprints on metal surface

6.3.5 Modulation of Anodic Bias

Voltage modulation is a common technique to tune the pore diameter. To test the application on the anodization of iron, different voltages were applied. SEM images of top view and cross section of the films are shown in Figure 6.13.

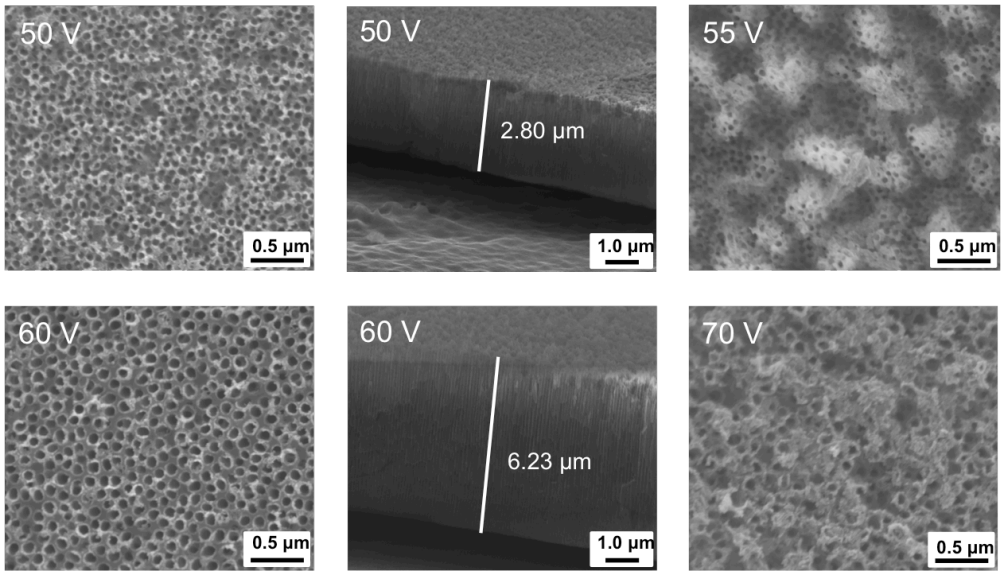

Figure 6.13 SEM images of anodized film after anodization for 30 min at 50 to 70 V.

At 50 V, the already mentioned nanoporous film with a diameter of 50 nm and a thickness of about 3 µm is produced. If the voltage is slightly increased to 55 V, the quality of the film suffers dramatically. The surface becomes uneven and nanotubes, while maintaining their diameter, are partly dissolved. This is probably due to the reaction speeding up to a point, where dissolution of the pores already begins. Surprisingly, a further increase of the voltage to 60 V increases the quality of the film again. This time though, pore diameter increases to 72 nm with a slight increase in standard deviation to 11 nm (see Figure 7.19b Appendix). More importantly, film

thickness increases up to 6.2 µm. It seems like the pore diameter increases in steps. At low applied voltages, no porous structure was formed. Between 50 - 55 V, diameter is 50 nm and increases to 72 nm at 60 V. A further increase in anodic bias decreases the film quality again and leads to a rough, unevenly etched surface with remaining oxide material lying on top of the pores, while the diameter of the pores remains constant.

6.3.6 Modulation of Water Concentration

The role of water was investigated by adding amounts between 1 - 3 wt% to the electrolyte. SEM images of the film and a comparison of the current curves are shown in Figure 6.14. Varying the concentration of water added to the electrolyte changes film quality as the reaction speed is modulated. On the one hand, the concentration of water dictates the limit for the oxygen available for the formation of iron(III) oxide. On the other hand, concentration of active fluoride ions increases by an increase of water, resulting in faster dissolution of the oxide.

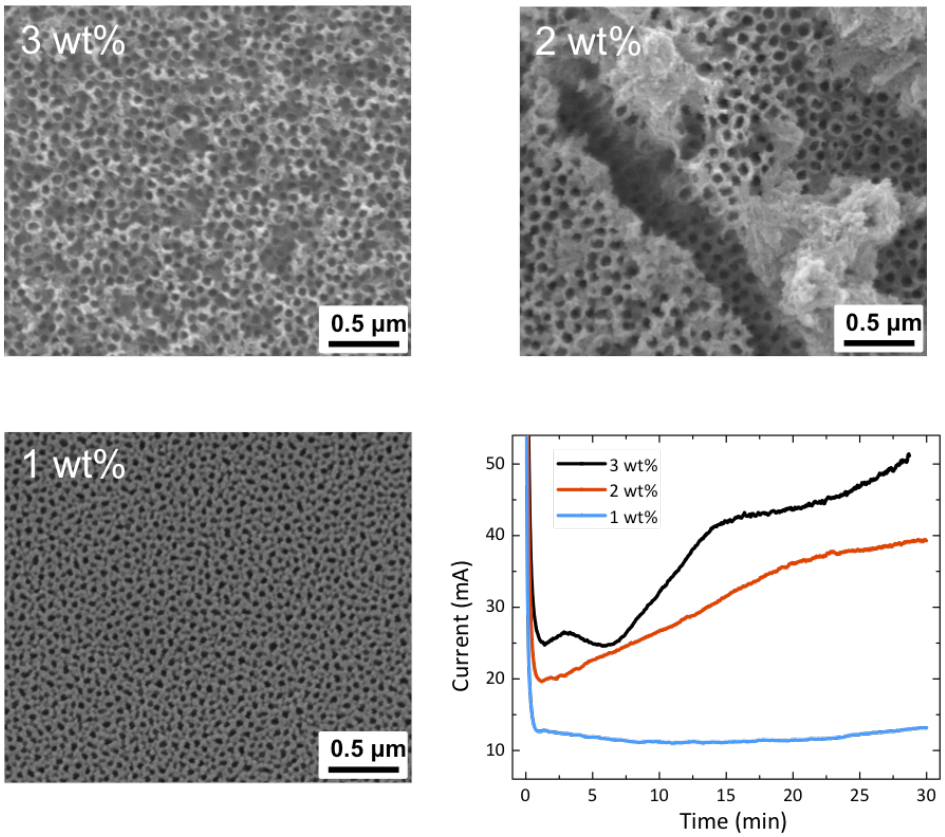

Figure 6.14 SEM images of anodized film with electrolyte containing 1 - 3 wt% water. Bottom right: Comparison of current curves.

At 3 wt%, a homogeneous porous structure is formed. A decrease to 2 wt% leads to large remains of oxide material from the surface layer which were not dissolved completely, even though a porous layer is synthesized. This is also reflected in the current curve, as the slope is reduced which can be translated into a decrease in reaction speed. A further decrease to 1 wt% leads to a porous layer similar to the one found after 3 min of anodization. Surface layer is not dissolved at all and the current stays low.

6.3.7 Stirring

On the basis of various reports about improvement in homogeneity of the porous structure by stirring of the electrolyte, anodization under stirring was investigated. Figure 6.15 shows SEM images of the anodized surface after 3 minutes while the solution was stirred with the stirring electrode at maximum velocity. At the center of the sample, the surface layer is mostly intact as visible by the small pore openings (Figure 6.15a). The effect of stirring is the least in the middle, so removal of the material is the slowest. In the middle between center and rim, pores openings are larger due to the increase in agitation of the electrolyte and thus the increased mass transport (Figure 6.15b). Close to the rim, pore openings are the largest, as most of the surface layer is already dissolved (Figure 6.15c).

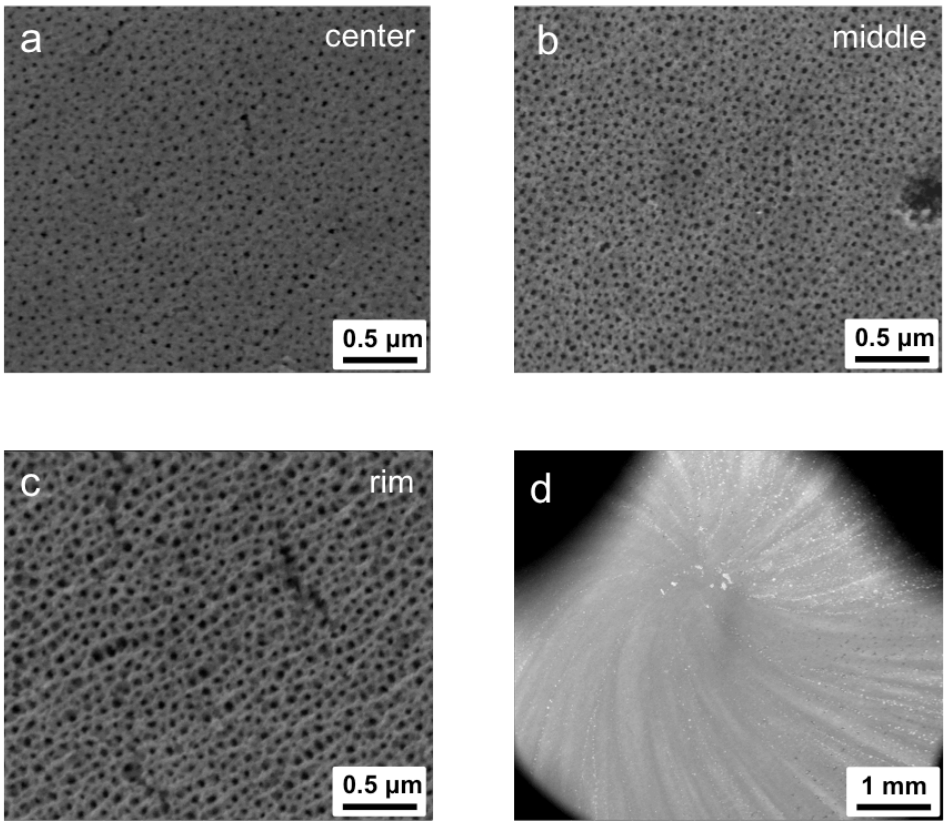

Figure 6.15 SEM images of iron foil after anodization for 3 min at 50 V with stirring electrode at maximum velocity at different locations. At the center, pores are only slightly opened (a). In the middle between center and rim, pores are opened further (b). Close to the sample rim, surface layer is already dissolved; pore openings are the largest (c). Low magnification shows uneven removal of oxidic material (d).

In addition to the variation of the film quality due to the difference in effective agitation of the electrolyte, low magnification SEM images of the sample show a macroscopically visible uneven material removal (Figure 6.15d). Due to the turbulences induced by the stirring electrode, oxidic material is distributed helically on the surface.

6.3.8 Tempering

Tempering is a technique commonly used to increase crystallinity of anodized metal oxide films. To investigate the effect of heat treatment on the film morphology, an anodized sample was heated with a heating rate of 5 °C/min and a dwell time of 30 min at 400 °C. Figure 6.16 shows SEM images of the anodized film after tempering. The surface is uneven, as the tubes seem to be melted together. Analysis of the cross section reveals the melting effect to be linear over the whole length of the tubes as they exhibit no cracking or bending and maintain the linear shape.

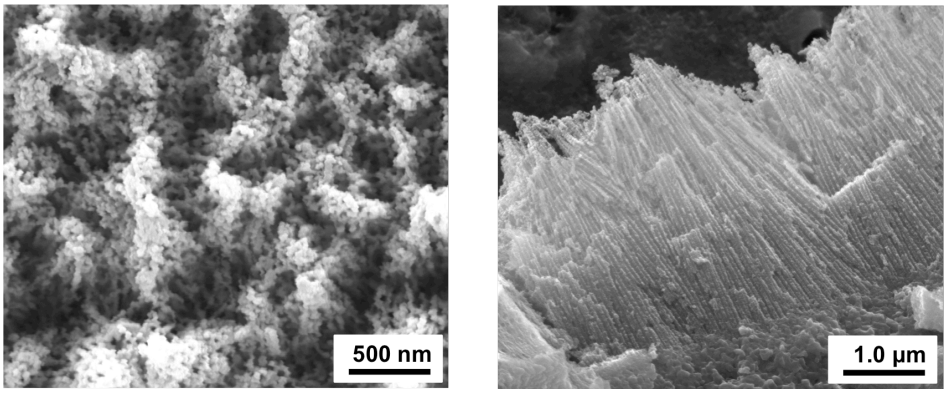

Figure 6.16 SEM images of iron foil after heat treatment. Left: Top view of anodized film showing an uneven and rough surface with melted-looking nanotubes. Right: Cross section view of anodized film showing the converging tubes.

The reason for the collapse of the structure seems to be the removal of crystallization water from the metal oxide resulting in a collapse of the structure (see Chapter 6.3.3).

6.4 Conclusion

An easy and fast electropolishing procedure for commercially available iron foils has been established. By the use of an electrolyte based on alcohols, perchloric acid and water, a single step polishing procedure with the use of a custom-made rotating electrode has lead to very smooth and clean polished iron foils. By the introduction of a preheating step for the electrolyte, the anodization of iron for the synthesis of iron oxide nanotubes could be successfully adapted to the custom made setup. The growth mechanism was studied in detail, revealing an alternating reaction of pore formation and surface etching by potential differences induced by possible oversaturation of IHF at the pore bottom. Cross section measurements of the film revealed a conical shape of the pores with a constant interpore distance and closed pore bottoms. Indentations in the metal, previously only reported for aluminum, could be observed and pave the way for a possible second anodization to further increase homogeneity of the nanopores. Modulations of the anodic bias lead to a step-wise increase in pore diameter and yielded an even greater film thickness. Variation in the abundance of water in the electrolyte resulted in a decrease in film quality as the reaction is slowed down, leading to a non-optimal dissolution of the surface layer. Tempering decreases film quality as the structure gradually collapses due to removal of crystallization water from the oxide.

6.5 References

[1] S. U. M. Khan and J. Akikusa, "Photoelectrochemical splitting of water at nanocrystalline n-Fe2O3 thin-film electrodes," *J. Phys. Chem. B*, vol. 103, no. 34, pp. 7184–7189, 1999.

[2] A. Duret and M. Grätzel, "Visible light-induced water oxidation on mesoscopic alpha-Fe2O3 films made by ultrasonic spray pyrolysis.," *J. Phys. Chem. B*, vol. 109, no. 36, pp. 17184–17191, 2005.

[3] I. Cesar, A. Kay, J. A. G. Martinez, and M. Grätzel, "Translucent thin film Fe2O3 photoanodes for efficient water splitting by sunlight: Nanostructure-directing effect of Si-doping," *J. Am. Chem. Soc.*, vol. 128, no. 14, pp. 4582–4583, 2006.

[4] A. Kleiman-Shwarsctein, Y. S. Hu, A. J. Forman, G. D. Stucky, and E. W. McFarland, "Electrodeposition of α-Fe2O3 doped with Mo or Cr as photoanodes for photocatalytic water splitting," *J. Phys. Chem. C*, vol. 112, no. 40, pp. 15900–15907, 2008.

[5] Y. S. Hu, A. Kleiman-Shwarsctein, A. J. Forman, D. Hazen, J. N. Park and E. W. McFarland, "Pt-doped α-Fe2O3 thin films active for photoelectrochemical water splitting," *Chem. Mater.*, vol. 20, no. 12, pp. 3803–3805, 2008.

[6] X. Gou, G. Wang, X. Kong, D. Wexler, J. Horvat, J. Yang and J. Park, "Flutelike porous hematite nanorods and branched nanostructures: Synthesis, characterisation and application for gas-sensing," *Chem. - A Eur. J.*, vol. 14, no. 19, pp. 5996–6002, 2008.

[7] L. Liao, Z. Zheng, B. Yan, J. X. Zhang, H. Gong, J. C. Li, C. Liu, Z. X. Shen and T. Yu, "Morphology controllable synthesis of α-Fe2O3 1D nanostructures: Growth mechanism and nanodevice based on single nanowire," *J. Phys. Chem. C*, vol. 112, no. 29, pp. 10784–10788, 2008.

[8] W. M. Zhang, X. L. Wu, J. S. Hu, Y. G. Guo and L. J. Wan, "Carbon coated Fe3O4 nanospindles as a superior anode material for lithium-ion batteries," *Adv. Funct. Mater.*, vol. 18, no. 24, pp. 3941–3946, 2008.

[9] M. V. Reddy, T. Yu, C. H. Sow, Z. X. Shen, C. T. Lim, G. V. Subba Rao and B. V. R. Chowdari, "α-Fe2O3 Nanoflakes as an Anode Material for Li-Ion Batteries," *Adv. Funct. Mater.*, vol. 17, no. 15, pp. 2792–2799, 2007.

[10] T. J. Latempa, X. Feng, M. Paulose, C. a Grimes, V. Uni, U. V Park and V. Pennsyl, "Temperature-Dependent Growth of Self-Assembled Hematite (r-Fe2O3) Nanotube Arrays : Rapid Electrochemical Synthesis and Photoelectrochemical Properties," vol. 113, pp. 16293–16298, 2009.

[11] R. R. Rangaraju, a Panday, K. S. Raja and M. Misra, "Nanostructured anodic iron oxide film as photoanode for water oxidation," *J. Phys. D. Appl. Phys.*, vol. 42, p. 135303, 2009.

[12] S.-H. Yu, J. Shin, J.-J. Kim, K. J. Lee and Y.-E. Sung, "Vertically aligned iron oxide nanotube arrays and porous magnetite nanostructures as three-dimensional electrodes for lithium ion microbatteries," *RSC Adv.*, vol. 2, pp. 12177–12181, 2012.

[13] H. E. Prakasam, O. K. Varghese, M. Paulose, G. K. Mor. and C. A. Grimes, "Synthesis and photoelectrochemical properties of nanoporous iron (III) oxide by potentiostatic anodization," *Nanotechnology*, vol. 17, pp. 4285–4291, 2006.

[14] S. Yeonmi and L. Seonghoon, "Self-organized regular arrays of anodic TiO2 nanotubes," *Nano Lett.*, vol. 8, no. 10, pp. 3171–3173, 2008.

[15] B. J. Park, H. E. Prakasam, and C. A. Grimes, "Fabrication of Iron (III) Oxide Nanostructures By Potentiostatic Anodization," *EEREU Annu. Res. J. Electr. Eng. Res. Exp. Undergraduates*, vol. III, p. 117, 2005.

[16] R. R. Rangaraju, K. S. Raja, A. Panday and M. Misra, "An investigation on room temperature synthesis of vertically oriented arrays of iron oxide nanotubes by anodization of iron," *Electrochim. Acta*, vol. 55, pp. 785–793, 2010.

[17] M. Wang, Y. Liu and H. Yang, "A unified thermodynamic theory for the formation of anodized metal oxide structures," *Electrochim. Acta*, vol. 62, pp. 424–432, 2012.

[18] S. P. Albu, A. Ghicov and P. Schmuki, "High aspect ratio, self-ordered iron oxide nanopores formed by anodization of Fe in ethylene glycol/NH4F electrolytes," *Phys. Status Solidi - Rapid Res. Lett.*, vol. 3, no. 2, pp. 64–66, 2009.

[19] H. Habazaki, K. Fushimi, K. Shimizu, P. Skeldon and G. E. Thompson, "Fast migration of fluoride ions in growing anodic titanium oxide," *Electrochem. commun.*, vol. 9, no. 5, pp. 1222–1227, 2007.

[20] H. Masuda and K. Fukuda, "Ordered metal nanohole arrays made by a two-step replication of honeycomb structures of anodic alumina.," *Science*, vol. 268, no. 5216, pp. 1466–1468, 1995.

7 Summary and Outlook

The aim of this work was to gain insight into the mechanism of the electrochemical anodization of both tin and iron. This knowledge should then be used to increase film quality.

In **chapter 2** it was demonstrated that by the combination of tempering and the use of a buffered solution, homogeneity of sponge-like tin oxide film could be increased. By tempering of the foil at 400 °C and a slow cooling rate, tin recrystallizes with a high degree of orientation alignment. This inhibits cavities, typically formed after anodization in the nanoporous structure due to former grain boundaries. With the use of a buffered solution, the precipitation of tin oxalate could be inhibited and a smooth porous film with a slight increase in pore wall thickness and homogeneity could be synthesized. The film mainly consists of tin(II) oxide as proven by X-ray diffraction. Film thickness was measured to be 26 µm and is homogeneous over 97 % of the sample surface. Backsides of the pores are closed and the underlying bulk metal shows no imprints. High-resolution cross section SEM revealed that the sponge to consist of a regular alignment of ordered pores arranged in a lamellar manner with a length of ~250 nm.

By the use of the buffered solution, it was possible to anodize tin at voltages below 5 V, leading to the discovery of a new lamellar arrangement. **Chapter 3** explored the growth mechanism of this Sn/SnO_2 structure. It is homogeneous over the whole anodized surface as demonstrated by low resolution SEM and the optical behavior upon rotating and tilting of the foil. Mössbauer spectroscopy showed the lamellae to

consist of a SnO_2 shell with an Sn core. Due to the penetration depth of gamma radiation of about 100 nm, the shell was estimated to be about 90 nm in thickness. XPS measurements confirmed the core-shell structure of the lamellae by showing a shift of the Sn signals to lower binding energies after sputtering. Additionally the oxygen signal decreased due to the removal of the oxide shell. The lamellae are etched along the *a,b* plane of the crystal structure as proven by X-ray measurement of a sample prior to anodization. The orientation of the tetragonal axis of the crystal structure was found to be inclined by 20° with respect to the surface normal. This translates into an inclination of the *a,b* plane of 70°, which was found to be the orientation of the lamellae after anodization. It was assumed that the anisotropic conductivity is the reason for a faster dissolution of tin in the *a,b* plane. The growth mechanism can be divided into three steps as proven by cross section SEM. First, the surface is passivated. Then, a blade-like structure is formed, which is subsequently transformed into the final lamellar structure by splitting of thick blades and widening of trench-bottoms. Orientation of the lamellae could be predicted by comparison of the current curves of the anodization. Vertically oriented lamellae show the highest increase in surface area, so the current is the highest. Due to a slow collapse of the structure, the current slowly decreases as the reaction continues. Horizontally aligned lamellae show the lowest increase in surface area and thus the lowest current, which slowly increases due to a further increase in surface area as the lamellae are formed. Variations from the optimal parameters of the reaction lead to a decrease in film quality. If the anodization potential is lowered or the concentration of oxalic acid is increased, the surface becomes rough and exhibits a high degree of defects. If the anodization potential is increased or the concentration of oxalic acid is

decreased, precipitation of tin oxalate occurs, passivating the sample surface and inhibiting the formation of lamellae.

A comparison of selected properties of the lamellar and sponge-like tin oxide was shown in **chapter 4**. While both structures showed photocatalytic behavior, the tin oxide sponge was able to decrease the Rhodamine B concentration only by 71 % while lamellar tin oxide yielded a degradation of 89 %. The reason for this seems to be the high surface area due to the lamellar arrangement combined with short diffusion pathways because of the thin oxide layer, resulting in highly efficient electron-hole separation. Additionally, the lamellar structure showed a structure dependent amphiphilic behavior. While vertical oriented lamellae do not offer enough contact area to sustain a stable solid-liquid-air interface, horizontally oriented lamellae exhibit a switchable contact angle for water. By irradiation with UV light or by keeping the sample in the dark, the contact angle could be switched between 35° and 133° respectively. The surface texture of sponge-like tin oxide does not exhibit this property, as the contact angle did not change under irradiation with UV light. Additionally, the structure was not able to support a water droplet and was soaked within minutes. The lamellar structure also exhibits an increased antibacterial activity as proven by co-incubation with *E. coli* bacteria. On the sponge-like tin oxide, a high degree of bacteria was destroyed as visible by the remaining fragments of bacteria in the inoculated area. On the lamellar tin oxide no bacteria growth was observed, proving an even higher degree of antibacterial activity.

In **chapter 5**, sponge-like tin oxide was investigated as electrode material in a lithium ion half-cell before and after coating with carbon. The anodized film was found to

consist mainly of tin oxide with a thin tin-gluing layer on the oxide-copper interface, as proven by XRD, cross section EDX, SEM and XPS analysis. The tin-gluing layer increases durability of the film, as even on bending of the sample, the porous film showed no chipping. If the anodization is conducted for a longer time, the gluing layer is oxidized as well, which results in spalling of the porous film. Carbon coating and the subsequent heat treatment lead to a gradual reduction of the oxide, as visible by XRD, EDX and XPS analysis. Electrochemical analysis of the film showed an increase in capacity and stability upon cycling after carbon coating. The obtained specific capacity for the coated sample was found to be up to the 50th cycle constantly 120 mAh g^{-1} higher compared to the uncoated sponge.

The anodization of iron was discussed in **chapter 6**. As a first step, an easy electropolishing procedure with the use of a custom-made rotating electrode could be established. Furthermore it was shown that the temperature of the electrolyte plays an important part in the anodization of iron. Below 60 °C, no porous structure could be achieved. A further increase in temperature increased homogeneity of the pores. At a temperature of 70 °C, a nanoporous film with an even thickness of 2.8 µm and a pore diameter of 50 nm could be synthesized. Growth of the porous structure was found to be decidedly different from the anodization of aluminum or tin. Investigation of the growth mechanism showed the reaction to be an alternation between pore formation and surface dissolution because of a possible oversaturation of iron fluoride anions at the pore bottoms, decreasing the effective potential. Cross section measurement revealed a truncated shape of the pores, reflecting the decrease in oxide dissolution efficiency towards the pore bottoms. Pores are closed with a barrier layer thickness of 2.5 nm. The metals surface shows imprints that could be used in the

future for a second anodization, further increasing homogeneity of the film. Pore diameter of the iron oxide film seems to increase in steps as an increase of 10 V lead to a homogeneous thick film with an increased pore size of 72 nm while an increase of 5 V decreased the film quality on the surface due to promoted dissolution of the film. A water concentration of 3 wt% was found to be necessary to allow the successful dissolution of the surface film. At lower concentrations, remnants of the oxide were found on the surface. Stirring, even though reported in different publications, was found to be counterproductive as it decreased homogeneity of the film and showed a macroscopically visible uneven material removal.

It can be concluded that the work presented in this thesis developed the insight into the growth mechanism for the anodization of both tin and iron. This knowledge could be used to successfully improve film quality. Furthermore, the discovery of the lamellar Sn/SnO_2 structure could pave the way for the application as a self-cleaning surface.

Future work in this particular field should include further investigation of the growth of the lamellar structure to be able to explain the spacing between etched cavities. Additionally it should be investigated how the orientation of the crystal structure can be manipulated to control orientation of the lamellae. First experiments were made by melting the sample in high magnetic fields but did not lead to a distinct result at the time of this thesis. Finally, application as an electrode material should be investigated for the lamellae, as the high surface area in combination with an abundance of the cycling-stable *a,b* surface should lead to a high performance and stability of the electrode. Concerning the anodization of iron oxide, the growth

mechanism should be investigated further by the use of XPS and cross section EDX to prove the proposed oversaturation of IHF at the pore bottoms.

Appendix

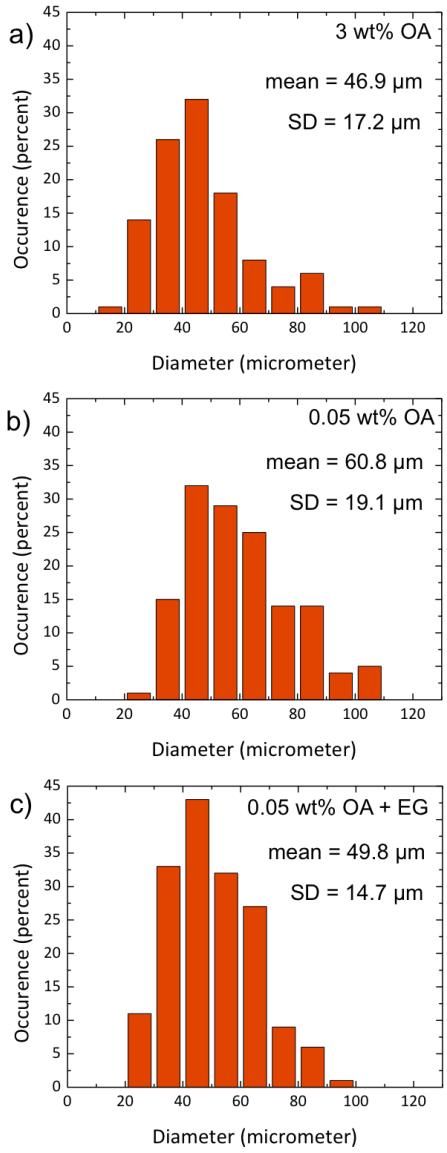

Figure 7.1 Histograms of pore diameters of the tin sponge after anodization for 10 min at 10 V in different electrolytes.

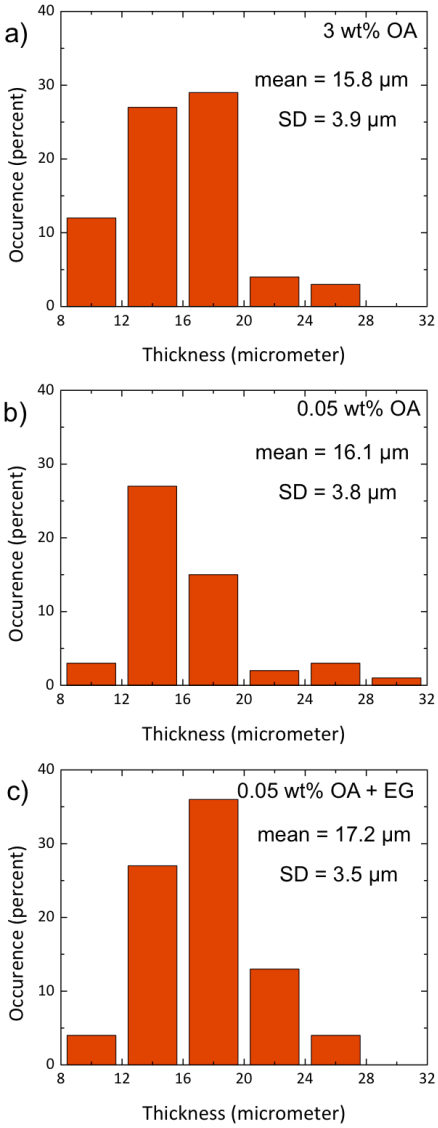

Figure 7.2 Histograms of wall thickness of the tin sponge after anodization for 10 min at 10 V in different electrolytes.

Table 7.1 Peak fitting result of XPS measurement. Corrected area and atomic concentration data for the 3d5 and 3d3 peak for tin(IV) and metallic tin from surface measurement of the unsputtered anodized tin surface.

Unsputtered Surface	Peak	Corrected Area RA/(RSF*T*MFP)	Atomic Concentration
Sn4+	3d5	5839.49	55.50%
	3d3	4041.53	38.41%
Sn	3d5	387.89	3.69%
	3d3	252.33	2.40%

RA: Uncorrected or raw intensity of background substracted peak in CPS*eV
RSF: Library Relative Sensitivity Factor
T: Value of the transmission correction function at the kinetic energy of the peak maximum
MFP: Value of the mean free path correction function at the kinetic energy of the peak maximum (escape depth approximation).

Table 7.2 Peak fitting result of XPS measurement. Corrected area and atomic concentration data of the 3d5 and 3d3 peak for tin(IV) and metallic tin from surface measurement on the sputtered anodized tin surface.

Sputtered Surface	Peak	Corrected Area RA/(RSF*T*MFP)	Atomic Concentration
Sn4+	3d5	644.30	6.19%
	3d3	397.05	3.81%
Sn	3d5	5516.24	53.96%
	3d3	3750.25	36.03%

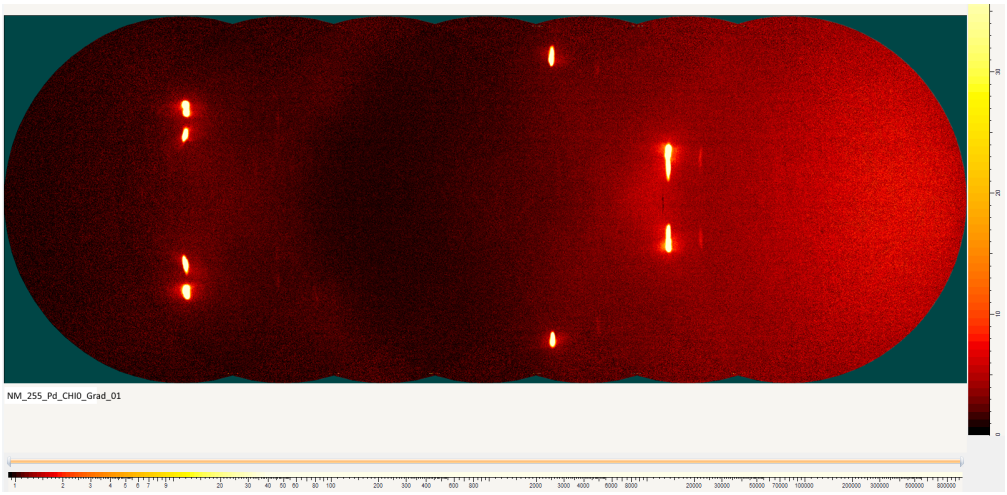

Figure 7.3 Two-dimensional X-ray diffraction pattern of a polished tin surface (χ scan, χ=0°) to determine the mosaicity of the structure and the nanodomain composition.

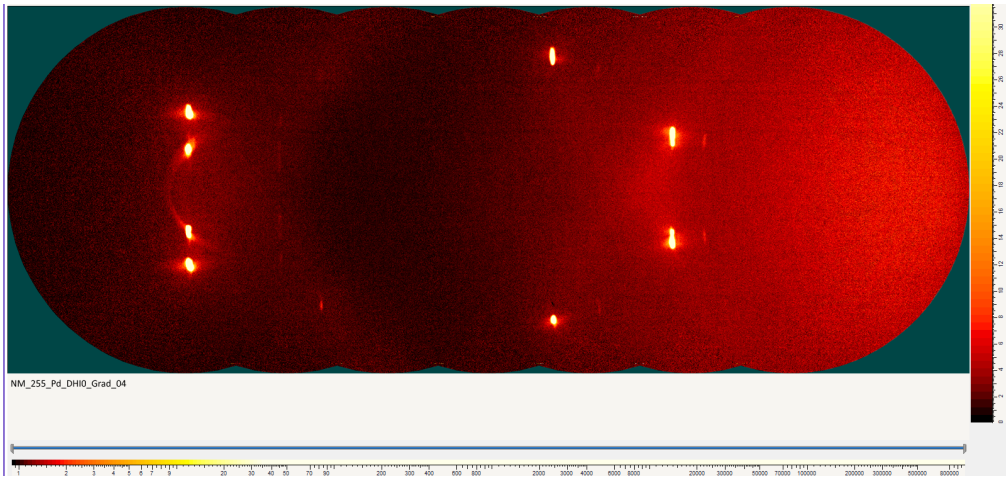

Figure 7.4 Two-dimensional X-ray diffraction pattern of a polished tin surface (χ scan, χ=20°) to determine the mosaicity of the structure and the nanodomain composition.

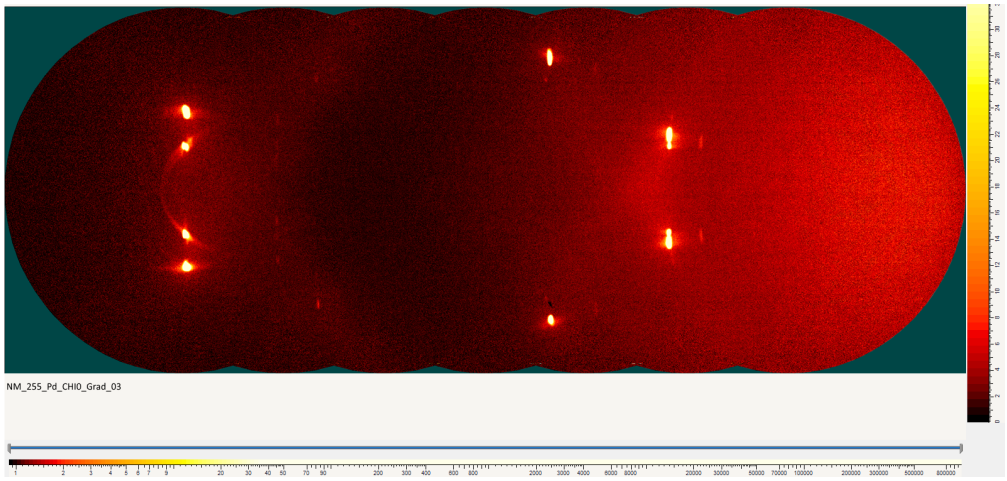

Figure 7.5 Two-dimensional X-ray diffraction pattern of a polished tin surface (χ scan, χ=40°) to determine the mosaicity of the structure and the nanodomain composition.

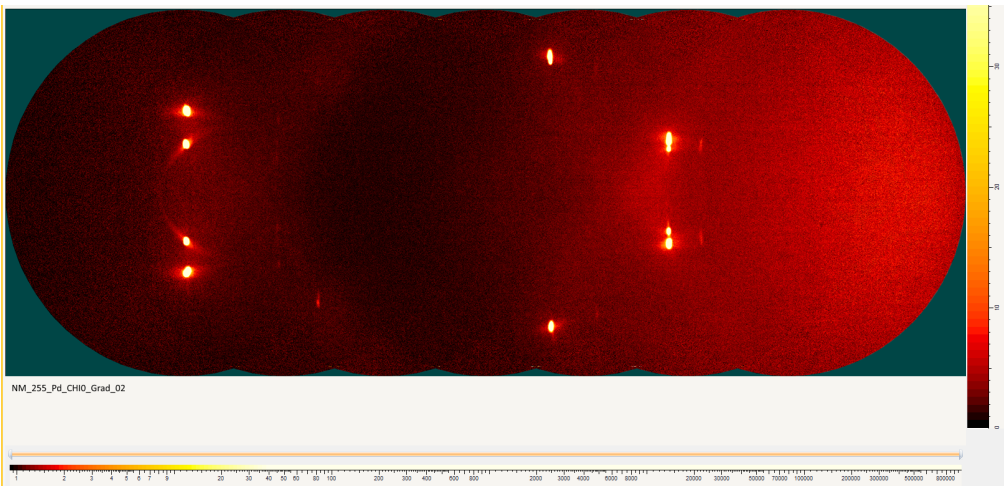

Figure 7.6 Two-dimensional X-ray diffraction pattern of a polished tin surface (χ scan, χ=60°) to determine the mosaicity of the structure and the nanodomain composition.

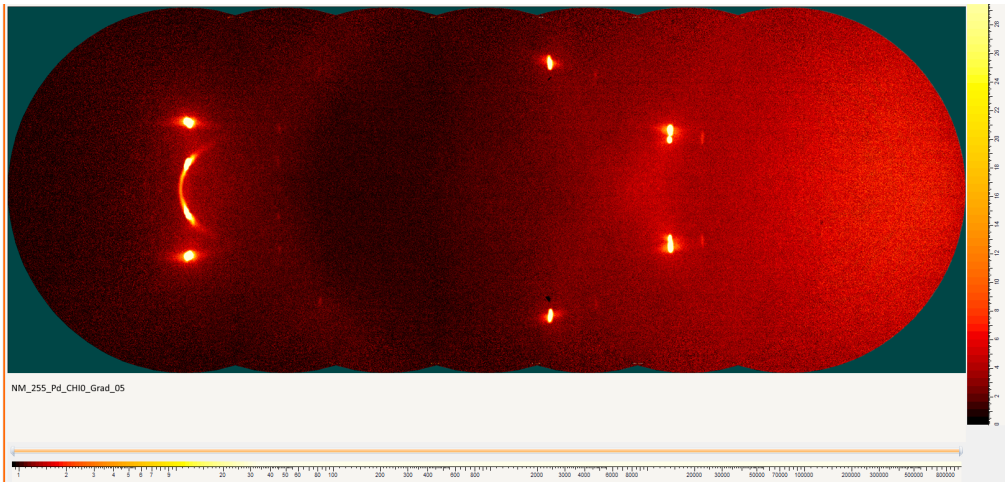

Figure 7.7 Two-dimensional X-ray diffraction pattern of a polished tin surface (χ scan, χ=80°) to determine the mosaicity of the structure and the nanodomain composition.

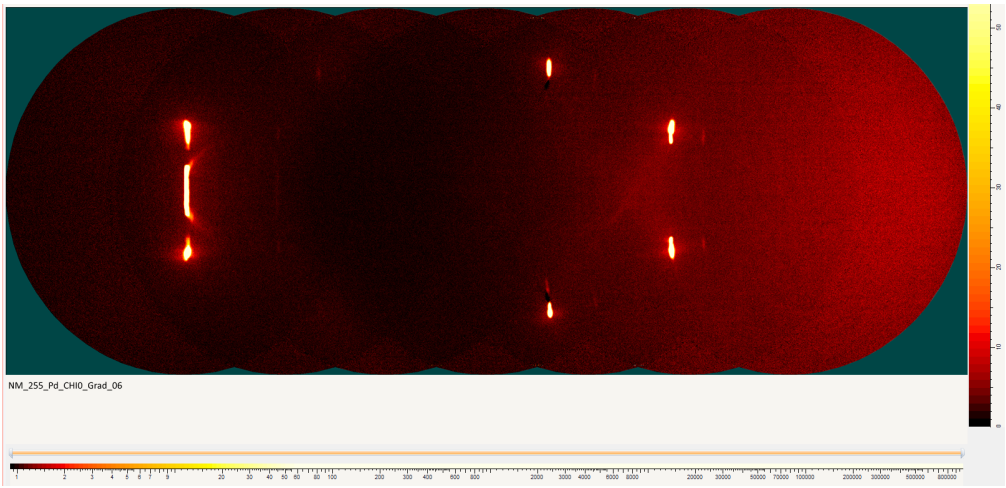

Figure 7.8 Two-dimensional X-ray diffraction pattern of a polished tin surface (χ scan, χ=100°) to determine the mosaicity of the structure and the nanodomain composition.

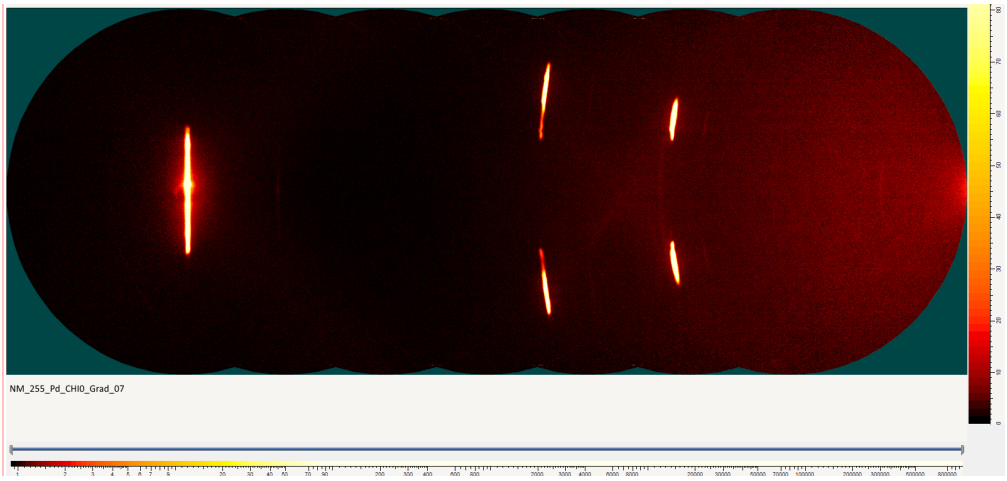

Figure 7.9 Two-dimensional X-ray diffraction pattern of a polished tin surface (χ scan, χ=120°) to determine the mosaicity of the structure and the nanodomain composition.

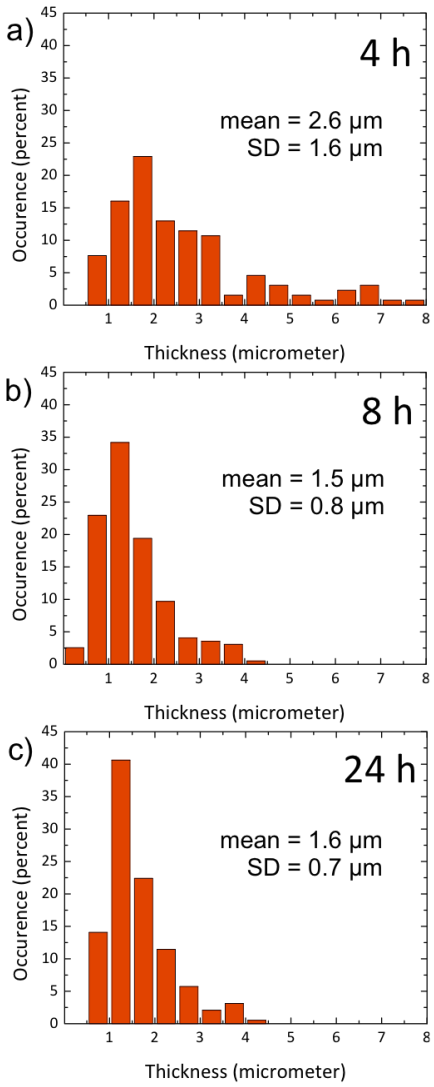

Figure 7.10 Histogram of measured lamellae thickness after 4, 8 and 24 h anodization time. Lamellae of less than 10 µm length were omitted, thickness was measured at the lowest point. a) After 4 hours, the mean thickness is 2.6 µm with a standard deviation (SD) of 1.6 µm. Amount of thickness between 0.75 to 2.25 µm is less than 60 %. b) Splitting of lamellae due to new trenches after 8 hours leads to a decrease in mean thickness and standard deviation to 1.5 and 0.8 µm respectively. Amount of thickness between 0.75 and 2.25 µm increases to 86 %. c) As the transformation to lamellae continues, bottom parts of trenches are widened and lamellar surface smoothened. After 24 hours, the thickness stays constant at 1.6 µm while size distribution is slightly narrowed to a SD of 0.7 µm. Amount of thickness between 0.75 and 2.25 µm is increased to 89 %.

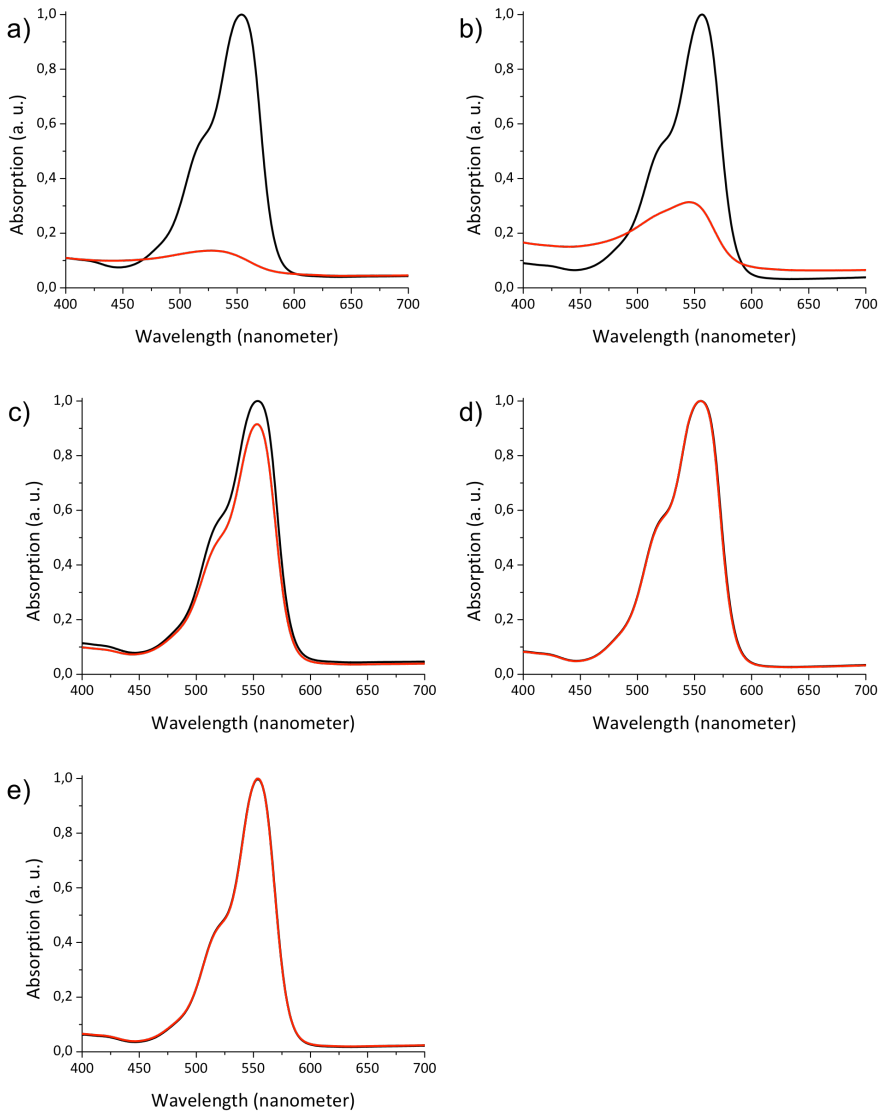

Figure 7.11 UV-Vis spectra of Rhodamine B before (black) and after (red) irradiation with UV light for 210 minutes. a,c) Spectra of the degradation of Rhodamine B under UV irradiation with a) the lamellar sample, b) the sponge-like sample, c) the polished sample and d) no sample. e) UV-Vis Spectra of Rhodamine B before and after being in contact with a lamellar sample for 210 minutes in the dark.

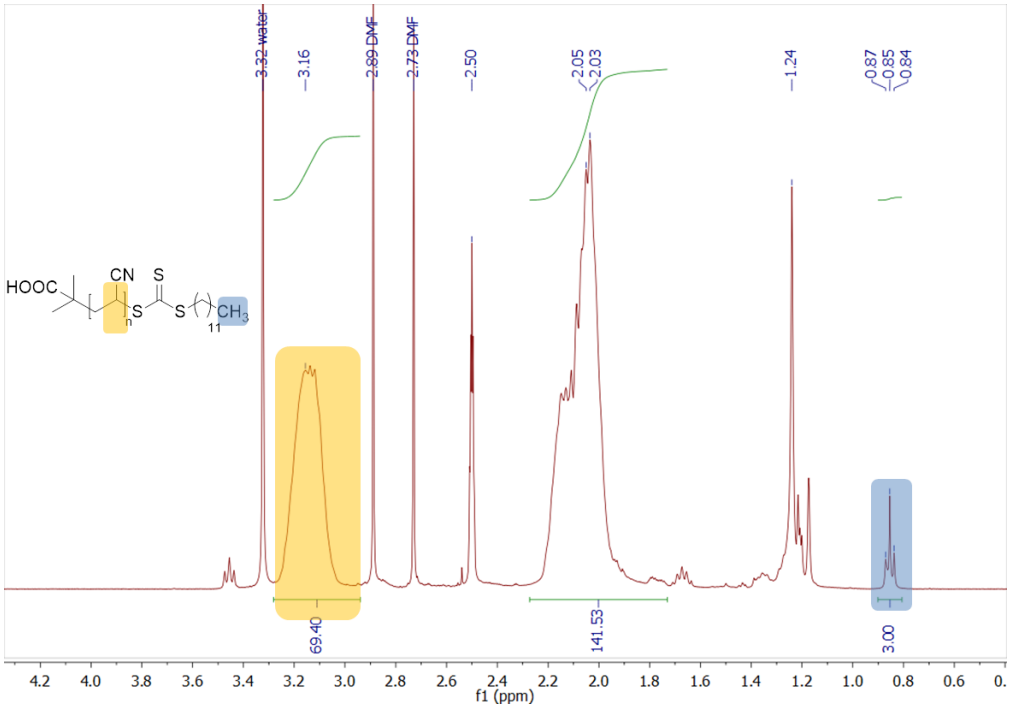

Figure 7.12 ^{1}H-NMR spectrum of polyacrylonitrile. The number average of the molecular weight is determined to be 70, as confirmed by the ratio of the integrals of the signals at 0.85 ppm (CH_3-group of the chain transfer agent end-group) and the signal at 3.16 ppm (CH-backbone signal of the polyacrylonitrile). Measurement and data treatment performed by [redacted]

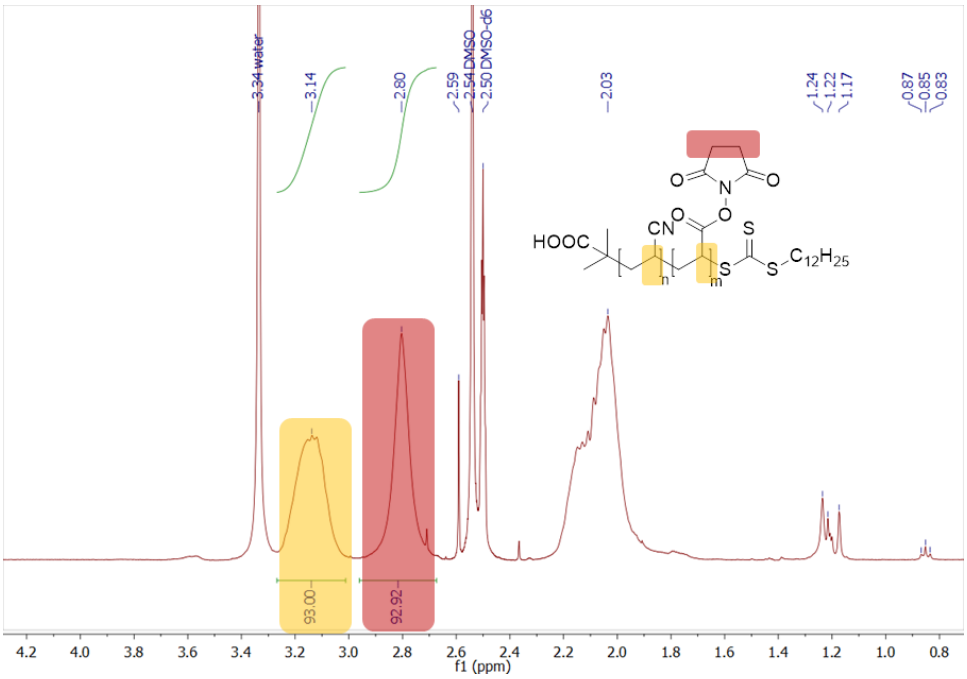

Figure 7.13 ^{1}H-NMR spectrum of poly(acrylonitrile-block-N-acryloxysuccinimide). Measurement and data treatment performed by [redacted]

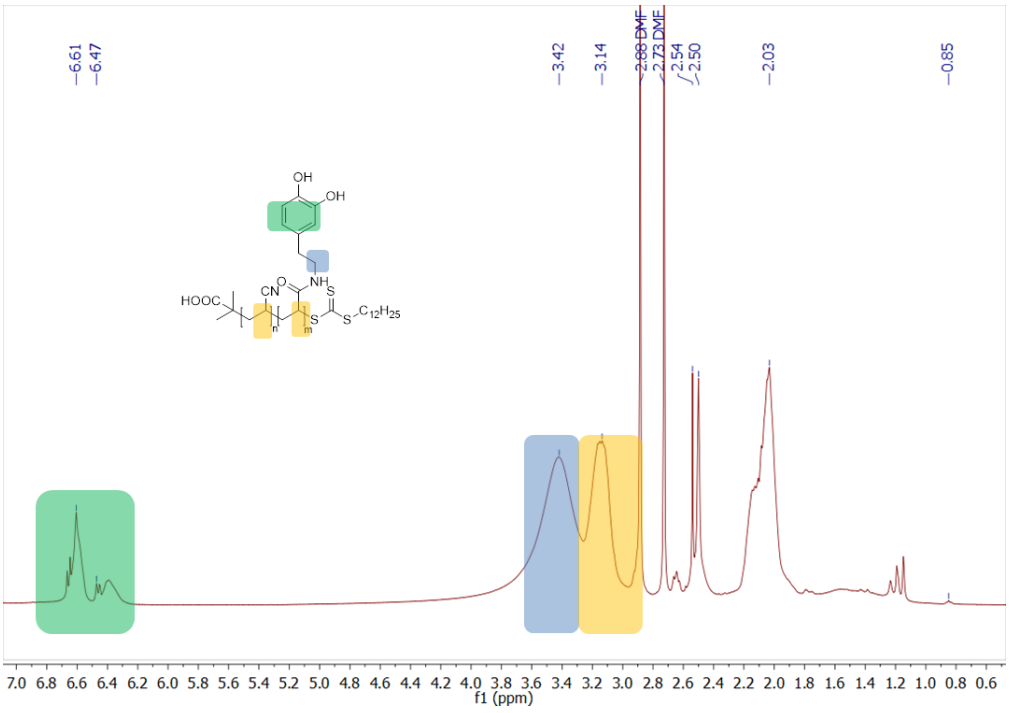

Figure 7.14 ^{1}H-NMR spectrum of poly(acrylonitrile-block-dopamine acrylamide) showing both the typical polyacrylonitrile signals and the dopamine acrylamide signals. Measurement and data treatment performed by [redacted]

Table 7.3 Atomic Concentrations for measured elements of carbon coated sample

	C	O	Cu	Sn
1	5.07	0	92.7187	2.2129
2	0	8.5573	55.002	36.4406
3	0	38.9735	4.415	56.6115
4	0	38.0204	2.751	59.2285
5	0	41.0113	1.6139	57.3748
6	0	40.2376	2.9094	54.2173

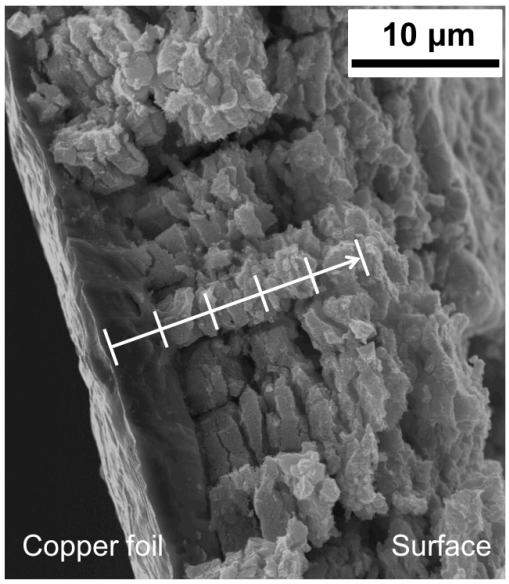

Figure 7.15 Cross section SEM image of carbon coated SnO_x sponge. Numbers inidcate measuring points for EDX, the arrow shows the direction of measurement.

Table 7.4 Atomic Concentrations for measured elements of carbon coated sample

	C	O	Cu	Sn
1	0.00	0.73	95.31	3.95
2	3.42	27.73	8.86	59.99
3	3.05	29.56	3.44	63.95
4	2.09	31.45	2.87	63.59
5	0.98	14.90	2.81	81.31
6	1.52	8.68	1.52	87.49

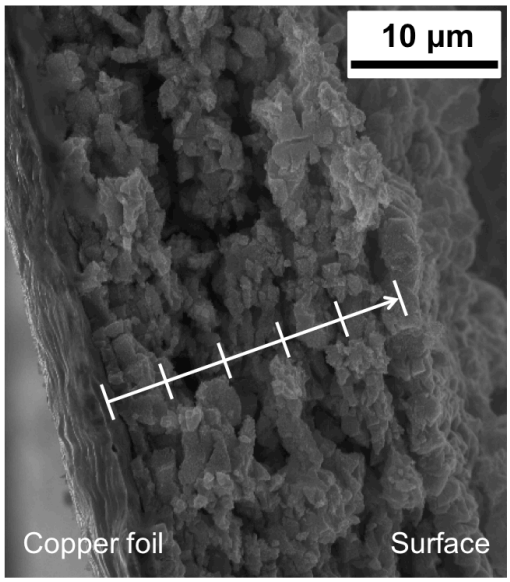

Figure 7.16 Cross section SEM image of carbon coated SnO_x sponge. Numbers inidcate measuring points for EDX, the arrow shows the direction of measurement.

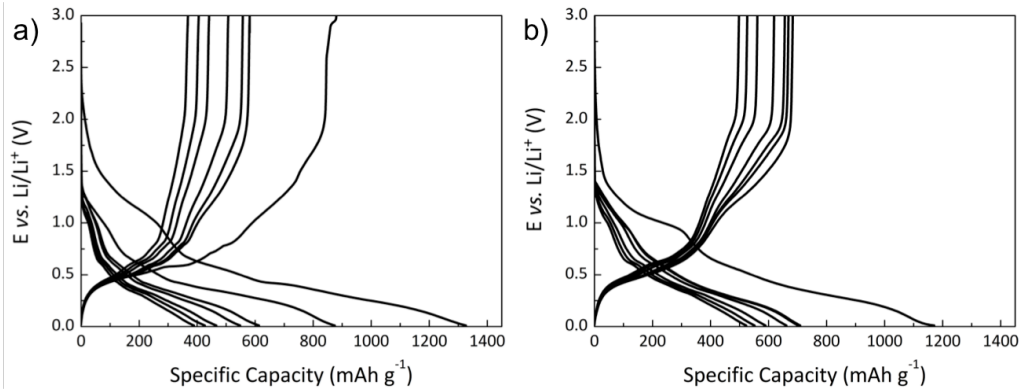

Figure 7.17 Potential profiles of cycles 1, 2, 3, 5, 10, 15, 20 for uncoated SnO_x (a) and coated SnO_x (b) at 0.05 C. Cut-off potentials: 0.01 and 3.0 V *vs.* Li/Li^+. Measurement and data treatment performed by [redacted]

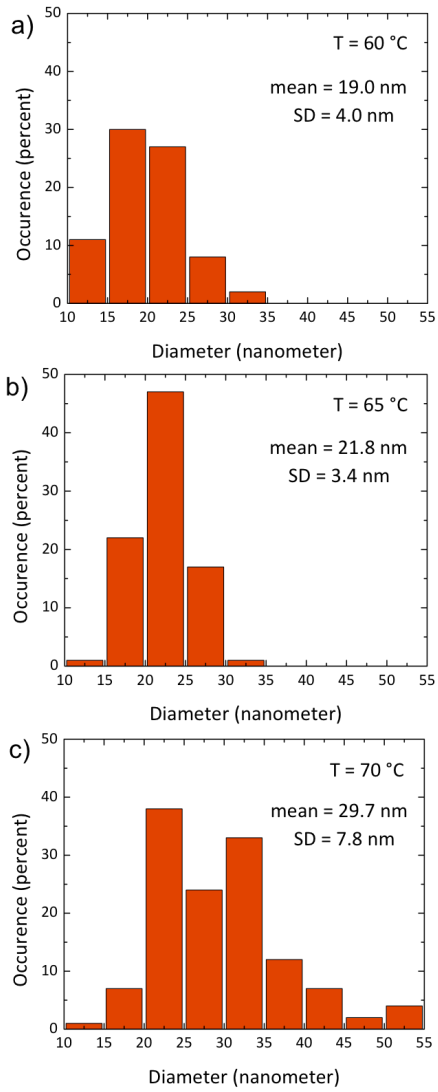

Figure 7.18 Histogram of measured pore diameter of anodized iron foil after 3 min at different electrolyte temperatures.

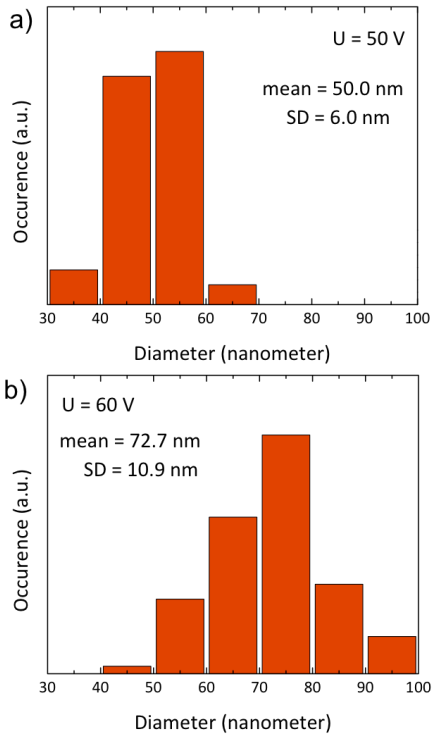

Figure 7.19 Histogram of measured pore diameter of anodized iron foil after 30 min at 50 V (a) and 60 V (b)

List of Figures

List of Tables

List of publications

[1] M. Khan, A. H. Al-Marri, M. Khan, **N. Mohri**, S. F. Adil, A. Al-Warthan, M. R. H. Siddiqui, H. Z. Alkhathlan, R. Berger, W. Tremel, and M. N. Tahir, "Pulicaria glutinosa plant extract: a green and eco-friendly reducing agent for the preparation of highly reduced graphene oxide," *RSC Adv.*, vol. 4, no. 46, p. 24119, 2014.

[2] S. F. Adil, S. Alabbad, M. Kuniyil, M. Khan, A. Alwarthan, **N. Mohri**, W. Tremel, M. N. Tahir, and M. R. H. Siddiqui, "Vanadia supported on nickel manganese oxide nanocatalysts for the catalytic oxidation of aromatic alcohols," *Nanoscale Res. Lett.*, vol. 10, no. 1, 2015.

[3] **N. Mohri**, M. Panthoefer, V. Ksenofontov, H. Götz, H. Duschner, W. Tremel "Self-Organized Arrays of SnO_2 Lamellae: Synthesis and Growth Mechanis" *to be submitted*

[4] **N. Mohri**, T. Link, R. André, H. Götz, H.Duschner, W. Tremel "Application of Self-Organized Arrays of SnO_2 Microplates with Enhanced Photocatalytic and Antimicrobial Properties compare to sponge-like SnO_2" *to be submitted*

[5] **N. Mohri**,* B. Oschmann,* F. Mueller, M. N. Tahir, S. Passerini, R. Zentel, W. Tremel "Synthesis and Characterization of Carbon Coated Sponge-like Tin Oxide Films and Their Application as Electrode Materials in Lithium Ion Batteries" *to be submitted*